FEASIBILITY TEST OF EXOTIC PARTICLE SEARCHES IN THE DECAY OF TRAPPED RUBIDIUM ISOMERS

by

Tao Kong

Master of Science, University of British Columbia, 2006
Master of Science, Shan Dong University, 2003
Bachelor of Science, Shan Dong University, 2000

A THESIS SUBMITTED IN PARTIAL FULFILLMENT
OF THE REQUIREMENTS FOR THE DEGREE OF

DOCTOR OF PHILOSOPHY

in

THE FACULTY OF GRADUATE STUDIES
(Physics)

THE UNIVERSITY OF BRITISH COLUMBIA
(Vancouver)

December 2012

Abstract

We tested the feasibility of searching for exotic particle emissions in the decay of trapped Rb isomers by measuring the recoiling momentum of the decay daughters. Massive particle emissions would cause the daughters to recoil at a momentum less than the case of a photon emission, and show up as a lower peak in the recoiling momentum spectrum.

$^{86\mathrm{m}}$Rb isomer decay ($6^- \to 2^-$) was chosen as the experimental subject, which allows a search for 0^+ and 1^- massive particles with a mass range between 0 and 556 keV/c^2. To measure the recoiling momentum of the neutral $^{86\mathrm{g}}$Rb decay daughters, they must first be photoionized to be collected by the spectrometer and detected by the MCP detectors. The photoionization scheme is a two-stepwise procedure, including Doppler-free two-photon transitions from the $5\mathrm{S}_{1/2}$ to $5\mathrm{D}_{5/2}$ states by a 778 nm laser, and from the $5\mathrm{D}_{5/2}$ state into continuum by a 1064 nm laser.

The recoiling momenta of the $^{86\mathrm{g}}$Rb decay daughters were reconstructed by measuring the Rb ions' time-of-flight and transverse displacements on the ion detector. The achieved momentum resolution for the 556 keV/c photoions is 15(3) keV/c, which is twice the expectation due to the sagging of the spectrometer mesh. Because of the photoionization rate limitation, the achieved sensitivity is at 10% decay branch compared to gamma emissions. A feasibility study to improve the sensitivity to 10^{-5} level is outlined and compared to the conventional experiments in this field.

The exotic particle search experiment requires the isotope shift knowledge for efficiently driving Doppler-free two-photon transitions in radioactive Rb isotopes. In total, we measured isotope shifts of the $5\mathrm{S}_{1/2}$ to $5\mathrm{D}_{5/2}$ transition for three Rb isotopes, $\delta\nu^{86\mathrm{m},87} = -69.46(3)$ MHz, $\delta\nu^{86\mathrm{g},87} = -83.62(2)$ MHz and $\delta\nu^{81\mathrm{g},87} = -552.34(27)$ MHz. The precision we achieved in the isotope shift measurements allows us to deduce the specific mass shifts between the $5\mathrm{S}_{1/2}$ and $5\mathrm{D}_{5/2}$ states with 4 – 28 MHz precision by making a King plot. This provides a benchmark for the isotope shift calculations needed for the cosmological tests of time and space variations of the fine structure constant α by astrophysical spectroscopy of alkali-like species.

Table of Contents

List of Tables

List of Figures

Acknowledgments

Most important of all, I would like to express my sincere gratitude to my research advisor, Prof. John Behr, who provides me the opportunity to conduct my PhD studies on such a challenging project. His patience .

I would also like to thank the rest of my thesis committee: Prof. Kirk Madison, Prof. Hirohisa Tanaka and Prof. Valery Milner, for their encouragement, guidance and ...

Dedication

To my angels: Simon and Catherine, my wife and my parents, who offered me unconditional love and supports throughout the course of this thesis.

Chapter 1

Introduction

1.1 Indirect Method for Massive Particle Searches

In the two-body final state of a gamma decay, gamma rays have same momentum as the recoiling nucleus. This would produce a single peak at $p = E/c$ in the momentum spectrum of the recoiling nucleus, where E is the nuclear transition energy. On the other hand, if massive particles are emitted in nuclear transitions instead of photons, the recoiling nucleus will have a lower momentum of $p = \sqrt{(E/c)^2 - m^2c^2}$ and produce a lower peak than E/c in the recoiling momentum spectrum.

Figure 1.1 shows an example of such a peak by simulation, which is an idealization of emitting a 200 keV/c^2 mass particle with $5(1) \times 10^{-5}$ branching ratio in the $^{86\mathrm{m}}$Rb isomer decay. The simulation used random number generators to create two Gaussian profiles for the $^{86\mathrm{g}}$Rb recoiling momenta when emitting 556 keV photons and 200 keV/c^2 mass particles. A 7 keV/c momentum resolution was included in the simulation, which is necessary to find the 200 keV/c^2 mass particle with $5(1) \times 10^{-5}$ branching ratio. The branching ratio is defined as Γ_m/Γ_γ, the ratio of transition rates between the 200 keV/c^2 mass particle emissions ($p = 519$ keV/c) and the gamma emissions ($p = E/c = 556$ keV/c).

In this work we use the indirect method to search for massive particle emissions in nuclear transitions, by measuring the momentum of mono-energetic recoils from nuclear isomer decay using TRIumf's Neutral Atom Trap (TRINAT). This method does not rely on any information about interactions of the particles in any detector, and is independent of the lifetime of the particle. It is unique to atom traps, and could measure the mass of any "invisible" particle produced in nuclear decays with very small backgrounds.

Such an experiment would utilize high-momentum-resolution spectrometer techniques developed for atomic physics experiments in the last decade [1, 2], such as field-free drift spaces for time-of-flight focusing, and electrostatic lenses for transverse momentum focusing to make mo-

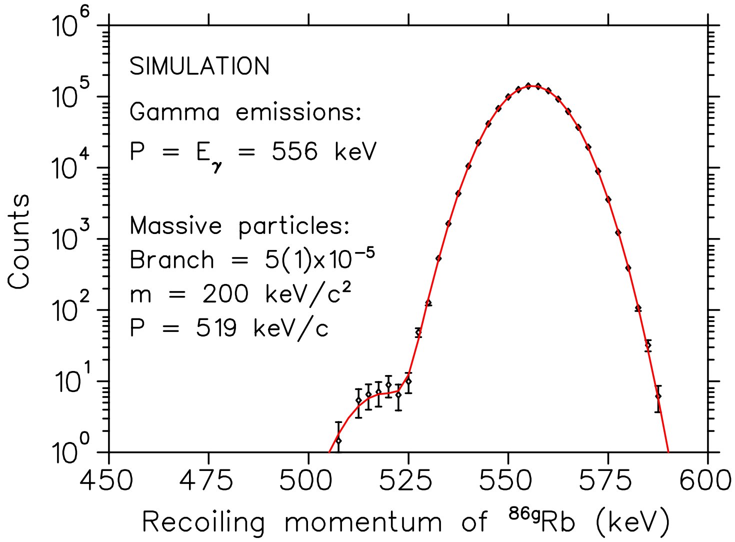

Figure 1.1: Idealization of emitting a 200 keV/c^2 mass particle with $5(1) \times 10^{-5}$ branching ratio in $^{86\mathrm{m}}$Rb isomer decay. A 7 keV/c momentum resolution is necessary in this case to find the 200 keV/c^2 mass particle. The gamma events are centered at $p = 556$ keV/c. The 200 keV/c^2 mass particle is centered at $p = 519$ keV/c.

mentum resolution less dependent on cloud size.

1.2 Candidate Particles

The amplitude of emitting a massive particle during nuclear transitions can be expressed as

$$M = G_{xN\bar{N}} \sum_n < \psi_{fn} | e^{i\vec{q}\cdot\vec{r}_n} | \psi_{in} > \ [3], \tag{1.1}$$

where $G_{xN\bar{N}}$ is defined as the coupling constant between the unknown massive particle to nucleons. ψ_{in} and ψ_{fn} are wavefunctions of the initial and final nuclear states. $\vec{q}$ is the momentum transfer and approximately equals the momentum of the particle ($q^2 \simeq E^2 - m_x^2$). The $e^{i\vec{q}\cdot\vec{r}_n}$ term is the plane wave description of the particle, treated as an operator between the initial and final nuclear wavefunctions.

The multipole expansion for the transition matrix element results in

$$M \propto G_{xN\bar{N}} \left[\langle \psi_{fn} | \psi_{in} \rangle + \langle \psi_{fn} | i\vec{q}\cdot\vec{r}_n | \psi_{in} \rangle \ldots + \frac{1}{l!} \langle \psi_{fn} | (i\vec{q}\cdot\vec{r}_n)^l | \psi_{in} \rangle \right], \tag{1.2}$$

where l is the multipolarity. For multipole transitions with a specific order of l, the transition probability for emitting a massive particle is

$$\Gamma = M^2 \propto \; G^2_{xN\bar{N}} \left\langle \psi_{fn} | (\vec{q} \cdot \vec{r}_n)^{2l} | \psi_{in} \right\rangle . \tag{1.3}$$

So the branching ratio for emitting massive particles depends on the multipolarity l by $(kr)^{2l}$ [4], where $k = q/\hbar$ is the wave number of the particle. $r = r_0 A^{1/3}$ is the radius of the nucleus and $r_0 \simeq 1.2$ fm. The size of kr is much smaller than 1 (for ^{86}Rb, $kr \simeq 1\%$ when $q = 556$ keV/c), so the branching ratio for emitting massive particles decreases by orders of magnitude for higher multipolarities.

The law of angular momentum conservation must be obeyed in nuclear transitions. For a nuclear transition from the J_i to J_f state, the angular momentum that can be taken away by the particle is in the range of $|J_i - J_f| \leq \Delta J \leq |J_i + J_f|$. ΔJ equals the angular momentum of the particle, thus it will be distributed as the spin and orbital angular momentum of the particle, $\Delta J = |\vec{J}| = |\vec{I} + \vec{L}|$. Since $\vec{L}$ can only be integer quantum numbers, the spins of the particle are also integers. So exotic particles that can be potentially emitted in nuclear transitions are recognized as bosons with any integer spins.

Parity is another intrinsic property for the exotic particle that can be determined in nuclear transitions. As a space reflection operation, the parity operator causes the following operation on Bosonic field $\Phi(\vec{x}, t)$ [5],

$$P\Phi(\vec{x}, t)P^{-1} = \eta\Phi(-\vec{x}, t), \tag{1.4}$$

with $\eta = \pm 1$. As an example, when the particle spin is 0, the plus (minus) sign refers to scalar (pseudo-scalar) field. The determination of the particle's parity relies on the transition matrix element, which can only be non zero when $P(\psi_{in}) \cdot P(\psi_{fn}) \cdot P(L) \cdot P(x)$ is positive. $P(\psi_{in})$ and $P(\psi_{fn})$ are the parity of the initial and final nuclear wavefunctions, $P(L) = (-1)^L$ is the parity that relates to particles' orbital angular momentum, and $P(x)$ is the intrinsic parity of the particle. As an example, for an isomeric transition from I^π (spin$^{\text{parity}}$) $= 6^- \rightarrow 2^-$ in ^{86m}Rb, the angular momentum that has to be taken away is $\Delta J = 4, ...8$. For the lowerest-order multipolarity of $M = 4$ and a potential spin-0 particle emission, $P(\psi_{in}) \cdot P(\psi_{fn}) \cdot P(L) = (-1)(-1)(-1)^4 = +$. So the parity of the particle is determined as "+", which is a scalar particle with $\mathrm{I}^\pi = 0^+$ and most favored in this $E4$ transition. The I^π for particles with higher spins can also be deduced using the same rule, but with lower branching ratio comparing to the scalar particle emissions.

In summary, angular momentum selection rules favor production of $\mathrm{I}^\pi = 0^-$, 1^+, 2^-, 3^+, ... particles in magnetic transitions [4], and 0^+, 1^-, ... particles in electric transitions. The branching ratio for these particles is proportional to $(kr)^{2l}$. The 0^+ (or 0^-) scalar particles have the biggest branching ratio and are most favored in nuclear transitions.

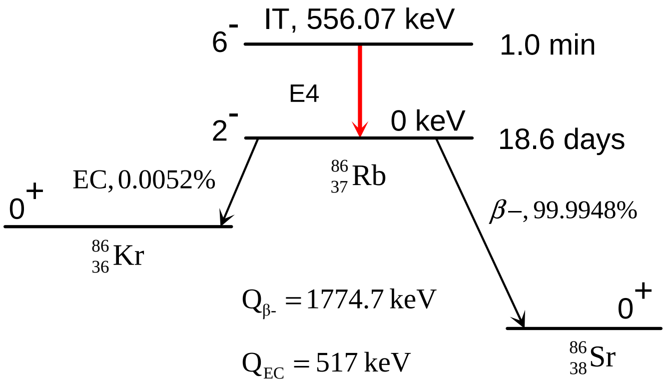

Figure 1.2: $^{86\mathrm{m}}$Rb isomer transition and decay scheme. All data are from the Landolt-Börnstein database.

1.3 ^{86}Rb Isomer Decay

1.3.1 Isomeric Transition

The ^{86}Rb isomer decay is chosen for the exotic particle search experiment. Figure 1.2 shows the decay scheme, which is an $E4$ transition from the 6^- isomer state to the 2^- ground state.

With a 1-minute half-life, $^{86\mathrm{m}}$Rb isomers undergo a two-body isomeric transition with 98% branching ratio by emitting 556 keV photons. This would produce a 556 keV/c peak in the momentum spectrum of the recoiling $^{86\mathrm{g}}$Rb nucleus. In the case of emitting massive particles instead of 556 keV photons, the recoiling momentum of $^{86\mathrm{g}}$Rb will be smaller than 556 keV/c and show up as a lower peak in the momentum spectrum. By measuring the mono-energetic recoiling momentum of the $^{86\mathrm{g}}$Rb decay daughter, we can indirectly search for massive particle emission in nuclear transitions.

This isomer decay has the maximum recoiling momentum among the ones we could detect. It allows the searches for 0^+ (or 1^-) particles within a mass range of 0 – 556 keV/c^2, according to the angular momentum selection rules we discussed in Section 1.2.

1.3.2 Internal Conversions

Besides the gamma decay, $^{86\mathrm{m}}$Rb isomers also undergo internal conversion with about 2% branching ratio [6]. The naturally-occurring internal conversion events can provide very important calibrations for our spectrometer. So details about the internal conversion process are explained in this section.

Figure 1.3 shows the decay scheme of the internal conversion process in $^{86\mathrm{m}}$Rb isomer decay. During the internal conversion process, the wavefunction of the inner-shell electron penetrates the

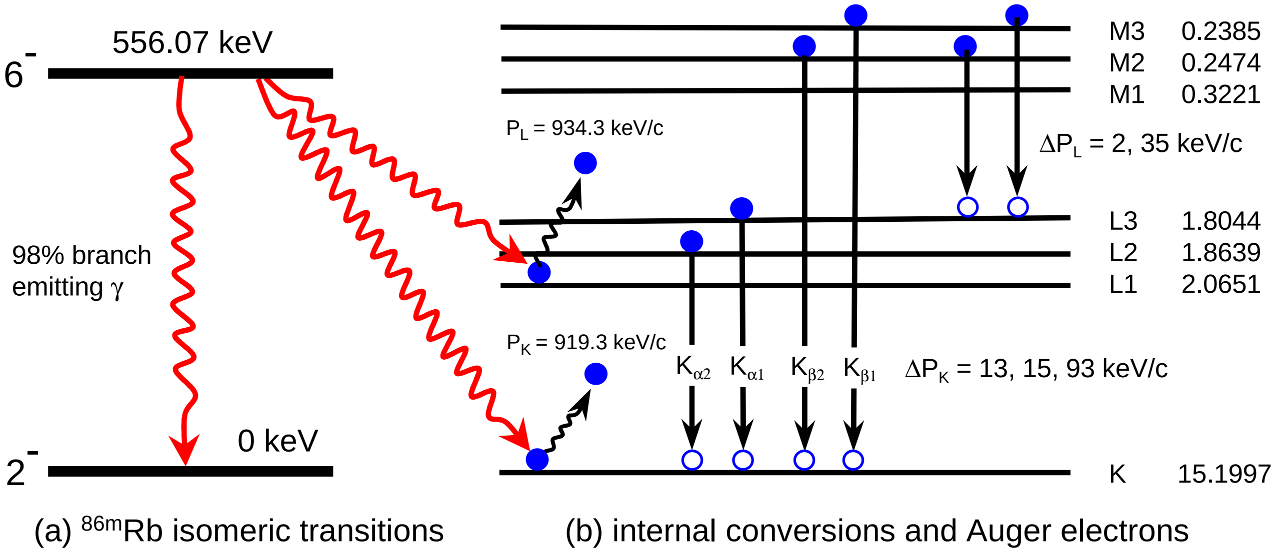

Figure 1.3: Detailed decay scheme of the ^{86m}Rb isomer. (a) ^{86m}Rb isomeric transitions with 98% branching ratio. (b) 2%-branch internal conversion process and the following Auger processes. P_K and P_L are the recoiling momentum of ^{86g}Rb by emitting a K-shell or L-shell electron, respectively. ΔP_K and ΔP_L are momentum broadening for P_K and P_L caused by auger electron or X-ray emissions. All units for the atomic energy levels are in keV.

^{86}Rb nucleus and couples to the 6^- isomer state. The 556 keV nuclear transition energy is taken directly by the electron, which is then ejected out of the atom without emitting a 556 keV photon.

The kinetic energy k_e of the electron emitted from the internal conversion process is equal to the nuclear transition energy minus its atomic binding energy. For a K-shell process, $k_e = 556 - 15.1997 = 541$ keV, which results in a 919.3 keV/c recoiling momentum for the originally trapped ^{86}Rb nucleus, since

$$P_K = P_{e^-} = \sqrt{(k_e + m_e)^2 - m_e^2}. \tag{1.5}$$

Similarly, the L-shell process will emit electrons with $k_e = 554$ keV and result in a different recoiling momentum for Rb ions, $P_L = 934$ keV/c, with approximately 7.3x less probability [7].

The recoiling momentum P_K and P_L by the internal conversion process will be used to calibrate our spectrometer, but the momentum resolution for P_K and P_L has many decay contributions that also need to be taken into consideration. The emission of the inner-shell electrons will leave vacancies in the low shells, which are then filled by high-orbit electrons, accompanied with the release of X-ray photons or Auger electrons. Figure 1.3 (b) shows the filling of the K-shell vacancies by electrons from L shell and M shell, with the emission of K$_\alpha$ and K$_\beta$ photons with energies around 13 – 15 keV, which will broaden the recoiling momentum P_K. The Auger electron emission will create high charge state ^{86}Rb ions, which have much different TOF and transverse displacements as the +1 photoions.

Photons (^{86}Rb)			Auger electrons (^{86}Rb)		
γ_{mode}	γ (keV)	γ (%)†	e_{bin} (keV)	$\langle e \rangle$ (keV)	e (%)
γ (E4)	556.07	98.19	541	8.4	1.56
$K_{\alpha 2}$	13.336	0.307	554	1.2	0.216
$K_{\alpha 1}$	13.395	0.59	556	0.231	0.0415
$K_{\beta 1}$	14.959	0.128			
$K_{\beta 2}$	15.286	0.0136			

† 0.10% uncertainty(syst).

Table 1.1: Photon energies and atomic electron energies emitted during the ^{86}Rb internal conversion process, data from Browne [6]. e_{bin} is the electron kinetic energy from internal conversions, $\langle e \rangle$ is the average kinetic energy of the following Auger electrons, $e(\%)$ is the absolute electron bin intensity.

The Auger electron emissions also cause the ^{86}Rb ions to recoil, on top of the P_K or P_L recoiling momentum. As shown in Table 1.1, the emission of a 541 keV electron will result in Auger electron emission with 8.4 keV average kinetic energy. This corresponds to $\Delta P_K = 93$ keV/c broadening for ions with $P_K = 919.3$ keV/c. The 1.2 keV average kinetic energy after the 554 keV electron emissions results in $\Delta P_L = 35$ keV/c broadening for ions with $P_L = 934$ keV/c.

1.4 Phenomenological Motivations

There are a number of phenomenological motivations for such general searches of massive particles within the mass range of 0 – 556 keV/c^2, including scalar dark matter candidates, U bosons and axions. Although the mass range seemingly have been explored long ago [8], potentially we have sensitivity to very small couplings that are otherwise difficult to constrain.

1.4.1 511 keV Line Emission from the Galactic Center

The central region of the Milky Way Galaxy is illuminated by 511 keV gamma-rays, which are the signature of e^+e^- pair annihilation and have been robustly detected by the INTEGRAL satellite [9]. The origin of the positrons is a subject of much debate.

Conventional astronomy explanations can't explain both intensity and shape of the 511 keV line. The suspected sources include neutron stars, pulsars, supernovae, novae, red giants, etc. More recently, an asymmetric distribution of the positrons in the inner Galactic disk is found to resemble the asymmetry in the distribution of "hard" LMXBs (Low Mass X-ray Binaries), suggesting that they may be the dominant origin of the positrons [10]. However, this evidence is still only suggestive and does not eliminate the need to explore other positron sources.

Explanations of the positron source are also investigated in particle physics, which motivate our searches for massive particles. Those explanations include 0^+ scalar dark matter candidates [11] and 1^- U bosons [12]. Scalar dark matter particle χ with mass in 0.5 MeV – a few MeV range can annihilate into e^+e^- pairs by s-channel decay, $\chi\chi \rightarrow e^+e^-$. This process is mediated by a new $I^\pi = 1^-$ gauge boson U, which can also serve as a candidate particle in our general searches. The constraints on U bosons depend on its mass and production modes [12], which are more stringent for U bosons with lighter masses. The typical branching ratio for U boson production is in the range of 10^{-5} – 10^{-4} [3].

1.4.2 Axions and The Strong CP Problem

The axion is a pseudoscalar particle with $I^\pi = 0^-$. It is originally proposed to solve the strong CP problem. There is no experimentally known violation of the CP-symmetry in Quantum Chromo Dynamics (QCD). However, there is a natural term L_θ in the QCD Lagrangian that is able to break the CP-symmetry, and

$$L_\theta = \theta \frac{g_s^2}{32\pi^2} G\tilde{G} = \theta \frac{g_s^2}{32\pi^2} G_a^{\mu\nu} \tilde{G}_{a\mu\nu} \,. \tag{1.6}$$

This is known as the strong CP problem [13]. Here θ is a phase parameter, g_s is the fine-structure constant of strong interactions. $G_a^{\mu\nu}$ and $\tilde{G}_{a\mu\nu}$ are the color field strength tensor and its dual, respectively. To solve the strong CP problem, a global U(1) symmetry, or the Pecci-Quinn (PQ) symmetry [14, 15], was invoked to replace the static CP-violating angle $\bar{\theta}$ with a CP-conserving field to allow the $\bar{\theta}$ to vanish dynamically. The spontaneous symmetry breaking of the global U(1) symmetry produces a light, long-lived, pseudoscalar Nambu-Goldstone boson – the axion [16].

In the original axion model, the PQ-symmetry breaking scale f_a is assumed to be equal to the electroweak scale. This implies an axion mass of ~ 100 keV/c^2. The original axion model has been ruled out by a variety of laboratory axion searches. New models assumed larger f_a and thus smaller axion masses [17]. However, the constraints in nuclear axion searches are loose, since axions are light enough to be emitted from nuclear transitions.

Direct limit on axions emitted from nuclear transitions appeared from Minowa's experiment [8], which constrains 0^- particles to be emitted with a branching ratio of $\Gamma_a/\Gamma_\gamma < 1.21 \times 10^{-6}$ in the mass range of 26.7 – 166 keV/c^2. The Minowa experiment indirectly searched for axions in the ^{139}La $M1$ transition ($I^\pi = \frac{5}{2}^+ \rightarrow \frac{7}{2}^+$), by measuring the missing signal of the 166 keV gamma (or electrons by internal conversion process) when the preceded x-ray is detected.

The Minowa experiment doesn't limit the 0^+ particles directly, which is favored in the allowed $E2$ transitions. According to Equation 1.3, the branching ratio for emitting 0^- and 0^+ particles are

$$\begin{aligned} \Gamma_{0^-}(M1) &\propto (kr)^2 G^2_{0^- N\bar{N}}, \\ \Gamma_{0^+}(E2) &\propto (kr)^4 G^2_{0^+ N\bar{N}}. \end{aligned} \tag{1.7}$$

The the ratio between them is

$$\frac{\Gamma_{0^+}}{\Gamma_{0^-}} = (kr)^2 \left(\frac{G_{0^+ N\bar{N}}}{G_{0^- N\bar{N}}}\right)^2 \simeq 10^{-4} \left(\frac{G_{0^+ N\bar{N}}}{G_{0^- N\bar{N}}}\right)^2, \tag{1.8}$$

since $(kr)^2 \simeq 1\%$ for the $\frac{5}{2}^+ \to \frac{7}{2}^+$ transition in ^{139}La. So the constraint on the 0^+ particle coupling strength is 100x lower than the constraint on the 0^- particle.

1.4.3 Massive Particles and Astrophysics

There are many indirect constraints from astrophysics on new massive particles in this mass region, both from cosmology and from stellar evolution. These constraints have some dependence on cosmological paradigms. As such, it is usually helpful to have direct constraints from experiments on such particles.

New massive particles with large enough couplings to matter might be created in too-large abundance in the early universe, causing unaccepable changes in the total mass density. New relativistic particles with small couplings, because of their relatively unconstrained motion in the early universe, can produce conflict with observations of large-scale structure of galaxies and the cosmic microwave background.

One way to avoid the indirect cosmological constraints is to have a cooler Big Bang, which avoids producing too many of these particles. After inflation ended, the universe was cold. However, in order for Big Bang Nucleosynthesis (BBN) to occur, it must have been heated by some mechanism. All that is known from overvations is that it must have been heated to a temperature on the order of MeV. Typically mechanisms are found to heat it much hotter to produce the baryon asymmetry, though there are mechanisms that work at low temperature [18]. In low-reheating scenarios, many fewer particles are produced for a given coupling, so particle couplings can be much larger without disturbing BBN and other cosmological constraints [19, 20]. The mass density of such particles can also produce indirect perturbations on Big-Bang Nucleosynthesis, especially the primordial ratio of helium to hydrogen [19, 20]. The scalar particle theorized to explain both the galactic center 511 keV radiation and the dark matter has been given properties, including mass and coupling strengths, consistent with these other astrophysics constraints without needing the low-reheating scenario [21].

There are also serious constraints from stellar evolution. Weakly coupled particles can carry away too much energy from the star, thus change the stellar evolution. These constraints have less model dependence and are very restrictive for coupling light particles below $\sim$ 30 keV/c^2. Above this mass, the limit on the coupling strength degrades quickly as the the emission is suppressed when the particle mass exceeds the stellar temperature [22].

1.5 Feasibility Test of Exotic Particle Searches in ^{86}Rb isomer decay

The ^{86}Rb isomer decay allows the searches for 0^+ (or 1^-) particles within a mass range of 0 – 556 keV/c^2. The sensitivity to massive particles is defined as the upper limits of Γ_m/Γ_γ, the branching ratio of the massive particle emissions with respect to the 556 keV/c gamma events. To be competitive with the conventional experiments in this field [8], our sensitivity to exotic particles needs to be at the 10^{-6} – 10^{-4} level.

Details of the exotic particle search experiment in ^{86}Rb isomer decay are summarized in Chapter 3 and Chapter 5, which cover the experimental setup and results, respectively. Due to the inefficient photoionization of the fast-moving decay daughters, the sensitivity level we achieved is only at 10%, which is not sensitive enough for searching the proposed exotic particles. However, we collected about 150 gamma recoils, and found the gamma-event peak at 556 keV/c on the $^{86\mathrm{g}}$Rb recoiling momentum spectrum. The achieved momentum resolution is about 15 keV/c, which limits the sensitivity of searching for massive particles with $m < 150$ keV/c^2. We also outlined the feasibility of improving the current 10% sensitivity to 10^{-5} level by fixing the sagging spectrometer mesh and optimizing photoionization efficiency.

1.6 Specific Mass Shift in Rb Isotopes

The exotic particle search experiment requires the isotope shift knowledge of the $5\mathrm{S}_{1/2}$ to $5\mathrm{D}_{5/2}$ transition for radioactive Rb isotopes, to efficiently drive the Doppler-free two-photon transitions (details discussed in Section 3.2.2). For this purpose, we measured the related isotope shifts in three Rb isotopes, $^{86\mathrm{m}}$Rb, $^{86\mathrm{g}}$Rb and $^{81\mathrm{g}}$Rb. The results are shown in Chapter 6.

The precision we achieved in the isotope shift measurements allows us to deduce the specific mass shifts between the $5\mathrm{S}_{1/2}$ and $5\mathrm{D}_{5/2}$ states with 40% precision (absolute precision in 4 – 28 MHz range), as well as the specific mass shift constant of 77(33) GHz·amu. These also provide a benchmark for isotope shift calculations that are needed for the cosmological tests of the time and space variation of the fine structure constant α by astronomical spectroscopy in alkali or alkali-like species.

1.6.1 Isotope Shift Theory

Isotope shifts are the atomic transition energy difference between isotopes, which can be separated into two parts: the field shift and the mass shift.

The field shift arises from the finite size of the nuclear charge distribution, which induces a transition frequency difference between isotopes [23]:

$$\delta\nu_F^{AA'} = -\frac{\pi a_0^3}{Z}\cdot\Delta|\psi(0)|^2\cdot f(Z)\cdot\delta\langle r^2\rangle^{AA'}, \tag{1.9}$$

where $\Delta|\psi(0)|^2$ is the change of the electron charge density at the nucleus between the lower and upper states of the optical transition, $\delta\langle r^2\rangle^{AA'}$ is the difference between the nuclear charge radii of isotopes A and A', and $f(Z)$ is a function of the atomic number Z that is roughly proportional to Z^2 for light elements [23].

The additional kinetic energy of the recoiling nucleus also induces energy level shifts, which is referred to as the mass shift. $\Delta E_k = \vec{p}^2/2M = (\sum_i \vec{p_i})^2/2M$, where $\vec{p}$ and M are the momentum and mass of the nucleus, $\vec{p_i}$ is the momentum of the ith electron, and the summation is over all the electrons due to momentum conservation. ΔE_k can be separated into two parts:

$$\Delta E_k = \frac{1}{2M}\sum_i \vec{p_i}^2 + \frac{1}{M}\sum_{i\neq j}\vec{p_i}\cdot\vec{p_j}\ . \tag{1.10}$$

The first term can be evaluated exactly. For isotopes with masses m_A and $m_{A'}$, the difference of the first term is defined as the normal mass shift $\Delta E_{NMS}^{AA'}$ and can be expressed as

$$\Delta E_{NMS}^{AA'} = h\nu_{A'}\frac{m_e(m_A - m_{A'})}{m_{A'}(m_A + m_e)} = h(\nu_A - \nu_{A'}), \tag{1.11}$$

where ν_A and $\nu_{A'}$ are the transition frequencies in those isotopes. Evaluation of the second term in Equation 1.10 is very difficult since it contains the momentum correlations between all the electrons. The transition energy shift between isotopes caused by this term is called the specific mass shift.

In general, the isotope shift between isotopes with mass number A and A' can be expressed as

$$IS^{AA'} = \frac{A - A'}{AA'}(N + S) + F\cdot\delta\langle r^2\rangle^{AA'}, \tag{1.12}$$

where F is the field shift constant, N and S are the normal mass shift constant and specific mass shift constant, respectively.

1.6.2 General Motivations

Optical isotope shifts provide precise tests of atomic and nuclear structure. For alkali-like species, isotope shifts have been evaluated by astronomical observations of optical transitions for searching the time and space dependence of the fine structure constant α [24]. In addition, isotope shift measurements help to determine the nuclear charge distribution [25, 26], and accurate transition frequencies are also needed for decay studies of radioactive isotopes [27].

These applications require good knowledge of the specific mass shift, which is difficult to calculate for atoms with more than one valence electron, but can be deduced by high precision transition frequency measurements. Typical errors for the best calculations are around 30 MHz, such as the specific mass shift calculations between S and D states in K, Ca^+ and Ba^+ [28], and in Sr^+ [29]. The Sr^+ calculation was tested by the specific mass shift measurement of the $5\mathrm{S}_{1/2}$ to $4\mathrm{D}_{5/2}$ transition [29]. This most recent investigation of the specific mass shift calculations can also be done in our case of the Rb $5\mathrm{S}_{1/2}$ to $5\mathrm{D}_{5/2}$ transition.

In general, the specific mass shift is a huge effect in very light nuclei, unless the recoiling momenta of the nucleus cancel due to the symmetry of atomic valence electrons. In lithium, the specific mass shift is of similar size to the normal mass shift, which are both 10,000x larger than the field shift [26]. In potassium, it is 20% of the normal mass shift. In francium, it is tiny and can be ignored. The specific mass shift in Rb was assumed to be zero for the charge radius measurements [30]. For the determination of the $^{74}\mathrm{Rb}$ charge radius [31], which is far from the line of stability and therefore more sensitive to mass shifts, the mass shift constant had to be estimated more carefully from the established phenomenology: the previously measured muonic X-rays and a more modern calculation of the field shift. Our measurement is not directly related to the Rb D2 transition, but generally supports the very difficult specific mass shift calculations.

1.7 Dissertation Outline

This dissertation is divided into 6 chapters.

Chapter 1 explains the motivation and experimental method for the massive exotic particle search in nuclear gamma decay, and the reason for choosing $^{86\mathrm{m}}\mathrm{Rb}$ isomer decay as the experimental subject. We will also motivate the measurement of the isotope shift in radioactive Rb isotopes, as well as the related theoretical backgrounds.

Chapter 2 introduces the atomic physics utilized in this experiment, including the magneto-optical trap, the Doppler-free two-photon transition technique and the power buildup cavity.

Chapter 3 discusses the experimental setup for searches of exotic particle emission in the decay of trapped $^{86\mathrm{m}}\mathrm{Rb}$ isomers, which includes cooling and trapping of $^{86\mathrm{m}}\mathrm{Rb}$ using the TRINAT double MOT system, the photoionization scheme and optical setup for photoionizing the fast-moving decay daughters, and the detector system for measuring the time-of-flight and transverse displacements for $^{86\mathrm{m}}$Rb decay daughters.

Chapter 4 summarizes the time-of-flight simulations using SimIon, including the momentum calibrations for the designed spectrometer, correcting ions' trajectory deflection by the quadrupole magnetic field, and the momentum resolution estimation based on the design.

Chapter 5 summarizes the results of the exotic particle search experiment. In this chapter, I will show the time-of-flight spectrum and ion MCP 2D images for the +1 photoions and the internal conversion events with higher charge states. I will explain the inconsistency in ions' transverse displacements between the experimental value and the simulation, which is caused by the sagging of the 40 mm spectrometer mesh. I will also reconstruct the recoiling momentum for +1 photoions and +4 internal conversion events based on the experimentally-improved momentum calibrations, and perform a massive particle search by scanning through the momentum spectrum of +1 photoions. At the end of this chapter, I will discuss the reasons for the low photoionization rate problem, explain the attempt to search for massive particle emissions in the decay of trapped $^{81\mathrm{m}}$Rb isomers, and show the results of the power buildup cavity tests.

Chapter 6 summarizes the results of the Doppler-free two-photon spectroscopy between the $5S_{1/2}$ and $5D_{5/2}$ states in radioactive Rb isotopes ($^{86\mathrm{m}}$Rb, $^{86\mathrm{g}}$Rb and $^{81\mathrm{g}}$Rb), as well as the analysis on specific mass shifts based on the deduced isotope shifts.

Chapter 2

Atomic Theory

Three important techniques from atomic physics are utilized in the exotic particle search experiment, the magneto-optical trap, the Doppler-free two-photon transition technique, and the power buildup cavity. The related theories are outlined in this chapter.

2.1 Magneto-optical Trap

After the invention in the 1980s, the method of laser cooling and trapping has been used as a source for laser cooled atoms to study atomic physics and to produce dilute quantum degenerate gases. It provides a platform for a variety of modern physics experiments, such as high-resolution laser spectroscopy, the experimental realization of the Bose-Einstein condensation, and the study of many-body quantum mechanics. The principle of the MOT is shown in Figure 2.1, which includes a three-dimensional optical molasses and a quadrupole magnetic field.

2.1.1 Optical Molasses

When near-resonance light is shone onto an atom, the atom absorbs the photons and its momentum changes due to the law of momentum conservation. The change of momentum induces a force on the atom, the scattering force [32], F_{scatt}:

$$F_{scatter} = \pm\hbar k \, \frac{\Gamma}{2} \, \frac{I/I_{sat}}{1 + I/I_{sat} + 4(\delta \mp kv)^2/\Gamma^2} \equiv F_{\pm}, \tag{2.1}$$

where $\hbar k$ is the momentum of the photon with no doppler shift, Γ is the decay rate of the excited state, I is the laser intensity and I_{sat} is the saturation intensity of the excited state, $\delta = \omega - \omega_0$ is the frequency detuning between the laser frequency ω and the atomic resonance frequency ω_0. The "±" signs correspond to the atom's direction being parallel/antiparallel to the photon.

The experimental realization of a one-dimensional optical molasses is one pair of counter-

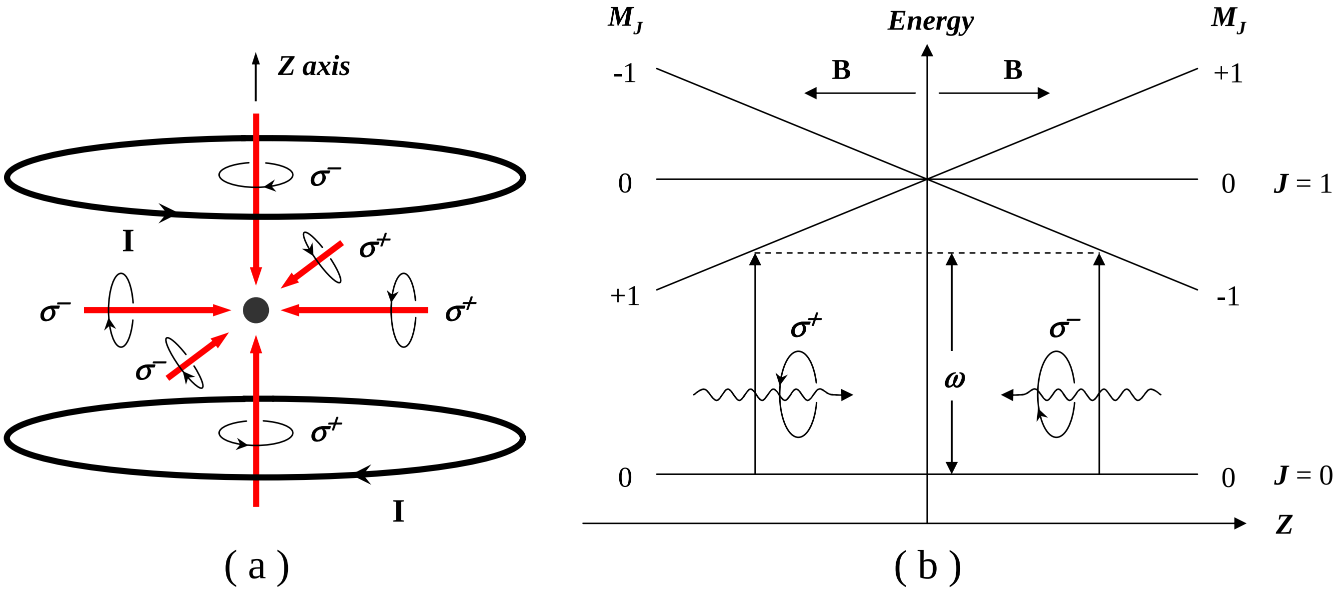

Figure 2.1: Principle of the magneto-optical trap. (a) the MOT diagram, (b) the energy diagram of a two level atom.

propagating laser beams with the same frequency ω, which is slightly red-detuned to the atomic resonance frequency ω_0 by an amount δ. Atoms moving in the molasses will see photons from both directions. According to the Doppler effect, the photon's frequency will be blue-shifted if the atom moves towards it, and red-shifted if moving away from it. The frequency of the blue-shifted photon gets closer to the atom's resonance frequency and will be more likely absorbed by the atom. On the contrary, the frequency of the red-shifted photon is further red-detuned relative to ω_0 and will be less likely absorbed by the atom. The absorption of a near-resonance photon drives the atom to the excited state. Then the atom undergoes spontaneous decays, which are random in all directions. The recoiling momenta by the spontaneous decays will average to zero after many cycles. However, the recoiling momenta caused by absorbing photons have well-defined directions: same direction for absorbing the red-shifted photons, and opposite direction for absorbing the blue-shifted photons. Since the atoms are more likely to absorb the blue-shifted photon, the total recoiling momentum applied by the optical molasses leads to a damping force that slows the atom down, the optical molasses force. With the assumptions of low atomic velocities $kv \ll \Gamma$ and low laser intensity $I \ll I_{sat}$, the expression of the damping force can be written as [32]:

$$F_{molasses} = F_+ + F_- \cong \frac{8\hbar k^2 \delta \vec{v}\ I/I_{sat}}{\Gamma(1 + 4\delta^2/\Gamma^2)^2}, \tag{2.2}$$

where $\delta < 0$, and the direction of $F_{molasses}$ opposes the atom's velocity and viscously damps its motion.

It is straightforward to generalize the optical molasses from one dimension to three dimensions by aligning three orthogonal retro-reflecting laser beams along the Cartesian axes. All beams are from the same laser and have the same red-detuned frequency, as shown in Figure 2.1(a). In the crossing region of all six beams, atoms moving in any direction will experience a damping force and be slowed down if $kv \ll \Gamma$.

Although the recoiling momenta from the spontaneous decay will average to zero, the fluctuations about the mean (which increase as more photons are scattered) produce a residual heating of the atomic cloud. When this reheating effect balances out the cooling effect of the laser, the atoms temperature is unchanged. The lowest temperature expected in the optical molasses technique is called as the Doppler cooling limit T_D, and

$$T_D = \frac{\hbar\Gamma}{2k_B}. \tag{2.3}$$

For rubidium $T_D = 143\ \mu\text{K}$, which corresponds to a most probable velocity of 12 cm/s.

2.1.2 Quadrupole Magnetic Field

The optical molasses only cools atoms in the laser crossing region, but does not trap them. The atoms can still diffuse out of the cooling region after some considerable amount of time. By addition of a quadrupole magnetic field and a special arrangement of the beam polarizations, the atoms can be trapped by the scattering force imbalance of the laser beams, which is caused by the magnetic field gradient.

The principle of the MOT [32] is shown in Figure 2.1. The quadrupole magnetic field is created by a pair of anti-Helmholtz coils, which produces a zero B field in the center. The field magnitude increases linearly in all three dimensions to a size much bigger than the trap. The linear B field causes the degenerate hyperfine energy levels to split into Zeeman sublevels, as shown in Figure 2.1 (b). The transition is a simple $J = 0$ to $J = 1$ transition. If the atom moves away from the trap center along the $+z$ direction, the σ^- photon will be absorbed by driving the atom from the $J = 0$ state to the $M_J = -1$ sublevel of the $J = 1$ state. So the scattering force points to the trap center and pushes the atom back. A similar process also occurs for atoms moving in the $-z$ direction. In summary, the quadrupole magnetic field acts like a damped harmonic oscillator for the atoms, providing a position-selective trapping force besides the cooling effect of the optical molasses.

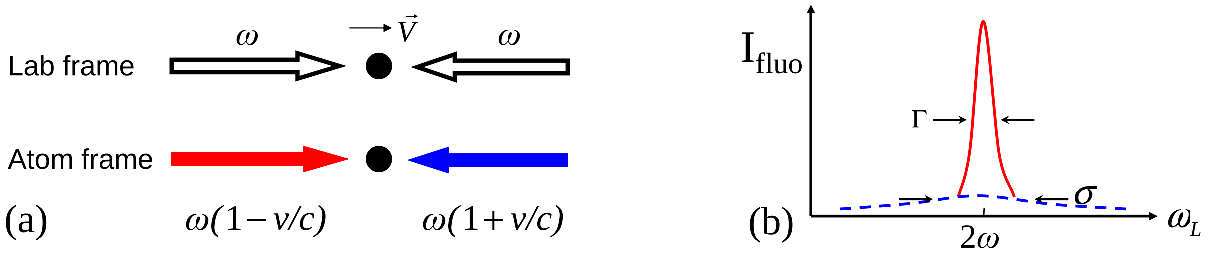

Figure 2.2: Doppler-free Two-photon Transitions. (a) schematic view, (b) typical fluorescence signal.

2.2 Doppler-free Two-photon Transition

2.2.1 Introduction

The principle of the Doppler-free two-photon transition is shown in Figure 2.2(a). An atom flying with velocity $\vec{V}$ simultaneously absorbs two counter-propagating photons with the same frequency ω and gets excited. In the atom's rest frame, the frequencies of these two photons are Doppler-shifted due to the velocity component v of the atom along the laser beam, which become to be "$\omega(1 \pm v/c)$" depending on whether the atom moves towards (+) or away (–) from the laser light. Then the total energy absorbed by the atom is

$$\hbar[\omega(1+v/c)+\omega(1-v/c)] = 2\hbar\omega, \tag{2.4}$$

and the frequency sum of the blue and red-detuned photons in the rest frame of the atom is independent of the atom's velocity. This leads to two important properties:
(1) the signal of this system does not exhibit Doppler broadening, i.e., Doppler-free;
(2) each atom in the system, regardless of its velocity, can contribute to the two-photon transition signal.

A typical fluorescence signal from the Doppler-free two-photon transition is shown in Figure 2.2(b), which includes a well-resolved two-photon signal on top of a wide Doppler profile. Although the two-photon signal is "Doppler-free", there's a small velocity-dependent profile which comes from absorbing two photons from the same direction. Moreover, the second-order relativistic Doppler shift is always "+" and will not be canceled in any case:

$$\omega = \omega_0\sqrt{\frac{1 \pm v/c}{1 \mp v/c}} \simeq \omega_0\left[1 \pm v/c + \frac{1}{2}(v/c)^2 + ...\right]. \tag{2.5}$$

In the exotic-particle search experiment, the maximum recoiling velocity is about 2 km/s for the ^{86g}Rb decay daughters, which corresponds to the 556 keV/c recoiling momentum after the

^{86}Rb isomeric transition. The two-photon transition frequency between the 5S$_{1/2}$ to 5D$_{5/2}$ states is $\omega_0 = 2\pi c \times (778 \text{ nm})^{-1}$ Hz. Then the maximum second-order Doppler shift is

$$\Delta\omega^{(2)} = \frac{1}{2}\omega_0(\frac{v}{c})^2 = \frac{1}{2} \cdot \frac{2\pi c}{778 \text{ nm}} \cdot (\frac{v}{c})^2 \simeq 60 \text{ kHz}, \tag{2.6}$$

when the Rb atoms fly along the 778 nm laser beam direction. However, this 60 kHz shift doesn't affect the two-photon transition rate for the fast-moving $^{86\text{g}}$Rb too much, since it's much smaller than the 330 kHz natural linewidth of the 5D$_{5/2}$ state (in the two-photon scheme). Moreover, the experimental two-photon transition linewidth is more than 1 MHz (details will be discussed in Chapter 6).

In the Doppler-free two-photon spectroscopy measurements, the Rb atoms are trapped in a MOT and their velocities are almost 0. So the second-order Doppler shifts are negligible and will be ignored for the systematic error analysis in chapter 6.

2.2.2 Transition Rate

The two-photon transition rate between the atomic ground state g and the excited state n can be obtained using time-dependent perturbation theory [33]:

$$R^{(2)}_{ng}(\omega) = \left| \sum_m \frac{\mu_{nm}\mu_{mg}E^2}{\hbar^2(\omega_{mg} - \omega)} \right|^2 2\pi \, \rho(\omega_{ng} - 2\omega), \tag{2.7}$$

where E and ω are the electric field amplitude and frequency of the driving laser, $\tilde{E}(t) = E(e^{-i\omega t} + e^{+i\omega t})$; ω_{mg} is the angular frequency difference between any intermediate state m and the ground state g; μ_{nm} and μ_{mg} are the transition dipole matrix elements between any intermediate states m and atomic states n and g, respectively.

The two-photon transition rate also depends on the atom's natural decay rate Γ, as the function of a Lorentzian profile:

$$\rho(\omega_{ng} - 2\omega) = \frac{1}{\pi} \frac{\Gamma/2}{(\omega_{ng} - 2\omega)^2 + (\Gamma/2)^2}. \tag{2.8}$$

Obviously, if the driving laser ω is on resonance with the two-photon transition frequency $\omega_{ng}/2$, the transition rate will be maximized and $\propto 1/\Gamma$.

Γ could be broadened for lots of reasons, such as Zeeman broadening, power broadening, and transit-time broadening. The transit-time broadening dominates in the reference vapor cell and the ^{86}Rb experiment, while the transit-time broadening and the Zeeman broadening contribute the most for the ^{81}Rb experiment.

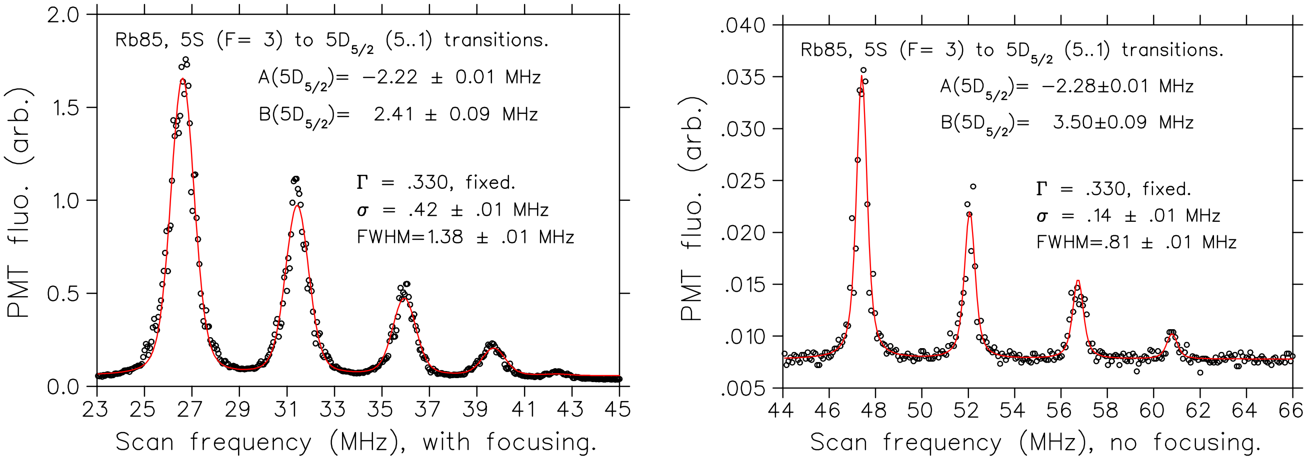

(a) with the focusing lens

(b) without the focusing lens

Figure 2.3: Test of the transit-time broadening effect in a Rb vapor cell, based on the $5S_{1/2}$ to $5D_{5/2}$ transition spectra of ^{85}Rb. The natural linewidth of the $5D_{5/2}$ state is fixed as $\Gamma = 0.33$ MHz in the curve fitting using Voigt profiles. (a) with focusing lenses, (b) without focusing lenses.

2.2.3 Transit-time Broadening

Transit-time broadening σ_t is inversely proportional to the transit time of atoms crossing a laser beam.

$$\sigma_t = u/w \tag{2.9}$$

in angular frequency units [34], where $u = \sqrt{2k_BT/m}$ is the most probable velocity and w is the $1/e^2$ beam radius for a Gaussian laser beam in a TEM00 mode.

We have tested the transit-time broadening effect in a Rb vapor cell, under the same experimental conditions as Section 3.2.3. Since $u \simeq 250$ m/s for Rb gas at 60 °C and $w \simeq 100\ \mu m$, the expected transit-time broadening is 0.4 MHz, which agrees well with our measurement of 0.44(1) MHz, as shown in Figure 2.3 (a). We also tested the effect at a much bigger beam radius of $w \simeq 0.4$ mm, by removing the focusing lenses besides the vapor cell. The result of $\sigma_t = 0.14(1)$ MHz is shown in Figure 2.3 (b), which also agrees well with the expected 0.1 MHz transit-time broadening. The spectra in Figure 2.3 were fitted by the Voigt profile, which is a convolution of the Lorentzian and the Gaussian profiles (details will be discussed in Chapter 6). During the curve fitting, the 0.33 MHz natural linewidth of the $5D_{5/2}$ state was fixed as the Lorentzian linewidth Γ. Based on the spectrum analysis in Figure 2.3, we concluded that the transit-time effect caused by atom's thermal velocity was the dominating broadening mechanism in the vapor cell, since the transit-time broadening dominated in the Gaussian linewidth σ as an inhomogeneous line broadening.

The expected transit-time broadening for the 556 keV/c decay daughters is $\sigma_t = 0.6$ MHz, since their recoiling speed is $u = 2$ km/s and the beam radius for the 778 nm light is $w \simeq 0.5$ mm.

This contributes additional broadening to the $^{86\mathrm{g}}$Rb linewidth that we measured in Chapter 6.

2.2.4 Selection Rules

The transition dipole matrix elements in $R_{ng}^{(2)}$ characterize the interaction strength between the atoms and near-resonant optical radiation, which take the form of $\langle F, m_F | e\vec{r} | F', m'_F \rangle$ to couple two hyperfine sublevels $|F, m_F\rangle$ and $|F', m'_F\rangle$. The calculation of these matrix elements involves the reduction from the dependence on F and m_F quantum numbers to L, S, J quantum numbers using the Wigner-Eckart theorem [35].

The two-photon operator is defined by [36]

$$Q_{\vec{\epsilon_1}\vec{\epsilon_2}} = \frac{\vec{D}\vec{\epsilon_1}\,\vec{D}\vec{\epsilon_2} + \vec{D}\vec{\epsilon_2}\,\vec{D}\vec{\epsilon_1}}{2\hbar(\omega - \omega_0)}, \tag{2.10}$$

where $\vec{D}$ is the electric dipole moment operator, ϵ_1 and ϵ_2 are the polarizations of the two oppositely propagating traveling waves. Q is symmetrical since $Q_{\vec{\epsilon_1}\vec{\epsilon_2}} = Q_{\vec{\epsilon_2}\vec{\epsilon_1}}$, and is a sum of a scalar operator with rank $k = 0$ and a quadrupolar operator with rank $k = 2$.

If $Q_{\vec{\epsilon_2}\vec{\epsilon_1}}$ is scalar, the line intensity $I_{ge}(F_g, F_e)$ for two-photon transitions between hyperfine sublevel F_g and F_e is

$$I_{ge}(F_g, F_e) \sim (2F_g + 1)\delta_{F_g,F_e}, \tag{2.11}$$

which is proportional to the degeneracy of the subspace F_g or F_e. The selection rules for the hyperfine quantum number F are $\Delta F = 0$ and $\Delta m_F = 0$, for J they are $J_e = J_g$ and $J_e = 0$ or 1/2.

If $Q_{\vec{\epsilon_2}\vec{\epsilon_1}}$ is quadrupolar, the line intensity is

$$I_{ge}(F_g, F_e) \sim (2F_g + 1)(2F_e + 1) \begin{Bmatrix} J_e & 2 & J_g \\ F_g & I & F_e \end{Bmatrix}^2 /(2I + 1), \tag{2.12}$$

where the $\begin{Bmatrix} J_e & 2 & J_g \\ F_g & I & F_e \end{Bmatrix}$ is the Wigner $6j$ symbol. All components in the $6j$ symbol are defined for integers and half integers, whose triads must satisfy the triangular inequalities for the $6j$ symbol to be non-0, such as $|J_e - J_g| \leq 2 \leq (J_e + J_g)$, or $|F_e - F_g| \leq 2 \leq (F_e + F_g)$.

2.3 Power Buildup Cavity

The main component of a power buildup cavity is the Fabry-Perot etalon [37], as shown in Figure 2.4. A laser with a wavelength of λ and an electric field of $E_0 e^{i(\mathbf{k}\cdot\mathbf{r} - \omega t)}$ is coupled into the

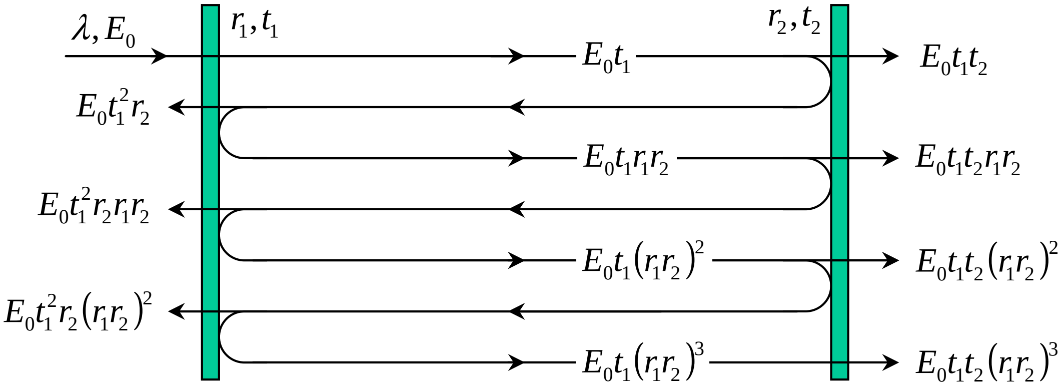

Figure 2.4: Principle of the Fabry-Perot etalon. r_1 and t_1 (r_2 and t_2) are the E-field reflectivity and transmission of the input (output) coupler, respectively.

cavity. After each cycle the laser will be reflected on mirror 1 and 2 once, and the electric field will decrease by a factor of $r_1 r_2$. If the cavity length L is adjusted to satisfy $L = n\lambda/2$, where n is any positive integer, then the E-fields of all cycles will add constructively and a standing wave will be formed inside the cavity. The total electrical field inside the cavity is thus

$$E_{cavity} = E_0 t_1 + E_0 t_1 (r_1 r_2)^2 + E_0 t_1 (r_1 r_2)^3 + ... = \frac{E_0 t_1}{1 - r_1 r_2}, \tag{2.13}$$

where r_1 and t_1 are the E-field reflectivity and transmission of the input coupler, respectively. r_2 is the E-field reflectivity of the output coupler. Then the power buildup ratio is

$$B = \left| \frac{E_{cavity}}{E_0} \right|^2 = \frac{T_1}{(1 - r_1 r_2)^2}. \tag{2.14}$$

Besides the circulating E-field inside the cavity, we can also deduce the field reflected by the input coupler E_R and the field transmitted through the cavity E_T.

$$E_R = E_0 t_1^2 r_2 + E_0 t_1^2 r_2 r_1 r_2 + E_0 t_1^2 r_2 (r_1 r_2)^2 + ... = \frac{E_0 t_1^2 r_2}{1 - r_1 r_2}, \tag{2.15}$$

$$E_T = E_0 t_1 t_2 + E_0 t_1 t_2 r_1 r_2 + E_0 t_1 t_2 (r_1 r_2)^2 + ... = \frac{E_0 t_1 t_2}{1 - r_1 r_2}. \tag{2.16}$$

Obviously, $E_R = E_{cavity}\, t_1 r_2$ and $E_T = E_{cavity}\, t_2$.

Optical finesse is defined as the ratio between the free spectral range $c/(2L)$ and the width of the transmission peak. For a two-mirror cavity, the cavity finesse is given by

$$F = \frac{\pi (R_1 R_2)^{1/4}}{1 - \sqrt{R_1 R_2}}, \tag{2.17}$$

where $R_1 = r_1^2$ and $R_2 = r_2^2$ are the power reflectivity of the input and output coupler, respectively.

Chapter 3

Experimental Setup of The Exotic Particle Searches

In this chapter, the experimental setup for searching the exotic particles is described. It can be divided into four sub-systems: the MOT (magneto-optical trap) system for cooling and trapping of the radioactive isomer isotopes, the photo-ionization system for photoionizing the fast-moving decay daughters, the detection system for photo-electrons and photo-ions, and the data acquisition system.

In the last section, I will also estimate the event rate for ^{86}Rb isotopes, based on the experimental conditions discussed in this chapter.

3.1 General Setup

The experimental setup is shown in Figure 3.1 and 3.2. Figure 3.1 shows the detailed setups of the recoiling momentum measurement. This includes the experimental principles and geometries of the detection chamber and the spectrometer, and positions of the electron detector and ion detector. Figure 3.2 shows the TRINAT double MOT setup for trapping Rb isotopes.

3.1.1 Experimental Method

To measure the recoiling momentum precisely, it is best to work in the center-of-momentum frame. So the first step of the experiment is to trap the ^{86}Rb isomer atoms in a MOT, which cools the isomer atoms down to 0.1 m/s and confines them in a 1 mm diameter cloud.

The trapped ^{86}Rb isomers undergo a two-body isomeric transition, by emitting a 556 keV photon with a 1-minute half-life. The neutral decay daughters recoil at a momentum with the same magnitude as the photon energy. To measure their recoiling momentum, the neutral decay daughters have to be photo-ionized so that they can be collected by the electric field and gain

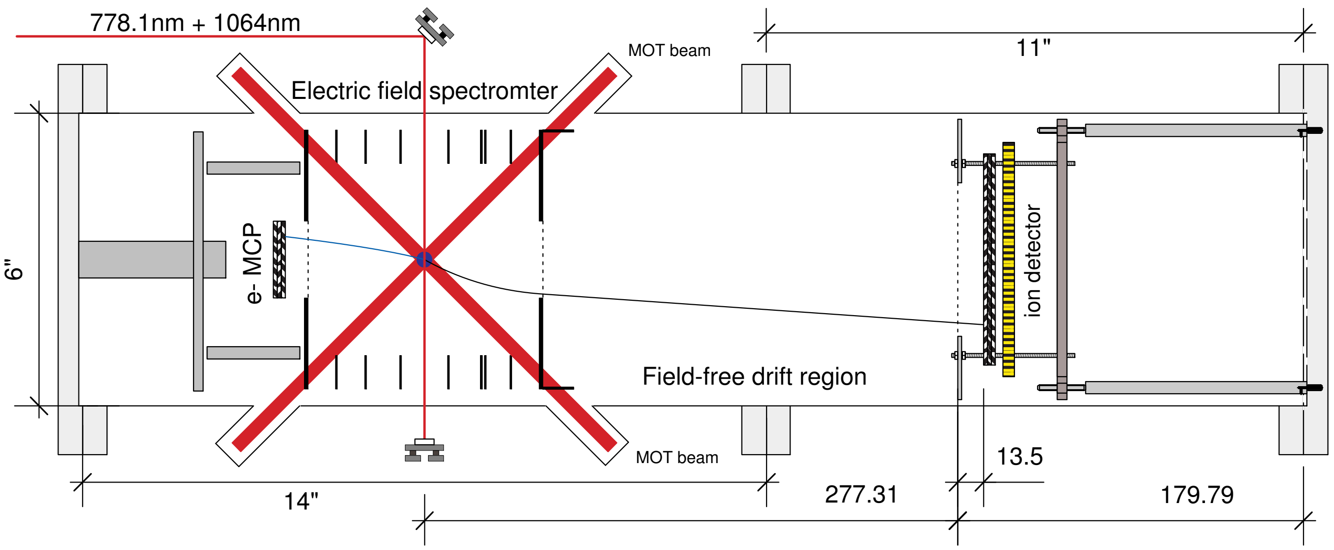

Figure 3.1: General experimental setups and geometries for recoiling momentum measurement. Units in mm unless specified. There are three copper meshes used, as indicated by a dashed line. A 40 mm mesh in front of the e$^-$ MCP detector, another 40 mm mesh separating the spectrometer field from the field-free region, and a 80 mm mesh in front of the ion MCP detector.

enough energy to fire the MCP detector (micro-channel plate). The photo-ionization scheme includes a Doppler-free two-photon transition from $5S_{1/2}$ to $5D_{5/2}$ states by a 778 nm laser, and a second 1064 nm laser is combined with the 778 nm laser to photoionize atoms from the $5D_{5/2}$ state into the continuum.

The electrostatic spectrometer is designed to collect photo-ions flying any direction and focus all of them onto the ion MCP detector, and send photo-electrons to the e$^-$ MCP detector. In addition, with a field-free drift space in the ion arm, the spectrometer has time focusing and momentum focusing capabilities which are critical for achieving high resolution in the recoiling momentum reconstruction.

After the photoions fire the ion MCP, their transverse positions on the MCP plate will be detected by a DLD80, a commercial delay-line-anode detector. The time-of-flight of the photoions is measured by the time coincidence between the photo-electrons and photo-ions, which has a specific range and can also be used to distinguish photoions from background events.

The recoiling momenta of the decay daughters are then reconstructed from the TOF of the photoions and their transverse positions on the ion MCP. More specifically, the photoion's TOF is proportional to the longitudinal component of the recoiling momentum, and the transverse position is proportional to the transverse component.

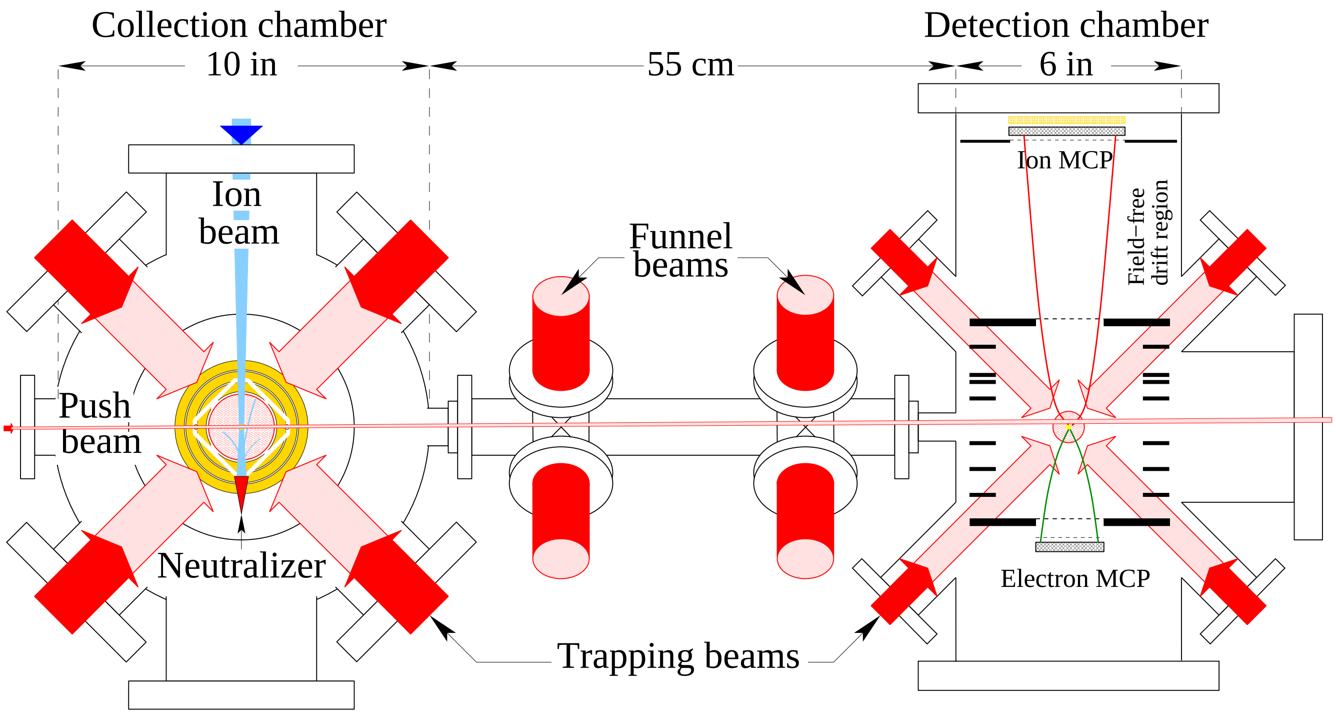

Figure 3.2: Schematics of the TRINAT double MOT, in the horizontal plane.

3.1.2 TRINAT Double MOT

The laser cooling and trapping of the radioactive Rb atoms is done by the TRINAT double MOT system [38], which was designed to reduce radioactive background and achieve UHV in the detection chamber. The schematic is shown in Figure 3.2. The double MOT system is made of three parts, a collection MOT, a transfer system and a detection MOT.

The radioactive Rb ions are provided by the Isotope Separator and Accelerator (ISAC) facility at TRIUMF, using the isotope separation on-line (ISOL) technique [39]. The ISOL system consists of a primary production beam, a target/ion source, a mass separator and beam transport system. The rare isotopes produced during the interaction of the 500 MeV proton beam with the target nucleus are stopped in the bulk of the target material, which is made of Nb and ZrC stacked foils and heated to 2000 °C. Those rare isotopes diffuse inside the target material matrix to the surface of the grain and then effuse to the ion source, where they are ionized to form an ion beam that can be separated by their mass to charge ratio and then guided to the experimental facilities. This system produces an enormous variety of isotopes and nuclear excited-state isomers at the very high rates needed for the experiments in the rest of this thesis.

Once the ion beam of radioactive Rb isotopes arrives at the TRINAT lab, it is firstly implanted in a Zirconium foil in the collection chamber. The Rb ions are mostly neutralized here because of the low work function of Zr [40]. Moreover, the Zr foil is heated to increase the Rb vapor density around the collection MOT in a dry-film coated cube. The collection MOT traps about 10^6 atoms in a 1 cm size cloud, with 10^{-3} collecting efficiency [38].

The transfer of the Rb atoms from the collection chamber to the detection chamber is done by lowering the first-trap laser intensity to about 10% of its value and applying a narrow blue-detuned push beam. This produces a 78(10)% transfer efficiency over a 75 cm distance. The push beam is aimed slightly above the detection MOT to miss it and to compensate the gravitational drop of the atoms during the transfer. There are also funnel beams working like a 2D MOT, to prevent the atomic beam from diverging in transverse directions.

In the detection chamber, the transferred Rb atoms are trapped again by a second MOT. The trap size is optimized to 1 mm size for Rb spectroscopy and recoiling momentum measurements. The UHV environment helps reduce the radioactive background, and results in a longer trap lifetime of about 15 seconds and higher trap population of about 10^6.

The 780 nm trapping light is from a Coherent 899 ring laser, locked at the Rb D2 transition by Doppler-free saturation spectroscopy. The output power of the 899 laser is split into two branches, which are sent to the collection MOT and detection MOT after AOM (accusto-optic modulator) frequency modulation. The trapping beams in the collection chamber have a diameter of 4.5 cm and the beam intensity is about 10 mW/cm^2, comparing to 50 mW/cm^2 and 2 cm diameter in the detection MOT. The 795nm repumping light is provided by diode lasers, locked at the Rb D1 transition. The diode lasers are in a master and slave configuration to produce enough repumping power for both MOTs.

The quadrupole magnetic field of the detection MOT is created by two identical coils in anti-Helmholtz configuration (coil geometries in Appendix B.2). Each coil has 32 turns with 50.5-Ampere current running through, resulting a magnetic field gradient of 0.5 Gauss/mm.

3.2 Photo-ionization

To measure the recoiling momenta of the neutral ^{86g}Rb decay daughters, we have to photoionize them first so that they can be collected by the electrostatic field and then guided into the detector. However, the daughter atoms fly with a recoiling momentum of 556 keV/c, which corresponds to a speed of 2 km/s and results in a Doppler frequency shift of 2.5 GHz at maximum. It's impossible for the laser frequency to be on resonance for each daughter atom in the case of one-photon transitions, and the photo-ionization rate will be greatly reduced.

As discussed in Section 2.2, the Doppler-free two-photon transition technique could cancel the first order Doppler frequency shifts by absorbing two counter-propagating photons with the same frequency. The properties of the Doppler-free two-photon transition technique make it a very good solution for photoionizing the decay daughters in this experiment. There are two advantages

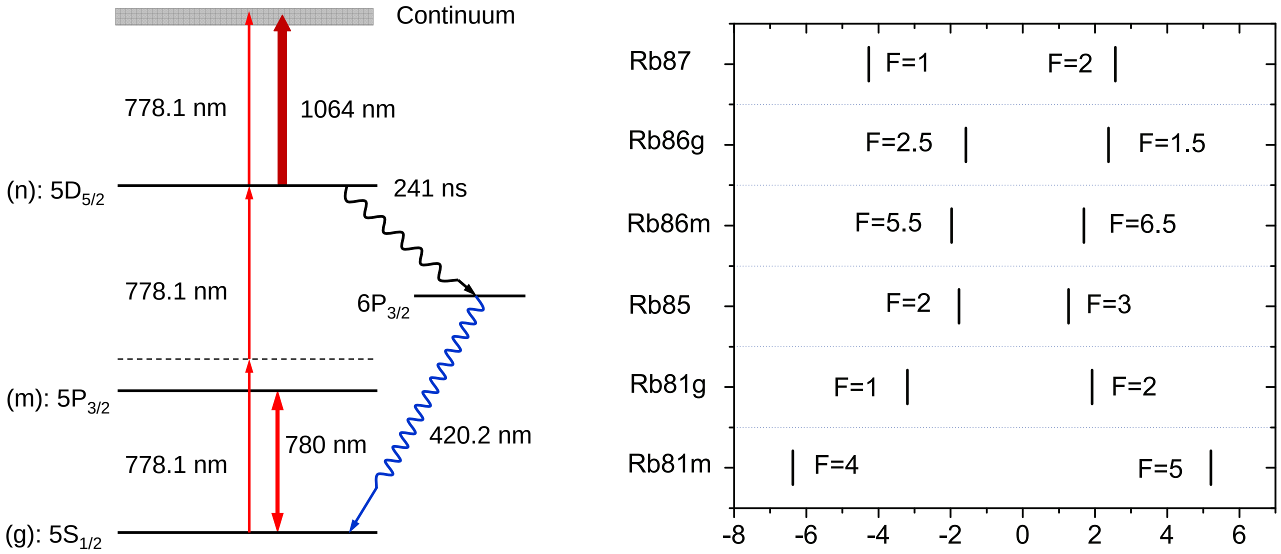

(a) photo-ionization scheme for Rb isotopes (b) $5S_{1/2}$ state hyperfine structures of Rb isotopes (GHz)

Figure 3.3: (a) photo-ionization scheme for Rb isotopes. (b) $5S_{1/2}$ state hyperfine structures of Rb isotopes. The needed hyperfine constants are from Ref. [30], the F number for each ground-state hyperfine level is also specified in the diagram.

to implement this technique. Firstly, the Doppler-free two-photon transition is independent of the atom's velocity in the first order approximation of the Doppler shift. Although the second order shift of $v^2/(2c^2)$ will not be canceled, it's only 60 kHz at maximum and can be neglected. Secondly, atoms flying in any direction with respect to the laser beam can be excited with the same probability, so there's no need to scan the laser frequency once it's locked on resonance with the transition frequency.

3.2.1 Photo-ionization Scheme

The photo-ionizing scheme is shown in Figure 3.3 (a), which can be divided into two steps. The first step is a Doppler-free two-photon transition, in which the atomic ground-state ^{86}Rb atoms simultaneously absorb two 778 nm photons from opposite directions and are excited to the $5D_{5/2}$ state. This two-photon transition is strongly enhanced by the near-resonance 780 nm D_2 transition.

The second step of the photoionization is from the $5D_{5/2}$ state to the continuum. The 778 nm laser could also drive this transition but its power is not good enough, so a second laser of 1064 nm is added to drive this transition more efficiently. In the meantime, the $5D_{5/2}$ state atoms could also decay back to the ground state by emitting 420nm fluorescence. Both the photoion signal and the 420nm fluorescence can be used to measure the $5D_{5/2}$ state hyperfine structure.

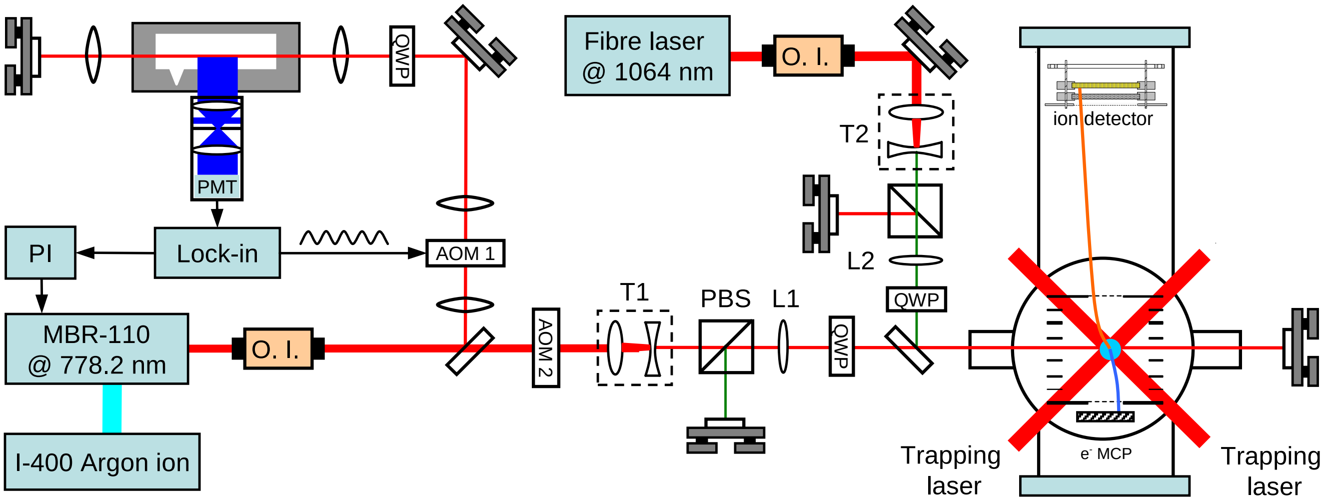

Figure 3.4: Optical setups for photoionizing the fast-moving ^{86g}Rb atoms. Acousto-optic modulators (AOM 1 and AOM 2) are used to compensate the offset of the two-photon transition resonance frequencies between the stable Rb isotopes in the vapor cell and the radioactive Rb isotopes in the trap. The beam divergence for both the 778 nm and 1064 nm light are controlled by telescopes (T1 and T2) and lenses (L1 and L2). Both laser beams are in multi-pass setups that are controlled by PBS (polarization beamsplitter) and QWP (quater waveplate). The laser feedbacks are blocked by O.I. (optical isolators) to improve the locking stability for the MBR laser, and to prevent the high 1064 nm light intensity from damaging the fibre laser.

3.2.2 $5S_{1/2}$ to $5D_{5/2}$ Two-Photon Transition Resonance

To drive the Doppler-free two-photon transition in radioactive Rb isotopes efficiently, the 778 nm light must be on resonance. However, the resonance frequencies of the $5S_{1/2}$ to $5D_{5/2}$ two-photon transition have never been measured for radioactive Rb isotopes, and the related isotope shift could be up to hundreds of MHz. Although the isotope shifts of the $5S_{1/2}$ to $5D_{5/2}$ transition could be estimated based on the isotope shift knowledge of the Rb D2 transition [30], the accuracy will not be good enough compared with the 0.66 MHz linewidth of the $5D_{5/2}$ state.

So the resonance frequencies of the $5S_{1/2}$ to $5D_{5/2}$ transition for radioactive Rb isotopes must be measured with high accuracy before the exotic particle searches, as well as the determination of the hyperfine structures for $5S_{1/2}$ and $5D_{5/2}$ states and the related isotope shifts in radioactive Rb isotopes. Details of the Doppler-free two-photon spectroscopy are shown in Chapter 6.

3.2.3 Photoionization Lasers

The optical setup for the exotic particle search experiment is shown in Figure 3.4, which includes a frequency-locking setup for the 778 nm light, and multi-pass setups for both the 778 nm and 1064 nm light to enhance the photoionization rate.

The 778 nm light driving the Doppler-free two-photon transition is from a Coherent MBR-110 Ti-Sapphire laser, which is pumped by a Coherent I-400 Argon ion laser. The linewidth of the MBR laser is 100 kHz, which is accurate enough to resolve the $5D_{5/2}$ state with a natural linewidth of 330 kHz (in two-photon scheme). The power output of the MBR-110 laser is about 0.6 Watts, and the beam is split into two parts by a beamsampler.

A small portion of the MBR laser power, $\sim$ 15 mW, is sent into a Rb vapor cell for locking the MBR laser frequency. Laser beams from both directions are focused and aligned to overlap with each other in the vapor cell. The focusing lenses have 20 cm focal length and the laser beam waist is $\sim 100\ \mu m$. The vapor cell was shielded by mu-metal to minimize the resonance frequency shifts caused by the Zeeman effect and was heated to 60 °C to increase the vapor density and the 420 nm fluorescence signal, which was collected and amplified by an ETL 9112B photo-multiplier tube. After amplification, the 420 nm fluorescence signal is sent to a phase-sensitive lockin amplifier and a PI (proportional-Integral) control box, to produce the error signal for locking the MBR laser to be on resonance with two-photon transitions in stable Rb species.

Most of the MBR laser power ($\sim$ 0.4 Watts) is sent to the UHV chamber, where the radioactive Rb isotopes are trapped in a magneto-optical trap (MOT). The trap cloud size is about 1 mm in diameter, and the 778 nm light is focused to overlap with the trap cloud to efficiently photoionize the trapped atoms. Photo-ions and photo-electrons are collected and accelerated by an electrostatic spectrometer so that they can be detected by micro-channel plates (MCPs). The photo-electron pulses are sent to a scaler counter and used for two-photon transition resonance searches.

The 1064 nm light is provided by a fibre laser, YLM-10-1064-LP from IPG Photonics, with 10 Watts maximum power output and 0.5 nm linewidth. To couple the 1064 nm light into the detection chamber and align with the trap cloud, a 45° mirror is used to combine the 778 nm and 1064 nm laser beams, which transmits the 778 nm laser power at 90% and reflect the 1064 nm laser power at more than 98.5%.

The photoionization laser beams are sent into the detection chamber through a vacuum viewport, which is 30° inclined above the horizontal plane and points towards the collection chamber. The optical setups for both lasers are built on a 30 mm cage system, including the telescope, polarization beamsplitters and waveplates, etc. This kind of setup made the alignment for the photoionization lasers much more difficult than in the horizontal plane. The reason is that the detection chamber has limited vacuum ports in the horizontal plane, which are used for the pushing beam and MOT beams, as shown in Figure 3.2.

3.2.4 Multi-pass Setup

According to our calculations (see section 3.6.1), the required power for the 1 mm size 778 nm light to saturate the two-photon transition would be 1.2 Watts. However, the MBR-110 laser can only provide 0.4 Watts at the trap location, due to the losses by the AOM modulation and optical controls. Similar problem also exists for the 1064 nm light.

To solve the power deficiency problem, we built a multi-pass setup for each laser, as shown in Figure 3.4. The light from both lasers is originally linearly polarized in the horizontal plane. By switching the laser polarizations with a quarter waveplate and the help of a PBS (polarization beamsplitter), both the 778 nm and the 1064 nm lights will pass through the trap cloud four times and the light intensities for both lasers will be quadrupled in the research chamber. In the meanwhile, the beam size of each pass at the trap location is adjusted to be around 1 mm by a telescope and a weak focusing lens, such as T1 and L1 for the 778 nm light, T2 and L2 for the 1064 nm light. The reason for the 1 mm laser beam size is from the momentum calibration, which requires that the fast-moving ^{86g}Rb photoions should be created within a 1 mm region around the trap center. Otherwise, the momentum resolution of the spectrometer will decrease dramatically (details will be discussed in Chapter 4).

The beam sizes for both lasers at the trap location were measured by the knife edge method, which was done by cutting the laser beam from one end to the other along the horizontal/vertical direction, and recording the transmitted power through the knife edge to deduce the beam sizes. Figure 3.5 shows the transmitted power measurements for the 778 nm light, including both horizontal and vertical directions for the first and third passes at the trap position.

To deduce the beam size W from the transmitted power P_T, we need a model to fit the data, which will be proven to be a complementary error function, erfc(x). The intensity for a Gaussian beam traveling along the z direction can be written as

$$I(x, y, z) = \frac{2P_0}{\pi W^2(z)}\, e^{-2(x^2+y^2)/W^2(z)}, \tag{3.1}$$

where P_0 is the total laser power, $(x^2+y^2) = r^2$ is the radial distance from the beam center, $W(z)$ is the $1/e^2$ beam radius at the position z and about 86.5% total laser power is inside the circle of $r = W(z)$. If the knife edge cuts through the laser beam along the x direction, the transmitted

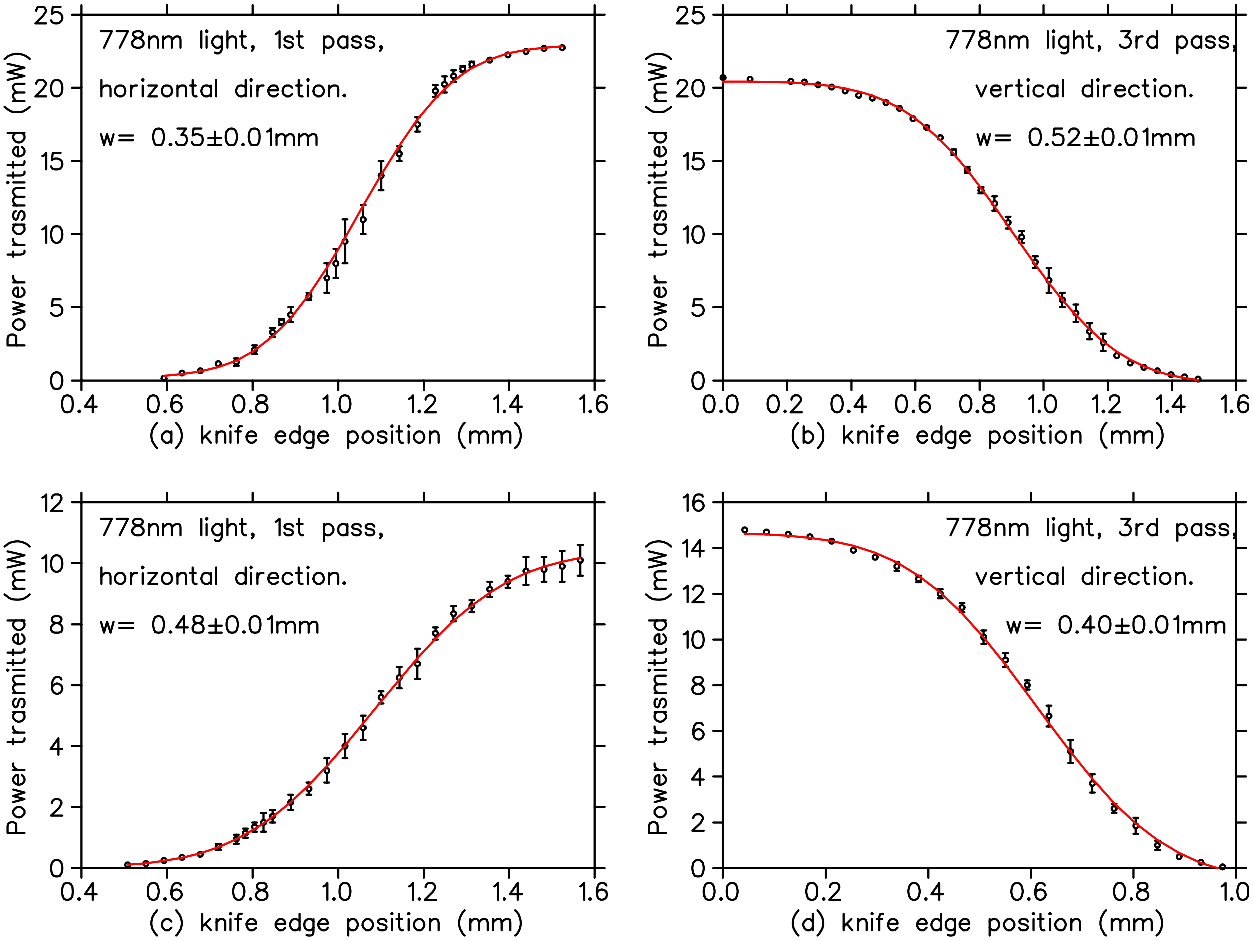

Figure 3.5: Beam profile measurement by a knife edge. (a) and (b) are the transmitted power P_T of the fist-pass 778 nm light, when the knife edge cut through the horizontal and vertical directions, respectively. (c) and (d) are the same case for the third pass.

power will be

$$\begin{aligned} P_T(z) &= \int_x^\infty \int_{y=-\infty}^\infty I(x,y,z)\,dxdy \\ &= \frac{2P_0}{\pi W^2(z)} \int_x^\infty e^{-2x^2/W^2(z)}dx \int_{-\infty}^\infty e^{-2y^2/W^2(z)}dy \\ &= \sqrt{\frac{2}{\pi}}\frac{P_0}{W(z)} \int_x^\infty e^{-2x^2/W^2(z)}dx \propto \mathrm{erfc}\left(\sqrt{2}\,x/W(z)\right), \end{aligned} \tag{3.2}$$

where $\mathrm{erfc}\big(\sqrt{2}\,x/W(z)\big)$ is a complementary error function.

As shown in Figure 3.5, the beam radius $W(z)$ is deduced by fitting P_T with a complementary error function, and the beam sizes are 0.7 – 1.0 mm and satisfy the 1 mm beam size requirement. We also performed the same beam profile measurement for the 1064 nm light, and the resulting

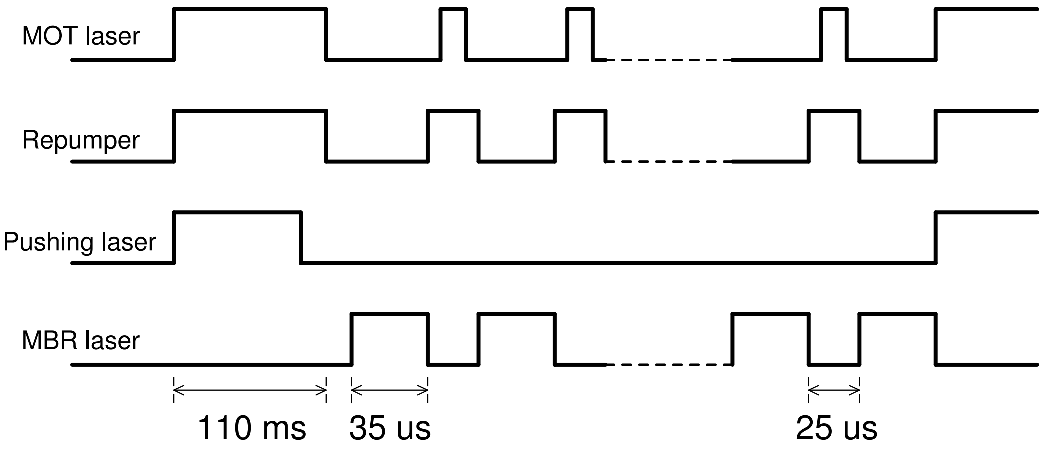

Figure 3.6: Duty cycle of the laser choppings, which are controlled by the AOM modulators.

beam sizes are 0.8 – 1.2 mm.

MBR laser frequency will be locked to a two-photon transition resonance of the cell species. By tuning the frequency modulation of AOM 1, we could scan MBR laser to search for two-photon resonances of the trapped species.

3.2.5 Duty Cycle

The duty cycle of the exotic particle search experiment is controlled by hardware using function generators. Figure 3.6 shows the scheme of the duty cycle, which can be divided into two parts, the trap-loading part and the photo-ionization part.

During the trap-loading part, the MBR laser is off and the blue-detuned pushing beam is turned on for 100ms to transfer Rb atoms from the first MOT into the UHV chamber, where the MOT laser and the repumper laser stay on to capture the transferred atoms to create the second MOT. The pushing beam is turned off 10ms earlier than the MOT laser and repumper laser to let the second MOT cool down.

As for the photo-ionization part, the MBR laser is chopped with a $35\mu s$ on and $25\mu s$ off cycle, while the repumper laser and the MOT laser are only on when the MBR is off. The chopping cycle removes potential AC Stark shifts of Doppler-free two-photon transitions by the MOT laser and repumper laser.

3.3 Electrostatic Spectrometer

Our spectrometer is designed to separate and collect all photoelectrons and photoions so that they can be detected by MCP detectors, regardless of the directions of the ^{86g}Rb recoiling momenta. More importantly, it's capable of three-dimensional focusing which minimizes the dependance of

	^{86g}Rb		^{81g}Rb	L (mm)
Electrodes	Uniform E	**Jeff4 248V**	Jeff4 47V	
A2	0	**0**	0	N.A.
B2	30	**6.8**	1.3	223.23(3)
CC2	51	**74.7**	14.1	209.77(20)
CC1	64	**80**	15.1	N.A.
C3	96	**84.4**	16.0	190.72(6)
C2	142	**107.7**	20.4	165.71(7)
C1	180	**92.2**	17.4	147.49(20)
B1	210	**248.4**	47.0	132.10(1)
A1	240	**142.5**	27.0	117.08(2)

Table 3.1: Biasing voltages on the spectrometer electrodes for the ^{86}Rb and ^{81}Rb experiments. L is the measured distance between each electrode and the flange center on the e^- detector side.

the momentum resolution on trap cloud size.

3.3.1 Three-dimensional Focusing

The trap cloud size largely limits the resolution of the recoiling momentum measurement. If two ions recoil have the same momentum but are located randomly in the trap cloud, they will arrive at the detector at different times and hit different positions. For a $\O = 1$ mm size trap, the maximum time difference is $\sim 0.5\ \mu s$ for the 556 keV/c momentum. The 1 mm spatial spread amounts to 2.5% uncertainty when projected onto the 40 mm radius ion MCP.

To achieve high momentum resolution, the spectrometer has to focus ions with the same recoiling momentum both in the longitudinal and transverse directions. Focusing in the longitudinal direction is also called time focusing, since it's a focusing in time. The transverse focusing is also called momentum focusing, since it's a focusing in space, and sorts recoiling ions into different trajectories according to their momentum. Details about time focusing and momentum focusing can be found in Section 4.1.1 and 4.1.2, respectively.

3.3.2 Spectrometer Geometry

The geometry of the spectrometer assembly is shown in Figure 3.7, which includes 9 electrodes, named as "A1, B1, C1, C2, C3, CC1, CC2, B2, A2". The electrode rings are made of aluminum, the relative distance between the neighboring electrodes are constrained by stainless-steel spacers, S1 – S9, which are all grounded. The empty spacing between the steel spacers and the electrodes is filled with ceramic spacers to insulate the biasing voltages for each electrode.

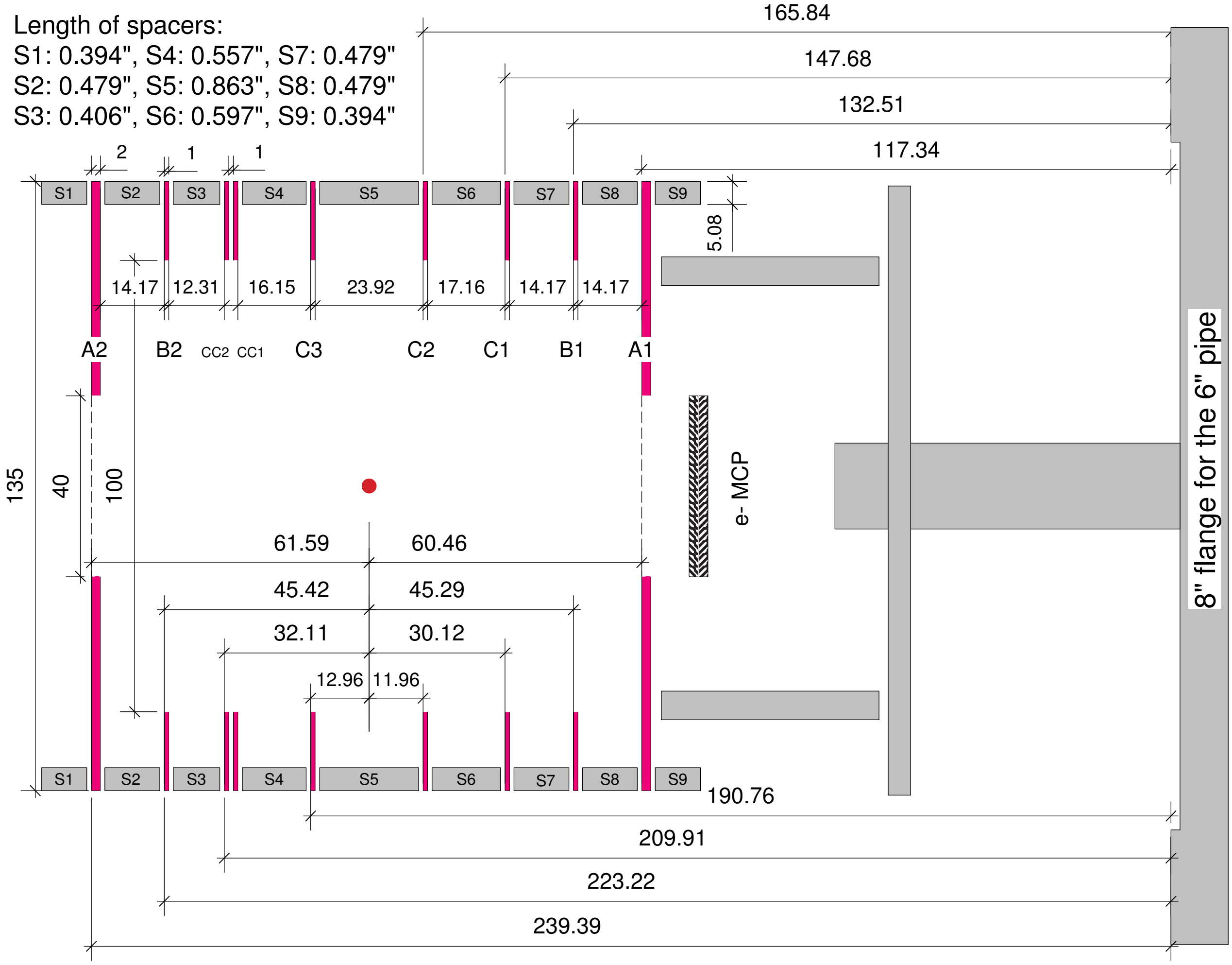

Figure 3.7: Geometry of the spectrometer assembly, all units in mm unless specified.

3.3.3 Resolution Optimization and Biasing Voltages

Our spectrometer is designed to include both time focusing and momentum focusing. To improve the momentum resolution in 3D and find the optimal biasing voltages for the electrodes, a numerical simulation was done by minimizing a customized χ^2 function,

$$\begin{aligned}\chi^2 &= \frac{1}{(0.04-|0.04-\max(r)|)^2}\sum_{i=1}^{N}\left[r_i - f_r(r_i,\vec{V})\right]^2 + \\ &\quad \frac{1}{(\max(t)-\min(t))^2}\sum_{i=1}^{N}\left[t_i - f_t(t_i,\vec{V})\right]^2.\end{aligned} \tag{3.3}$$

The χ^2 function measures the momentum resolution, including the radial part $\sum_{i=1}^{N}\left[r_i - f_r(r_i,\vec{V})\right]^2$ and the longitudinal part $\sum_{i=1}^{N}\left[t_i - f_t(t_i,\vec{V})\right]^2$. Details about the simulation can be found in J. Fung's TRINAT work report [41].

The optimal biasing voltages for the electrodes were determined by minimizing the χ^2 function, starting with a 1.2 Volts/mm uniform E-field, which gives maximum time focusing while also maximizing the use of the detector. The results are shown as the "Jeff4 248V" version in Table 3.1, which will be used to search for massive particles in the ^{86}Rb experiment. This set of potentials generates an electric field that focuses the spread of the recoils' radial displacements from an initial 1 mm down to about 220 μm. The time focusing of this field results in $\sim$ 10 ns timing spread for recoils with equal longitudinal momentum, and $\sim$ 3200 ns total timing spread for recoils with all possible longitudinal momenta between 0 and 556 keV/c.

Table 3.1 also summarized other versions of biasing voltages, such as the version of a uniform E-field for the ^{86}Rb experiment, and the version for the ^{81}Rb experiment which is scaled down from the "Jeff4 248V" version by a factor of $248.4/47 \simeq 6.1$.

3.4 Detector System

As shown in Figure 3.1, there are two detectors used in this experiment, an electron detector and an ion detector. The electron detector is made of two pieces of circular MCP plates in a chevron configuration, and biased to a voltage gradient of 1100 Volts/mm. The ion detector includes a MCP assembly and a delay-line anode, the ion MCP assembly has a Z-stack of three MCP plates, and is biased to 800 Volts/mm. The biasing voltage of each component is shown in Table 3.2.

	ion MCP plates			e$^-$ MCP plates			Delay-line anode		
	Front	Middle	Back	Front	Back	Anode	Signal	Refer.	Anode
Voltage	-2500	-1550	+350	+300	+2500	+2700	+650	+600	+575

Table 3.2: Biasing voltages on the MCP plates and the delay-line anode, DLD80.

3.4.1 Micro-channel Plates

A micro-channel plate is a planar detector used for detecting charged particles (electrons and ions), or radiations (ultraviolet radiation, X-rays and Gamma-rays). It provides high efficiencies and fast timing for anything producing secondary electrons at its surface.

The MCP plates used in this experiment are from Galileo. Each channel has a 12 μm diameter

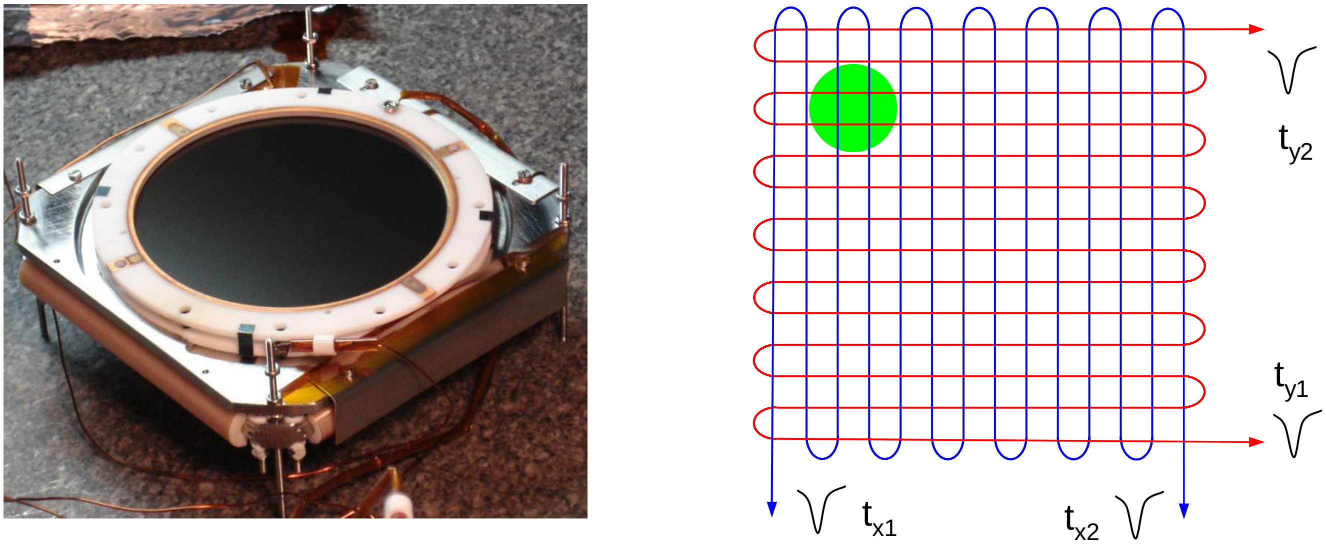

(a) MCP and DLD80 assembly

(b) working principle of DLD80

Figure 3.8: Micro Channel Plate and Delay-Line-Anode DLD-80.

and 11° angle. The active size after assembling is about 80 mm in diameter for the ion MCP, and 40 mm for the electron MCP.

Since the front MCP plate on the ion detector is biased at -2500 Volts, the impact energy of the Rb ions is above 2.5 keV. So the absolute detection efficiency for Rb ions is more than 60% [42], whereas the detection efficiency for the electron detector is about 50%.

3.4.2 Delay-line Anode

A commercial delay-line anode, DLD-80 from Roentdek, is chosen to measure the photoions' positions on the ion MCP, which is made of two pairs of signal and reference wires wound around an aluminum plate, the anode holder.

Figure 3.8(a) shows a picture of the ion MCP and delay-line anode assembly. The delay-line anode is mounted behind the back MCP plate with a 5 mm gap. The electron shower coming out of the back MCP plate will be accelerated to hit the delay-line anode, then trigger two electrical pulses traveling in opposite directions along the copper wires, as shown in Figure 3.8 (b). Since the traveling time for each pulse is proportional to its position on the wire, the difference of the traveling time between these two pulses is proportional to the ion's position relative to the center of the ion detector. A calibration shows that

$$x = (t_{x2} - t_{x1})/7.9, \tag{3.4}$$

$$y = (t_{y2} - t_{y1})/7.6, \tag{3.5}$$

where x and y are in mm and the time is in ns.

The reference wire is parallel and interlacing with the signal wire, and its biasing voltage is 50 volts less than the signal wire. The electron shower from the back MCP plate will be more attracted to hit the signal wire. The signals from the signal wire and reference wire are filtered by a transformer. If there's a signal that triggered both the signal and reference wires, it will not be detected as a real signal, since the subtraction between the signal wire and the reference wire cancels it.

3.4.3 Copper Mesh

As shown in Figure 3.1, three circular copper meshes were used in the system: a 40 mm diameter mesh in front of the e^- MCP detector, a 80 mm diameter mesh in front of the ion MCP detector, and another 40 mm diameter mesh at the left entrance of the field-free drift region. All three meshes have the same 80% transmission rate and share a common ground as the chamber wall.

The first two meshes provide a grounding reference for the high biasing voltages on the MCP detectors, and create uniform electrical fields for accelerating e^- and ions to a high enough energy so that they can fire the MCP detectors. Fluctuations on these meshes will deflect the trajectories of the charged particles during the acceleration, and change the hit positions on the detectors. This is particularly important for the ion side since the ion's displacement on the ion MCP is crucial for the transverse momentum reconstruction.

The third mesh separates the spectrometer field region from the field-free drift region and acts as an entrance window for ions to travel into the drift region. The shape of this mesh determines the local electric field on the spectrometer side, which is critical for the transverse momentum calibration, but less sensitive to the ion's TOF due to timing focusing capability of the spectrometer.

3.4.4 Mask Calibration

As discussed in Section 3.5.2, the width broadening for the DLD80 signals changes the rise time of the pulses and decreases the accuracy for constant fraction timing discrimination, eventually distorting the ions' positions on the detector. Besides, the non-uniformity of the electric field between the back MCP and the DLD80 also distorts the electrons' trajectories, so the ions' positions detected by the DLD80 will be different than their positions on the ion MCP.

This distortion problem was fixed by a mask calibration. The calibration mask is made of nickel by the lithography method with 2 μm accuracy. The geometry of the mask is shown in Figure 3.9 (a), which has 50 μm thickness and a cell structure with 1 mm wide barriers and 2 mm × 2 mm square holes. The mask calibration was done by projecting 5 MeV Alpha particles (from

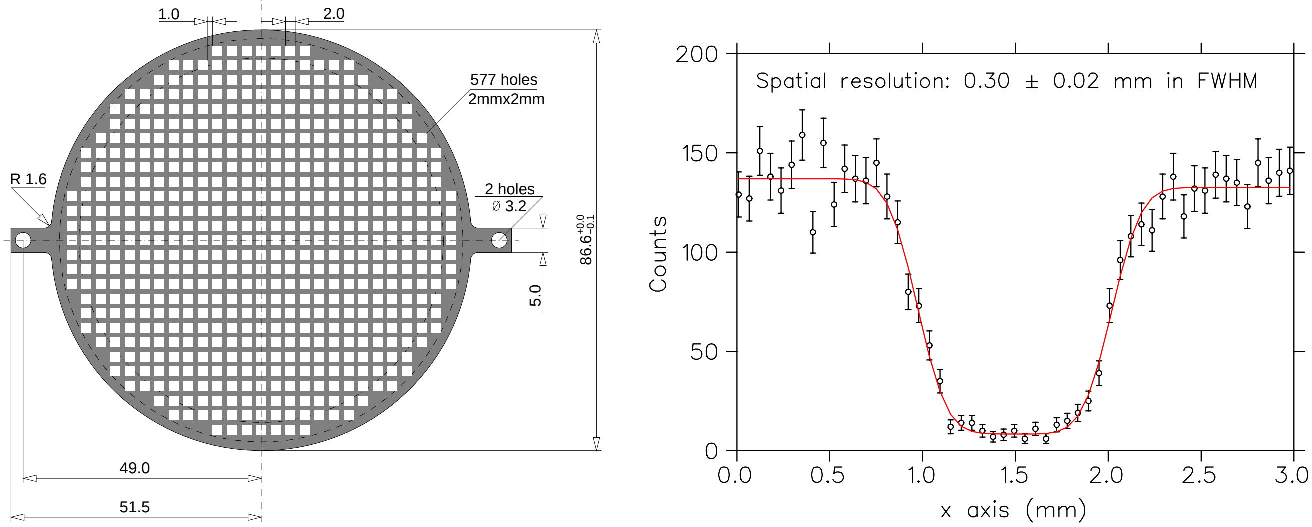

(a) geometry of the calibration mask, all units in mm.

(b) spatial resolution deduction.

Figure 3.9: (a) geometry of the calibration mask. (b) deducing the spatial resolution of DLD80, by fitting Equation 3.8 to one grid channel of the x projections of all events in Figure 3.10 (b).

an ^{241}Am source) onto the ion MCP, while the mask covered the front MCP surface. The recorded mask image is shown in Figure 3.10 (a), which is similar to the design but distorted. The white strips in the mask image are the region where the 50 μm thick nickel barrier blocked most of the Alpha particles.

To correct the mask distortion, a transformation matrix was created by finding the relationship between the distorted mask grids and the designed grids. For each grid point, the coefficients of the transformation A_X, B_X, C_X, D_X and A_Y, B_Y, C_Y, D_Y, was calculated by solving eight equations,

$$xx_i = A_X + B_X \cdot x_i + C_X \cdot y_i + D_X \cdot x_i \cdot y_i, \tag{3.6}$$

$$yy_i = A_Y + B_Y \cdot x_i + C_Y \cdot y_i + D_Y \cdot x_i \cdot y_i, \tag{3.7}$$

where $i = 1, 2, 3, 4$ and according to four corners of the grid, (xx_i, yy_i) and (x_i, y_i) are the coordinates of the flat grid and distorted grid, respectively. The transformation coefficients of all grids are then combined as a transformation matrix and will be used to calibrate the experimental data.

Figure 3.10 shows an example of the mask calibration, in which the mask distortion is corrected by applying the transformation. To estimate the spatial resolution of the detector, a customized function was fitted to one grid channel of the x projections of the mask image in Figure 3.10 (b), which is a combination of two complementary error functions,

$$\text{counts} = \frac{A_1}{2}\, erfc\left(\frac{x - (x_0 - \delta/2)}{\sqrt{2}\sigma}\right) + \frac{A_2}{2}\, erfc\left(\frac{(x_0 + \delta/2) - x}{\sqrt{2}\sigma}\right) + \text{BKG}. \tag{3.8}$$

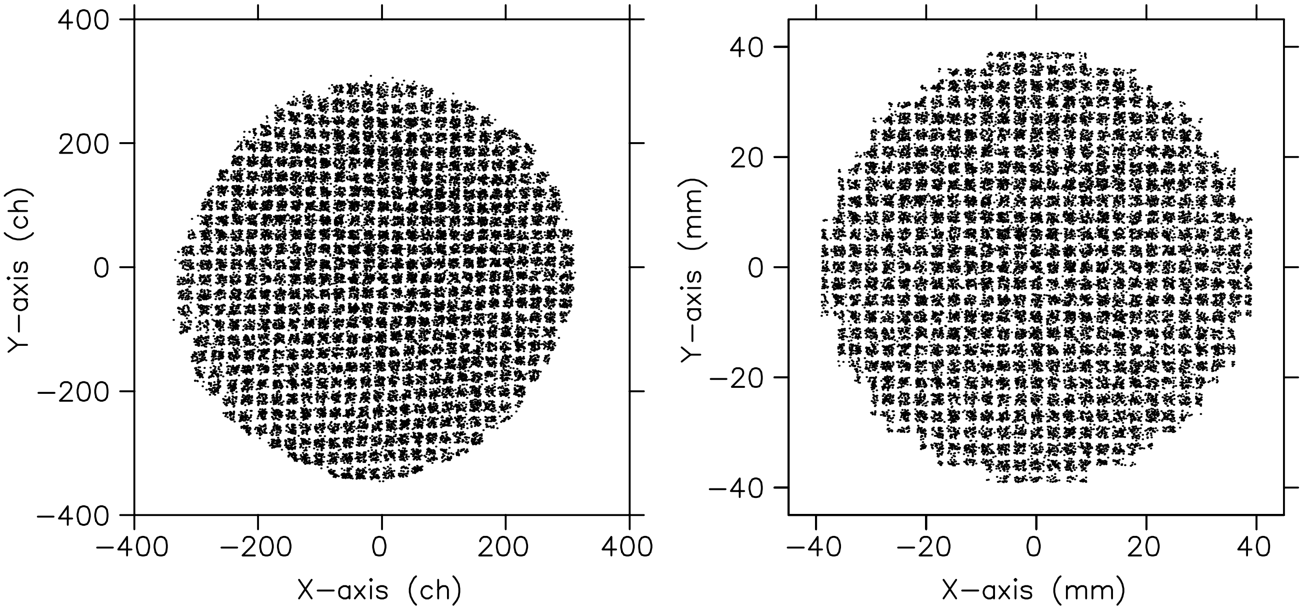

(a) MCP image before mask calibration

(b) MCP image after mask calibration

Figure 3.10: DLD-80 mask calibration. (a) MCP image before mask calibration, (b) MCP image after mask calibration.

The analytical expression of the complementary error function has been shown in Equation 3.2. As a convolution of the Gaussian and the step functions, the complementary error function models the shape of the measured edges: the deviation from an ideal edge is characterized by the Gaussian width σ, the positions of the edges are at $x_0 \pm \delta/2$. The fitting is shown in Figure 3.9 (b), which is centered at $x_0 = 1.5$ mm and covers the grids between 0 and 3 mm. The result shows that our spatial resolution of DLD80 is 0.3 – 0.4 mm. As a comparison, a French group reported 0.11(3) mm resolution [43]. However, the French group claimed the spatial resolution is constant over the whole detector surface and the reported resolution is for a localized position, while our resolution is a general resolution by summing one grid channel across the whole plate.

3.5 Nuclear DAQ

The nuclear data acquisition is done by a CAMAC system (Computer Automated Measurement And Control), controlled by a linux-based MIDAS application (Maximum Integration Data Acquisition System).

The electronics involved for the nuclear data acquisition include constant fraction discriminators, time-to-digital converter(TDC), NIM modules and digital delay generators.

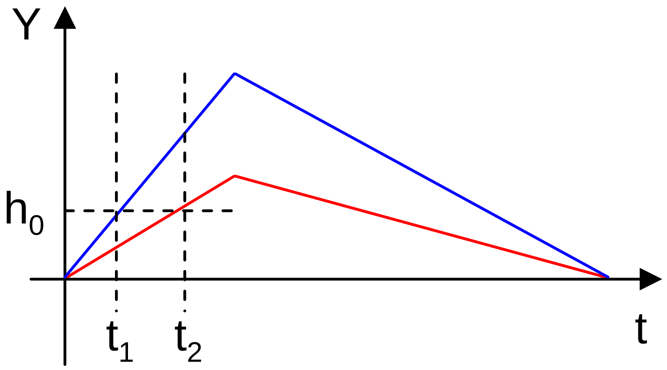

Figure 3.11: Simplified electrical pulses with the same rise time but different pulse heights.

3.5.1 Timing Coincidence

The signals from the MCP detectors and the delay-line anodes are firstly sent to the constant fraction discriminators, then converted to logic pulses in NIM modules which are used for triggering TDC.

The time of flight measurement of the ^{86}Rb ions is done by the TDC, which is started by the ion MCP signal, and stopped by the electron MCP signal. The electrons' TOF is just tens of ns and they arrive the detector much earlier than the ions, so the electron signals must be delayed to trigger the TDC later than the ions, and the delay time is slightly longer than Rb ions' TOF. This kind of hardware coincidence setup effectively improves the signal to noise ratio by distinguishing photoions from radioactive backgrounds.

3.5.2 Constant Fraction Discriminator

Constant fraction discriminator minimizes the time walk for pulses with different heights but similar rise time, such as the example shown in Figure 3.11. The pulses are simplified as lines for easier mathematical descriptions, thus the rising edge of the pulses can be written as $y = ht$, where h is the slope of the rising edge and also determines the height of the pulse, since both pulses have the same rise time.

Inside the constant fraction discriminator, the input signal is first split into two branches. One branch y_d is delayed by a time of t_d, and another branch y_{ia} is inverted and attenuated by a factor of f. y_d and y_{ia} could be written as

$$\begin{aligned} y_d &= h(t - t_d), \\ y_{ia} &= -hft. \end{aligned} \tag{3.9}$$

The output signal y' from the constant fraction discriminator is the sum of y_d and y_{ia},

$$y' = y_d + y_{ia} = h(t - t_d) - hft, \tag{3.10}$$

and the zero-crossing of y' is at time $t_0 = t_d/(1-f)$, which is independent of the signal slope/height. As a comparison, the leading edge discrimination produce a signal at the same height of the input pulses, which will cause time walking for signals with different height but same rise time, such as the difference of $|t_2 - t_1|$ in Figure 3.11.

Signals from the MCP detector and DLD80 are first sent to constant fraction discriminators, which will generate logic pulses for triggering the TDC at the same fraction of the pulse heights, when the rise time of the signals is constant. However, the DLD80 signals are from electrical pulses which traveled along a long wire. Those signals will be broadened during the traveling, and thus their rise time will depend on the travel time. For pulses starting with a large transverse displacement on the detector, the broadening difference between signals at both ends of the wire is a maximum. Thus the constant fraction discriminator will be triggered at quite different fraction of the pulse heights when the delay time t_d is fixed. The offset between the triggering level will cause global nonlinearity of the ions' positions on the detector, which is maximum for ions at the edge of the detector, as shown in Figure 3.10 (a).

3.6 Photoionization Rate Estimation

Based on the photoionization scheme and the experimental setups discussed in this chapter, we could estimate the photoionization rate for ^{86}Rb isotopes in the exotic-particle search experiment. There are several factors affecting the photoionization rate, such as the two-photon transition rate, the excitation efficiency by the 1064 nm light, and the MCP detecting efficiencies.

3.6.1 Two-photon Transition Rate by 778 nm Light

The $5S_{1/2}$ to $5D_{5/2}$ two-photon transition rate can be calculated by Equation 2.7, which is simplified to

$$R^{(2)}_{ng}(\omega = \omega_0) = \frac{4}{\Gamma}\left|\sum_m \frac{\mu_{nm}\mu_{mg}E^2}{\hbar^2(\omega_{mg} - \omega_0)}\right|^2, \tag{3.11}$$

When the 778 nm light is on resonance. Moreover, since the $5P_{3/2}$ state is much closer to the 778 nm resonance than all the other intermediate states, the summation can be reduced for the $5P_{3/2}$ state only. Then the two-photon transition rate will be further simplified to

$$R^{(2)}_{ng}(\omega = \omega_0) = \frac{4\mu_1^2\mu_2^2E^4}{\hbar^4\Gamma(\omega_1 - \omega_0)^2}, \tag{3.12}$$

where ω_1 is the angular frequency of the Rb D2 transition, $\mu_1 = 4.227\, ea_0$ [44] and $\mu_2 = 2.334\, ea_0$ [45] are the electric-dipole matrix elements for the D2 transition and the $5S_{1/2}$ to $5D_{5/2}$ transition, respectively.

In the detection chamber, the electric field by the 778 nm light from one direction is about 0.3 statvolts/cm in CGS unit, according to 0.4 Watts laser power in a 1 mm diameter beam. Using the above information, the two-photon transition rate is calculated to be 1 MHz. However, the experimental linewidth of the $5D_{5/2}$ state for ^{86}Rb isotopes is broadened to be twice the natural linewidth (will be discussed in Chapter 6), so the two-photon decay rate is reduced to 0.5 MHz.

Because the 778 nm light is in a four-pass setup, the two-photon transition rate will be doubled by absorbing $\sigma^+\sigma^+$ or $\sigma^-\sigma^-$ photons from opposite directions but not quadrupled, since absorbing two photons with opposite circular handedness doesn't increase the two-photon transition rate [46]. A more detailed explanation can be found in [36], which explained that there are two paths for absorbing two photons with opposite handedness but the same frequency. The probability amplitude of the $\sigma^+\sigma^-$ path is opposite to the $\sigma^-\sigma^+$ path. Therefore the total probability in this case is minimized and won't contribute to the two-photon transition rate.

In summary, the two-photon transition rate for the fast-moving decay daughter is about 1 MHz, which is 25% of the natural decay rate.

3.6.2 Excitation Efficiency by 1064 nm Light

According to the photo-ionization scheme, atoms in the $5D_{5/2}$ state will either decay back to the ground state, or get photoionized by the 1064 nm light. If we define the transition rate by the 1064 nm light as R_{1064}, the probability of getting photoionized from the $5D_{5/2}$ state is

$$\eta_{1064} = \frac{R_{1064}}{R_{1064} + 2\Gamma}, \tag{3.13}$$

where the decay rate is set as twice the natural decay rate, and $R_{1064} = \sigma \cdot \Phi$ is determined by the 1064 nm photon flux Φ and the ionization cross section σ. The total power for the 1 mm size 1064 nm light in the four-pass setup is 40 Watts, and the cross section is about 17.5 MBarn [47]. Then the probability of getting photoionized by the 1064 nm light is $\eta_{1064} \simeq 5\%$.

3.6.3 $^{86\mathrm{m}}$Rb Event Rate

There's no interaction time limitation for the trapped isomers, since they could see the photoionization light as long as the lasers are on. Although the 778 nm two-photon transition light is not on resonance for the trapped isomers, they are photoionized at a rate much higher than the fast-moving decay daughters.

The cycling transition for trapping the $^{86\mathrm{m}}$Rb isomers is a D2 transition between the $5\mathrm{S}_{1/2}$ state F = 13/2 sublevel and the $5\mathrm{P}_{3/2}$ state. So the $5\mathrm{S}_{1/2}$ to $5\mathrm{D}_{5/2}$ two photon transition by the 778 nm light also starts from the $5\mathrm{S}_{1/2}$ state F = 13/2 sublevel, since the $^{86\mathrm{m}}$Rb isomers are left in this state after the trapping laser is turned off (Details about the $5\mathrm{S}_{1/2}$ state hyperfine structure for Rb isotopes are shown in Figure 3.3 (b)). According to the law of angular momentum conservation, the $^{86\mathrm{m}}$Rb isomers in the $5\mathrm{S}_{1/2}$ F = 13/2 sublevel can only decay to the $5\mathrm{S}_{1/2}$ F = 5/2 sublevel in $^{86\mathrm{g}}$Rb, since the ^{86}Rb isomer decay is an $E4$ transition. So when the 778 nm light is locked to the two-photon transition between the $5\mathrm{S}_{1/2}$ F = 5/2 state to the $5\mathrm{D}_{5/2}$ state hyperfine sublevels in $^{86\mathrm{g}}$Rb, the laser frequency is about 1645 MHz off-resonance for the trapped $^{86\mathrm{m}}$Rb isomers (deduced by the two-photon spectra we measured in Chapter 6). In this case, the Lorentzian function of $\rho(\omega_{ng} - 2\omega)$ will not be on resonance, and

$$\rho(\omega_{ng} - 2\omega) = \frac{1}{\pi} \frac{\Gamma/2}{(4\pi \times 1645\mathrm{MHz})^2 + (\Gamma/2)^2}. \tag{3.14}$$

Thus the transition rate R_{778} for the isomers is 0.04 Hz. Moreover, the isomers could absorb 778 nm photons from the same direction since the Doppler frequency shift is negligible for them. This would increase their two-photon transition rate by 3×, so $R_{778} = 0.12$ Hz.

The expected isomer event rate is

$$R_m = \lambda_m N_m(t) = \lambda_m N_0 e^{-\lambda_0 t}, \tag{3.15}$$

where $N_m(t)$ is the number of the isomers at time t, λ_m is the isomer photoionization rate, λ_0 is the total decay rate of the isomers and

$$\lambda_0 = \lambda_m + 1/\tau_d. \tag{3.16}$$

The isomer photoionization rate

$$\lambda_m = R_{778} \cdot \eta_{1064} \cdot \eta_e \cdot \eta_{ion} \cdot \eta_{duty} \simeq 10^{-3}\ \mathrm{Hz}, \tag{3.17}$$

where $\eta_{duty} = 58\%$ is the time percentage of the 778 nm light in the duty cycle, and $\eta_e = 50\%$ and $\eta_{ion} = 60\%$ are detection efficiencies of the electron MCP and ion MCP, respectively. The total decay rate of the isomers λ_0 is dominated by the isomer decay rate $1/\tau_d = 0.013$ Hz, since the isomer decay lifetime $\tau_d = t_{1/2}/\ln 2 \simeq 87$ seconds, which is much longer than the photoionization part of the duty cycle.

For a typical trap population of $N_0 = 10^6$, the isomer event rate $R_m \simeq 1$ kHz.

3.6.4 ^{86g}Rb Event Rate

The ^{86g}Rb decay daughter recoils with a 556 keV/c momentum, which corresponds to a speed of 2 km/s. The typical interaction time τ_t between the fast-moving ^{86g}Rb recoils and the 0.5 mm radius photoionzation lasers is only about 0.25 μs. Although the atoms moving along the photoionization laser beam could interact with the light for a much longer time, the spectrometer is designed to work best for ions created within the 1 mm size trap, and the high-transverse-momenta ions created outside this region will not be focused enough to arrive at the ion MCP detector. In the exotic particle search experiment, the 778 nm light is on resonance with the fast-moving ^{86g}Rb atoms. So the two-photon transition rate for the ^{86g}Rb atoms is 1 MHz, and the probability of exciting them from the 5S$_{1/2}$ state to the 5D$_{5/2}$ state during the 0.25 μs interaction time is $\eta_{778} = R_{778}\ \tau_t = 25\%$.

The expected event rate for the decay daughters can be determined by

$$\begin{aligned} R_g &= (N_m(t)/\tau_d)\ \lambda_g \\ &\simeq N_0/\tau_d \cdot \eta_{778} \cdot \eta_{1064} \cdot \eta_e \cdot \eta_{ion} \cdot \eta_{duty}, \end{aligned} \tag{3.18}$$

where λ_g is the photoionization efficiency for ^{86g}Rb, and the number of trapped isomers $N_m(t) \simeq N_0$ during the photoionization. Since the typical trap population is $N_0 = 10^6$, the expected event rate for the ^{86g}Rb decay daughters is about 25 Hz, which is 40x less than the isomer event rate.

3.6.5 Event Rate Ratio

The absolute event rate could be affected by complex experimental factors. The most important factor is the two-photon transition rate, which critically depends on the alignment of the 778 nm beam. However, the optical components for the photoionization lasers are mounted on a 40 mm cage system which is at 30° inclined above the horizontal plane. Thus the beam stability is worse than the optical table mounting. Morerover, the alignment between the photoionization laser and the trap cloud could also be affected when the laser beams are unstable.

Although the experimental event rate could be much different from the expected one, the ratio between the isomer event rate and the daughter event rate will not be affected by the common factors, such as the laser power, $\eta_{1064}, \eta_e, \eta_{ion}, \eta_{duty}$, etc.

$$Ratio = \frac{R_m}{R_g} = \frac{\lambda_m N_m(t)}{\lambda_g N_m(t)/\tau_d} = \frac{\tau_d R^i_{778}}{\tau_t R^d_{778}} = \frac{\tau_d}{\tau_t} \cdot \frac{(\Gamma/2)^2}{(\Delta\omega)^2 + (\Gamma/2)^2}, \tag{3.19}$$

where the superscript i represents isomer, d represents decay daughter, $\Delta\omega = 2\pi \times 1645$ MHz, and $\Gamma = 2\Gamma_0$ (the natural decay rate of the 5D$_{5/2}$ state). If we assume the dipole transition matrix elements are the same for both Rb isotopes, this ratio is about 40. It is also consistent with the ratio between the calculated absolute event rates (as shown in Section 3.6.4). The achieved rates in the exotic particle search experiment will be discussed in Section 5.9.2.

Chapter 4

Time-of-Flight Simulations

In this chapter I will summarize the Time-of-Flight simulations using SIMION, which will be used for momentum calibrations and reconstructions in the Rb86 experiment.

Firstly I will explain the TOF theory involved in this experiment, which includes two important features, time focusing and momentum focusing. Then I will discuss the trajectory deflection by magnetic fields, and the way to correct it. After correcting the magnetic field deflection, I will show the results of momentum calibrations for +1 and +4 ^{86}Rb ions, using flat copper meshes and the designed geometries for the spectrometer and the detectors. At the end of this chapter, I will summarize the momentum resolution we could expect.

4.1 Time-of-Flight Theory

Time-of-flight technique has been widely used in mass spectroscopy. By combining it with the recently developed laser cooling and trapping technique, a new method with the name of COLTRIMS (Cold Target Recoil Ion Momentum Spectroscopy) was invented to make the momentum measurement possible [1, 2]. This technique is also crucial for our exotic particle search experiment.

Besides the basic idea that the flight time is inversely proportional to the mass of the particle, there are more interesting features that could be realized with the TOF technique, such as time focusing and momentum focusing.

4.1.1 Time Focusing

The idea of time focusing is to build a one-one linear mapping between the ions' TOF and their longitudinal momenta, regardless of their initial positions. Ions in a position further away from the field-free drift region will spend more time in the acceleration region. However, they also see a bigger voltage drop and will reach the field-free drift region at a higher speed than those starting closer to the drift region. Then the less time spent by the far ions in the field-free drift region will

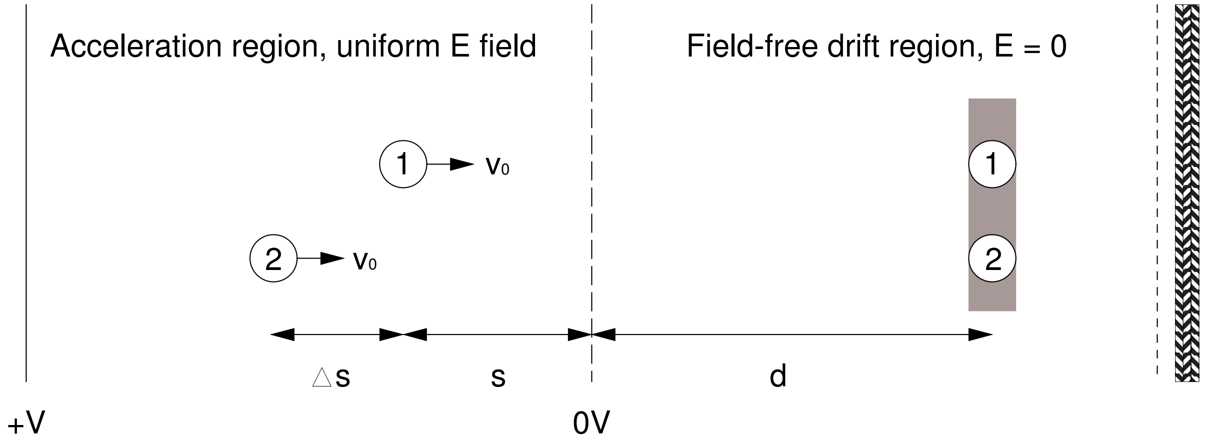

Figure 4.1: The principle of time focusing, for a spectrometer with uniform electric field. Both ion 1 and ion 2 have a $+q$ charge and mass m, and the initial velocities are v_0 along the time-of-flight axis.

compensate the extra time it spent in the acceleration region, and arrive the detector at the same time as the closer ions.

Figure 4.1 shows the principle of time focusing for a spectrometer with a uniform electric field. Detailed discussion and kinematics can be found in Cotter's book [48]. Ion 1 and ion 2 start the flying from different locations in the acceleration region, s and $s + \Delta s$, respectively. Each has a charge of $+q$ and mass m, thus the same acceleration, $a = Eq/m$. If the ions have a initial velocity of v_0, then the time spent in the acceleration region is

$$t_{1s} = \frac{-v_0 + \sqrt{v_0^2 + 2as}}{a} \text{ and } t_{2s} = \frac{-v_0 + \sqrt{v_0^2 + 2a(s + \Delta s)}}{a}, \tag{4.1}$$

and the time spent in the drift region for a distance of d is

$$t_{1d} = \frac{d}{\sqrt{v_0^2 + 2as}} \text{ and } t_{2d} = \frac{d}{\sqrt{v_0^2 + 2a(s + \Delta s)}}, \tag{4.2}$$

where the subscript 1 and 2 means ion 1 and ion 2, respectively.

If we define the TOF difference between ion 1 and ion 2 in the acceleration region as Δt_s, and the difference in the field-free drift region as Δt_d, then

$$\begin{aligned}\Delta t_s = t_{1s} - t_{2s} &= \frac{\sqrt{v_0^2 + 2as}}{a} - \frac{\sqrt{v_0^2 + 2a(s+\Delta s)}}{a} \\ &= \frac{\sqrt{v_0^2 + 2as}}{a} - \left(\frac{\sqrt{v_0^2 + 2as}}{a} + \frac{\Delta s}{\sqrt{v_0^2 + 2as}} + ... \right) \\ &\simeq \frac{-\Delta s}{\sqrt{v_0^2 + 2as}} \end{aligned} \tag{4.3}$$

$$\begin{aligned}\Delta t_d = t_{2d} - t_{1d} &= \frac{d}{\sqrt{v_0^2 + 2a(s+\Delta s)}} - \frac{d}{\sqrt{v_0^2 + 2as}} \\ &= \left(\frac{d}{\sqrt{v_0^2 + 2as}} - \frac{da\Delta s}{(v_0^2 + 2as)^{3/2}} + ... \right) - \frac{d}{\sqrt{v_0^2 + 2as}} \\ &\simeq \frac{-da\Delta s}{(v_0^2 + 2as)\sqrt{v_0^2 + 2as}}, \end{aligned} \tag{4.4}$$

where the expansion including the $(s + \Delta s)$ term is about the point $\Delta s = 0$ and treats s as a constant.

Time focusing requires that ion 1 and ion 2 reach position d at the same time, which means the total flight time of ion 1 equals that of ion 2, $t_{1s} + t_{1d} = t_{2s} + t_{2d}$, or $\Delta t_s = \Delta t_d$. If the initial velocities are 0, the condition of time focusing for a uniform electric field is $d = 2s$ (with $\Delta s \ll s$), and this condition is still true for non-0 initial velocities as long as $v_0 \ll \sqrt{2as}$.

The trapped $^{86\mathrm{m}}$Rb atoms decay into $^{86\mathrm{g}}$Rb atoms, with a recoiling speed of about 2 km/s. If two $^{86\mathrm{g}}$Rb ions fly in an E-field free region, starting with the same longitudinal components but separated by 0.42 mm longitudinally, the minimum TOF difference between them will be 200 ns when their recoiling momenta are both along the TOF axis. In contrast, the time-focusing capability of our spectrometer reduces this difference to 1.6(1) ns in σ, as shown in Figure 4.2. The simulation assumes that all the $^{86\mathrm{g}}$Rb ions have the same 556 keV/c longitudinal momentum and are distributed in a 0.42 mm FWHM cloud with a 3D Gaussian profile.

4.1.2 Momentum Focusing

The main idea of momentum focusing is to sort ions with the same initial momentum into the same trajectories and hit the same position on the detector, thus minimizing the spatial spreads caused by the trap cloud size and providing a one-to-one linear relationship between ions' transverse displacements and their initial transverse momenta.

In our design, the momentum focusing capability for the spectrometer is achieved by an electrostatic lens, which is made of two electrodes "CC1" and "CC2" with a 2 mm separation. The

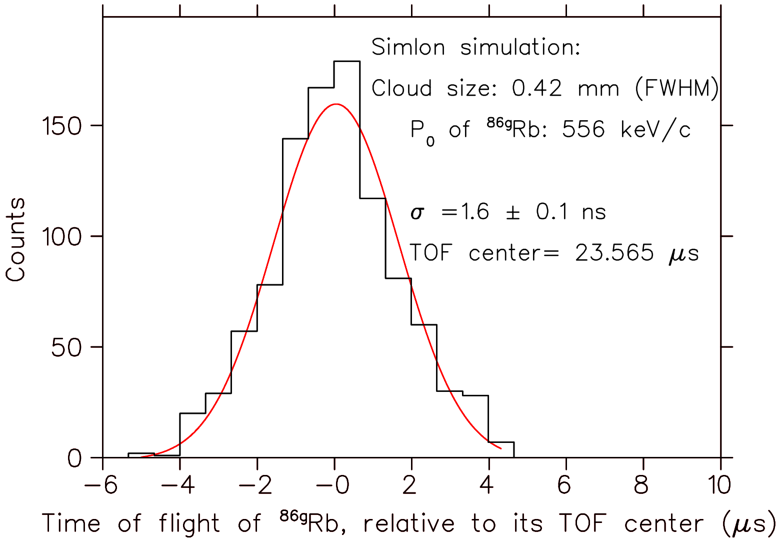

Figure 4.2: TOF spectrum of ^{86}Rb ions by SimIon simulations, with 556 keV/c initial momenta along the longitudinal direction (TOF axis).

resulting optical-lens-like E-field can be seen in the contour line simulation by SimIon, as shown in Figure 4.3. The simulation also includes the trajectories of three groups of ions. Each group starts with the same momentum but distributed in a 1 mm FWHM cloud with a 3D Gaussian profile. The trajectories qualitatively showed the focusing effect of the electrostatic lens, since the width decreases as the ions flying away from the trap center, and the ion MCP position is optimized at the width minimum region.

Different trap cloud sizes were also investigated to test the limits of the momentum focusing function. As shown in Figure 4.4 (a), the ions' spatial spreads on the MCP are evaluated for different sizes of the trap and different recoiling momentum along the x direction, including trap sizes of 0.4 mm, 0.5 mm and 0.6 mm in σ. The average size of the MCP spread is quite constant when the recoiling momentum is less than 400 keV/c, but increases for higher recoiling momentum, and the size for the 556 keV/c recoils is almost twice the size for low momentum recoils. As an example, the MCP image size is more than 0.4 mm in σ for the 556 keV/c recoils from a $\sigma = 0.6$ mm trap, which is worse than the spatial resolution of our delay-line anode.

So the momentum focusing function of our spectrometer works well for trap size up to 1 mm in FWHM, while bigger trap size will hurt the momentum resolution of the 556 keV/c recoils. The spatial spreads were also converted into momentum resolution by $\sigma \times P_{recoil}/r_{disp.}$, as shown in Figure 4.4 (b). We also checked the effect of momentum focusing in y direction, which showed similar results as in x direction.

In summary, the momentum focusing capability of our spectrometer focuses the ions' radial spread by a factor of 2.5 when the recoiling momentum is less than 500 keV/c, but the focusing

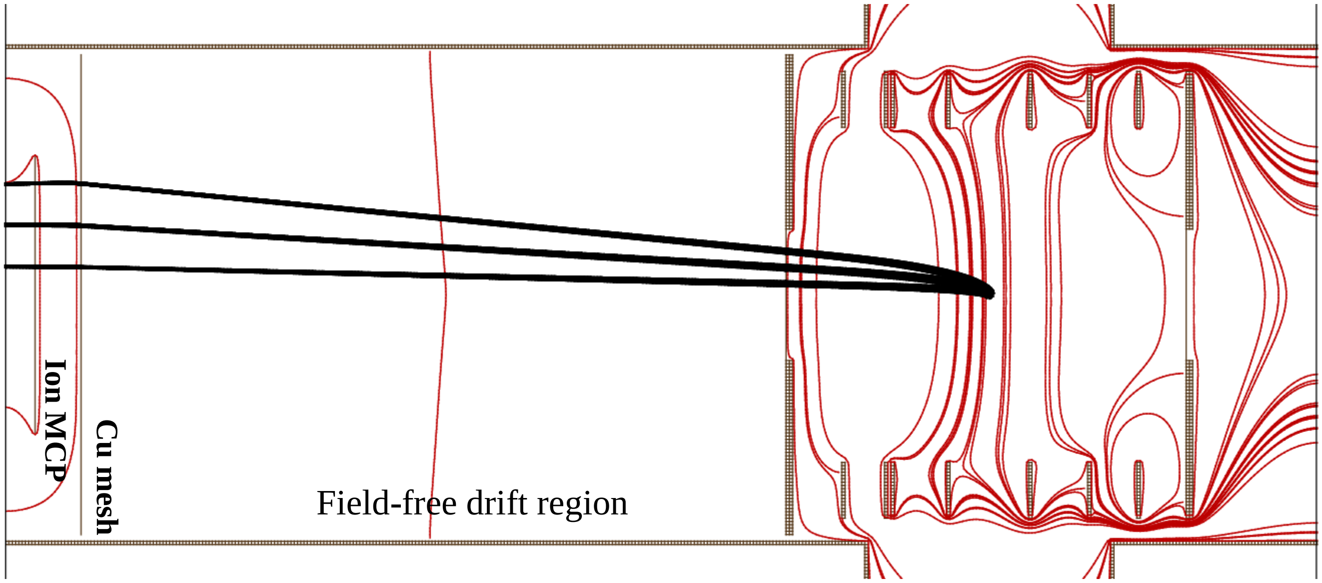

Figure 4.3: Principle of momentum focusing. The black lines are trajectories of 3 groups of photoions with different transverse momentum, 100 keV/c, 250 keV/c and 400 keV/c. Each group includes about 300 ions with initial positions distributed in a 1 mm FWHM cloud. The group linewidth gets smaller as the trajectories converge.

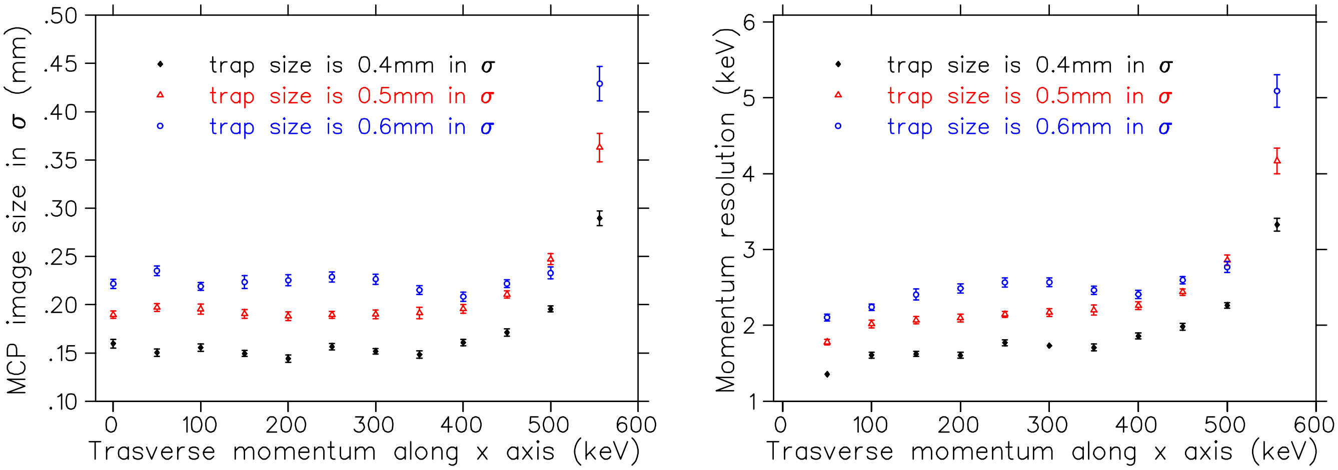

Figure 4.4: Investigation of the momentum focusing capability by SimIon simulations. (a) spatial spread on the MCP detector, for ions with different transverse momentum. (b) Momentum resolution converted from the spatial spread by $\sigma \times P_{recoil}/r_{disp.}$.

gets worse for the 556 keV/c recoils. The resulting uncertainty in momentum resolution is 2 – 3 keV/c for 1 mm FWHM trap size.

4.1.3 Maximum Transverse Displacement

If we define the recoiling speed of the ^{86}Rb ions as $v_0 = \sqrt{v_L^2 + v_r^2}$, where v_L and v_r are the longitudinal and transverse components, respectively, then the transverse displacement r when the ions leave the acceleration region s is

$$r = v_r \times t_s = \sqrt{v_0^2 - v_L^2} \times \frac{-v_L + \sqrt{v_L^2 + 2as}}{a}. \tag{4.5}$$

To find out the longitudinal velocity that corresponds to a maximum displacement, we need to take a time derivative of r, and

$$\frac{dr}{dt} = 0 \Rightarrow v_L = \pm \frac{v_0^2}{\sqrt{2as + 2v_0^2}} = \pm \frac{v_0}{\sqrt{1 + E_k/E_0}}, \tag{4.6}$$

where E_0 is the ion's initial kinetic energy, and $E_k = E_0 + mas$ is the ion's kinetic energy after E-field acceleration. Equation 4.6 verifies that the maximum displacement of the ions on the detector does not correspond to a 0 longitudinal velocity component.

In our experimental setup, the recoiling kinetic energy for ^{86g}Rb is $E_0 \simeq 1.9$ eV, and the kinetic energy after acceleration is $E_K \simeq 86$ eV. So the longitudinal velocity component that results in a maximum transverse displacement should be around $0.15 v_0$ but could be slightly different, since the E-field of our spectrometer is not totally uniform.

4.2 Trajectory Deflection by The Magnetic Field

There are three main sources of magnetic field involved in this experiment, the Earth's magnetic field, 3 pairs of Helmholtz coils, and the quadrupole magnetic field from the MOT.

The Earth's magnetic field is about 0.5 Gauss and across the whole chamber, and it is canceled around the trap region by three pairs of Helmholtz coils from three directions. The field sum of these two fields have little effect on deflecting the ions' trajectories, compared to the quadrupole magnetic field. The quadrupole magnetic field is only 0.3 Gauss/mm at the trap position, but increases to tens of Gauss as the photo-ions fly away from the trap center, as shown in Figure 4.5 (a).

Ions with only longitudinal momentum components will not be deflected by the quadrupole magnetic field, since their traveling direction is along the z axis which is always parallel to the $\vec{B}$ field. However, ions with transverse momentum components will be deflected by the quadrupole B field, and their final positions could be shifted up to 3 mm, in a direction orthogonal to their initial transverse momentum. Figure 4.5 (b) shows the SimIon simulations of the deflection effect, for +1 ions with transverse momentum along the x axis (horizontal direction), the deflection is in

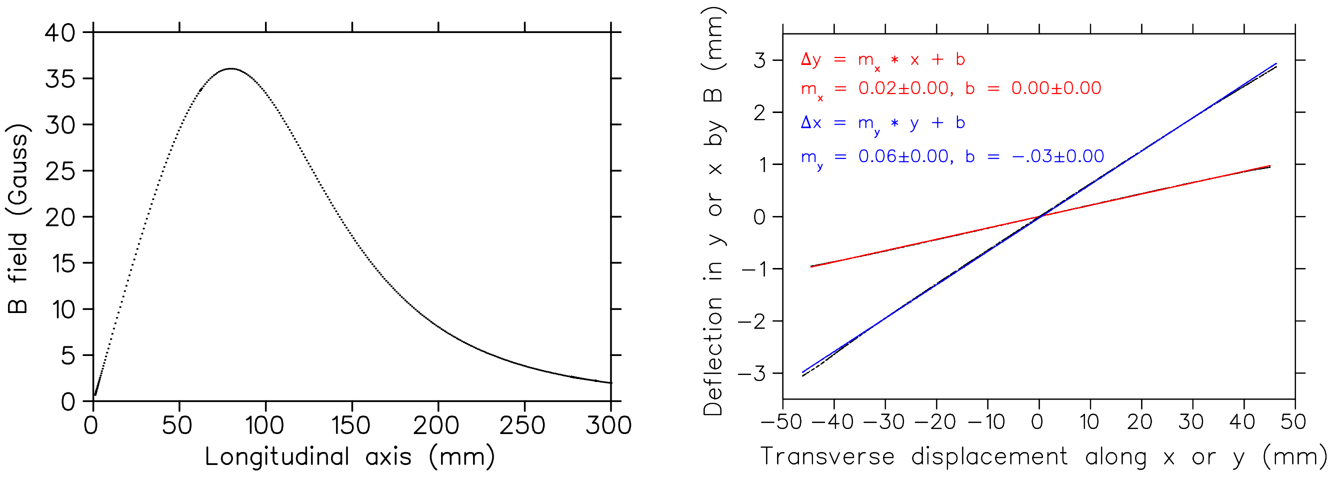

(a) B field along the longitudinal axis.

(b) Deflection of ions' positions by B field

Figure 4.5: SimIon simulations of the quadrupole magnetic field. (a) magnitude of the quadrupole magnetic field along the longitudinal axis. (b) deflection by the quadrupole magnetic field. +1 ^{86}Rb ions started with momentum along the x or y direction, the deflection is along the orthogonal transverse axis and increases linearly with the transverse displacement.

the vertical direction and $\Delta y = 0.02x$, which is about 2% of the x transverse displacement. On the other hand, $\Delta x = 0.06y - 0.03$ mm; the deflection in the horizontal direction is three times of the vertical direction.

4.2.1 MCP 2D Image Distortions

The directions and sizes of Δx and Δy could explain the distortion pattern we observed, both in SimIon simulations and in the experimental data. As shown in Figure 5.13 and 5.16, the MCP 2D images is distorted to an elliptical shape with the major axis at around 60°, which should be circular when B field is off. Since $\Delta x = 3\Delta y$, the distortion along the x direction is much worse than along the y direction. In the half plane of $y > 0$, Δx is positive and ions are shifted to the $+x$ direction, wherever, in the $y < 0$ region, all ions are shifted to the $-x$ direction.

4.2.2 Corrections

It might seem that the quadrupole B field deflection wouldn't affect the momentum calibration much, if using the total radial displacement instead of calibrating the x and y components separately. For ions starting along the vertical direction, the total radial displacement after deflection is

$$r' = \sqrt{y^2 + \Delta x^2} = \sqrt{y^2 + (0.06y)^2} = 1.002y, \tag{4.7}$$

so the radial displacement only changes by 0.2% at maximum, which is negligible compared to the contribution from the 0.3 – 0.4 mm spatial resolution. However, the momentum focusing effect gets worse with increasing transverse momentum, and the spatial spread of the ions with the same transverse momentum will be affected greatly by the B field deflection. So it is necessary to correct the B field deflections, especially for ions with higher transverse momentum.

The easiest way to correct the deflections by the quadrupole B field is to include the correlation between the ions' x and y coordinates when calibrating the transverse momentum components. Equation 4.8 has been selected to calibrate $P_x^{'}$ and $P_y^{'}$,

$$\begin{aligned} P_x^{'} &= a_x\, x^3 + b_x\, x^2 + c_x\, x + m_y y + d_x \\ P_y^{'} &= a_y\, y^3 + b_y\, y^2 + c_y\, y + m_x x + d_y \end{aligned} \tag{4.8}$$

which includes the correlations of $\Delta x \sim m_y y$ and $\Delta y \sim m_x x$, and also a third order polynomial for the non-correlation part.

4.3 Momentum Calibrations with A Flat Spectrometer Mesh

4.3.1 Time-of-flight Simulation by SimIon

The momentum calibration requires to find the relationships between ions' initial recoiling momentum and measurable variables, such as the TOF, and the transverse displacements on the detector. Those relationships were determined by TOF simulations using SimIon 8, a 3D ion optics simulation program that calculates the electric fields for the electrodes and ion trajectories in those fields.

In SimIon simulations, the experimental setups for the TOF simulation are created by a GEM code, as shown in Appendix B.1, which includes the vacuum chamber, the electrodes of the spectrometer, the MCP detector and flat copper meshes, etc. The related geometries and dimensions can be found in Figure 3.1 and Figure 3.7, and the biasing voltages for the electrodes can be found in Table 3.1.

Besides the electric field, SimIon also calculates the quadrupole magnetic field of the MOT, which is created by a LUA user program in the simulation, as shown in Appendix B.2. The Earth's B field was ignored since it was compensated by three pairs of Helmholtz coils.

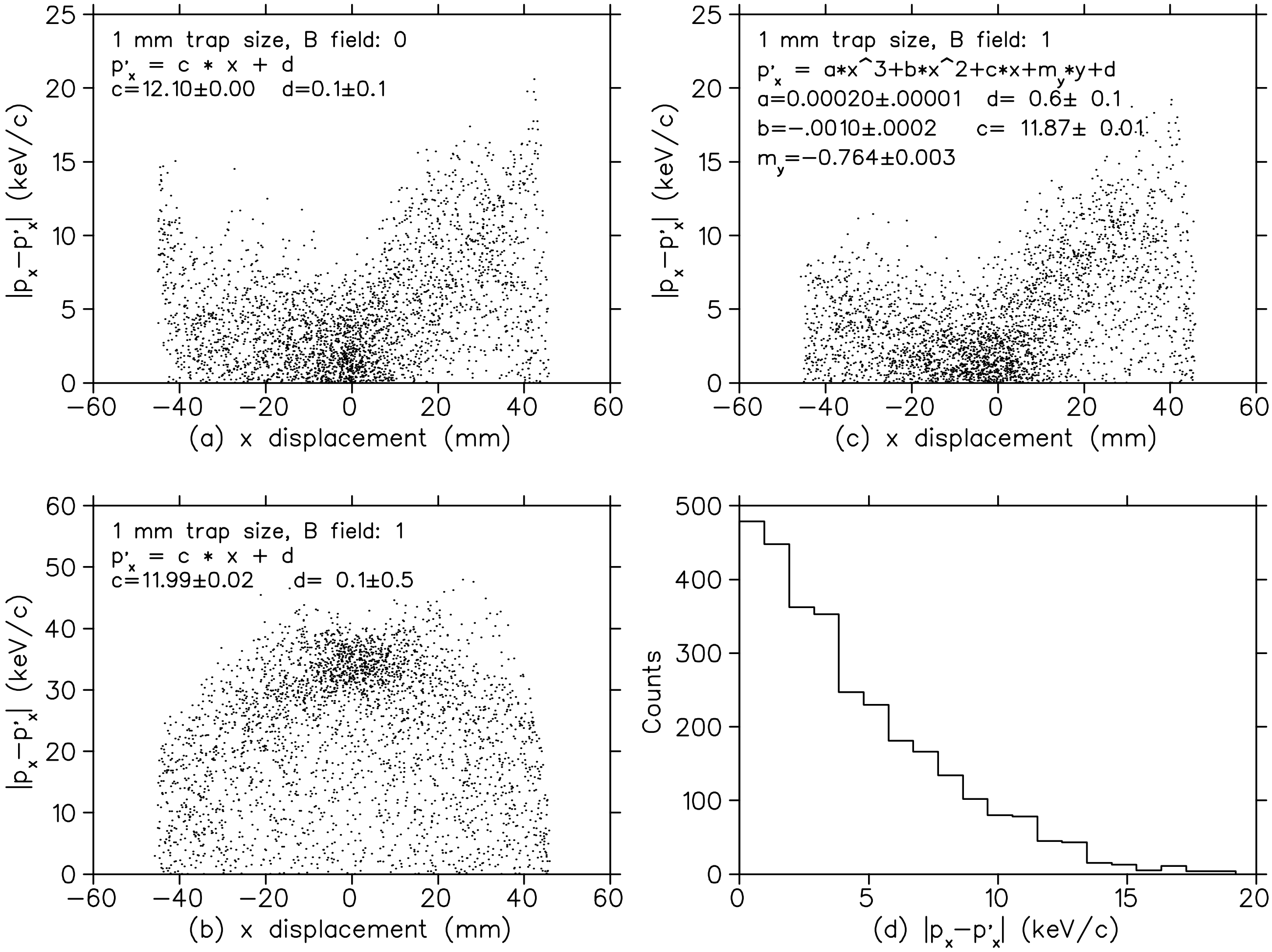

Figure 4.6: Momentum calibrations of the x component for ions with +1 charge and starting in a 1 mm FWHM size trap, when the 40 mm spectrometer mesh is flat. P_x is the preset momentum component in the simulation, P_x' is the calibrated value according to different calibration equations. (a) linear calibrations when B field is off. (b) linear calibrations when B field is on. (c) calibrations using Equation 4.8 with B field on. (d) histogram of the $|P_x - P_x'|$ residual, after calibrating with Equation 4.8.

4.3.2 ^{86}Rb Ions with Charge +1

The calibrations are divided into two parts, the longitudinal component along the z axis, and the transverse components along the x and y axes. To find the relationships between the initial momentum components and measurable variables, the +1 ^{86}Rb ions are simulated in SimIon with a 556 keV/c recoiling momentum, the directions are evenly distributed in azimuthal and elevation angles, and the starting positions are distributed in a 1 mm FWHM cloud by a 3D Gaussian profile.

The relationship between the longitudinal momentum P_t and TOF t is quite linear and not

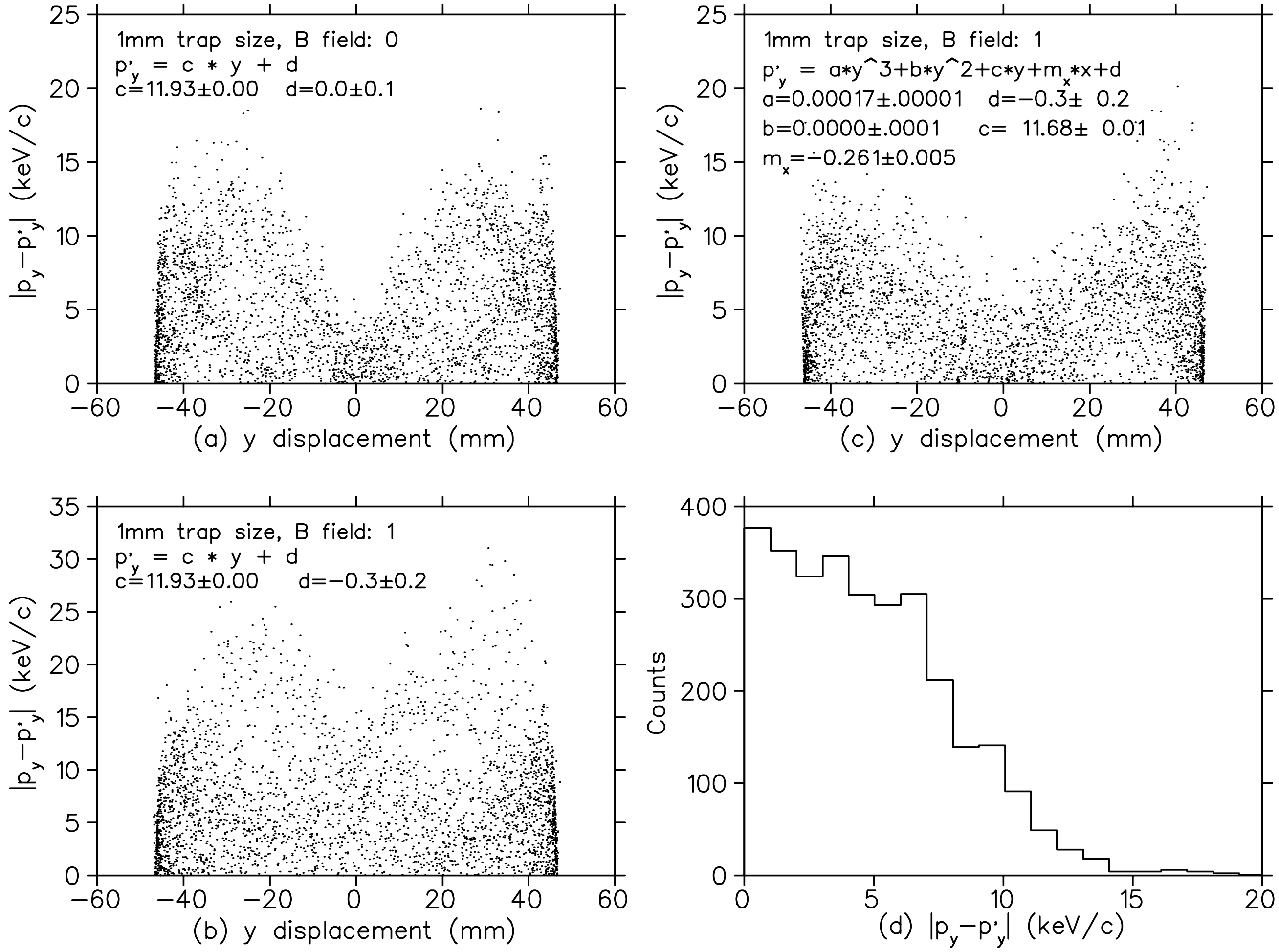

Figure 4.7: Momentum calibrations of the y component for ions with +1 charge and starting in a 1 mm FWHM size trap, when the 40 mm spectrometer mesh is flat. P_y is the preset momentum component in the simulation, P'_y is the calibrated value according to different calibration equations. (a) linear calibrations when B field is off. (b) linear calibrations when B field is on. (c) calibrations using Equation 4.8 with B field on. (d) histogram of the $|P_y - P'_y|$ residual, after calibrating with Equation 4.8.

affected by the quadrupole field, so the calibration is fitted by a linear function,

$$P_t = m(t - t_0) + b, \tag{4.9}$$

$t_0 = 25.1\,\mu s$ is the TOF center when $P_t = 0$. For $t > t_0$, $m = 0.3466(5)$ keV/c/ns and $b = -0.08(5)$ keV/c, for $t < t_0$, $m = -0.3428(11)$ keV/c/ns and $b = 0.86(11)$ keV/c.

On the other hand, the calibrations in the transverse directions are not linear. According to the discussions in Section 4.2, the transverse calibrations are determined to be Equation 4.8, a correlation between the x and y coordinates on the detector. Figure 4.6 shows the details of the transverse calibration in x direction, including comparisons between different calibrations. Figure 4.6 (a) shows the residual between the initial momentum component P_x and the calibrated value of P'_x, $|P_x - P'_x|$, when the quadrupole B field is off. The calibration is a linear relationship between P_x and x, which calibrates P_x well with only 20 keV/c residual at maximum, the residual is minimum at 0 displacement and increases with x. However, once the quadrupole field is on, the same linear calibration doubles the residual and the residual is maximum for 0 displacement, as shown in Figure 4.6 (b). Obviously the linear calibration doesn't work well when B field is on, since the deflection of $\Delta x = 0.06y$ is not corrected. Figure 4.6 (c) shows the residual after calibrations by Equation 4.8, the B field deflection from P_y is corrected by the "$m_y \cdot y$" term, the residual is even slightly smaller than Figure 4.6 (a), since the third order polynomial of x fits the non-deflected displacement better than a linear function. The second and third order components of the polynomial contribute 5% – 10% at maximum to the calibration when the displacement is 40 mm, which is considerable enough to be included in the calibration. A histogram of the residual is also shown in Figure 4.6 (d), from which the momentum resolution by calibrations with Equation 4.8 can be determined as 5 keV/c.

Similar analysis was also done for the y direction, the results are shown in Figure 4.7. Equation 4.8 still works the best when calibrating P_y, but the linear calibration isn't as bad as for calibrating P_x. Since $\Delta y = 0.02x$, the deflection in the vertical direction is only 1/3 of the horizontal direction,

4.3.3 ^{86}Rb Ions with Charge +4

Since later on we will use the +4 internal conversion events as a reference for calibrating the +1 photoions, the same analysis as the +1 ions was also done for the +4 ions, which were simulated in SimIon with 920 keV/c recoiling momentum and same distributions in directions and positions as the +1 ions.

The longitudinal component P_t is still linearly proportional to TOF, $P_t = m(t - t_0) + b$, and the TOF center $t_0 = 12.6\,\mu s$ for +4 ions. For $t > t_0$, $m = 1.3862(28)$ keV/c/ns and $b = 0.92(11)$ keV/c, for $t < t_0$, $m = -1.3723(53)$ keV/c/ns and $b = 0.46(21)$ keV/c.

As for the transverse direction, the same analysis as Figure 4.5 (b) shows $\Delta y = 0.04x$ and $\Delta x = 0.13y$ for the +4 ions, which is twice more than the deflections for +1 ions. To correct these deflections, we repeated the same analysis as the +1 ions, and the results are shown in Figure 4.8 and 4.9. The calibrations using Equation 4.8 still works great, the deflections by the quadrupole B field are well corrected and the residuals are at the same level as the linear calibrations when B field is off. Since the deflection effect is much worse for the +4 ions than the +1 ions, the residuals after linear calibrations with B field on is much higher, up to 120 keV/c for $|P_x - P'_x|$ and 60 keV/c

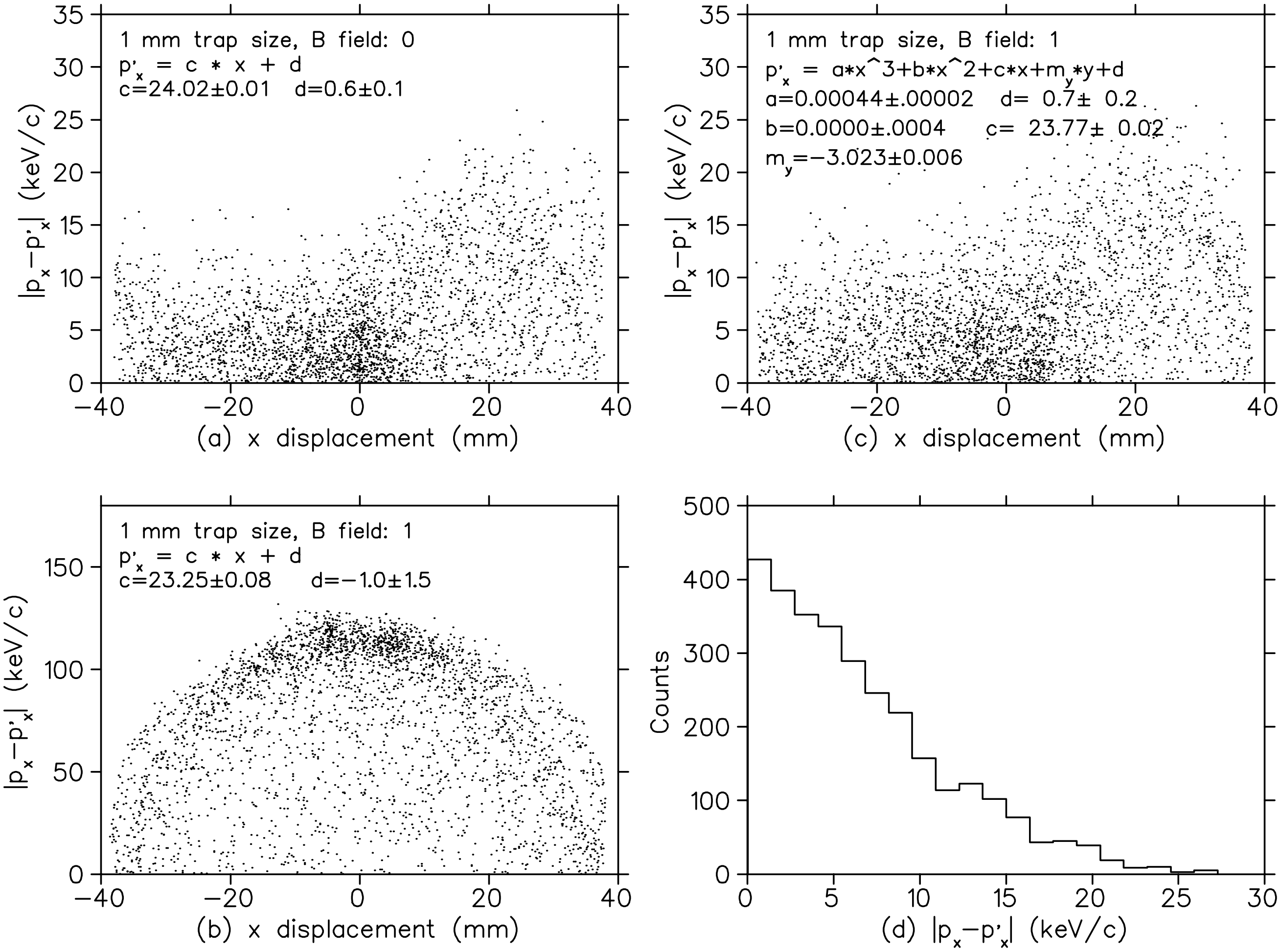

Figure 4.8: Momentum calibrations of the x component for ions with +4 charge and starting in a 1 mm FWHM size trap, when the 40 mm spectrometer mesh is flat. P_x is the preset momentum component in the simulation, P_x' is the calibrated value according to different calibration equations. (a) linear calibrations when B field is off. (b) linear calibrations when B field is on. (c) calibrations using Equation 4.8 with B field on. (d) histogram of the $|P_x - P_x'|$ residual, after calibrating with Equation 4.8.

for $|P_y - P_y'|$. However, the correction algorithm fixed the deflections and the achieved resolution on P_x or P_y is about the same as the +1 ions.

4.4 Momentum Resolution

While calibrating the recoiling momentum of the ^{86g}Rb ions, the expected momentum resolution dP is determined by the timing resolution of ions' TOF and the spatial resolution of the ion

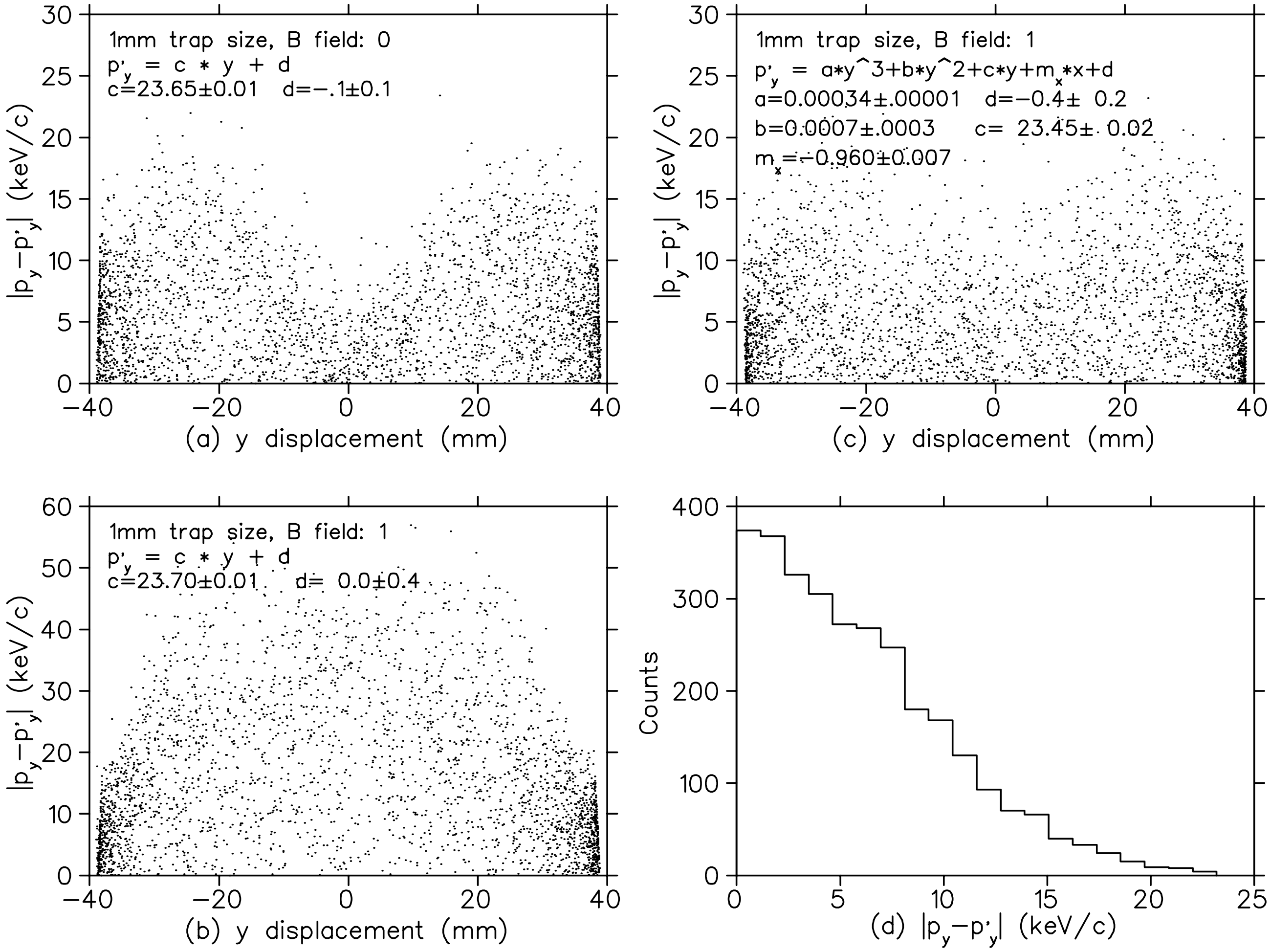

Figure 4.9: Momentum calibrations of the y component for ions with +4 charge and starting in a 1 mm FWHM size trap, when the 40 mm spectrometer mesh is flat. P_y is the preset momentum component in the simulation, P'_y is the calibrated value according to different calibration equations. (a) linear calibrations when B field is off. (b) linear calibrations when B field is on. (c) calibrations using Equation 4.8 with B field on. (d) histogram of the $|P_y - P'_y|$ residual, after calibrating with Equation 4.8.

detector, since

$$P^2 = P_t^2 + P_x^2 + P_y^2, \tag{4.10}$$

$$dP = (P_t dP_t + P_x dP_x + P_y dP_y)/P. \tag{4.11}$$

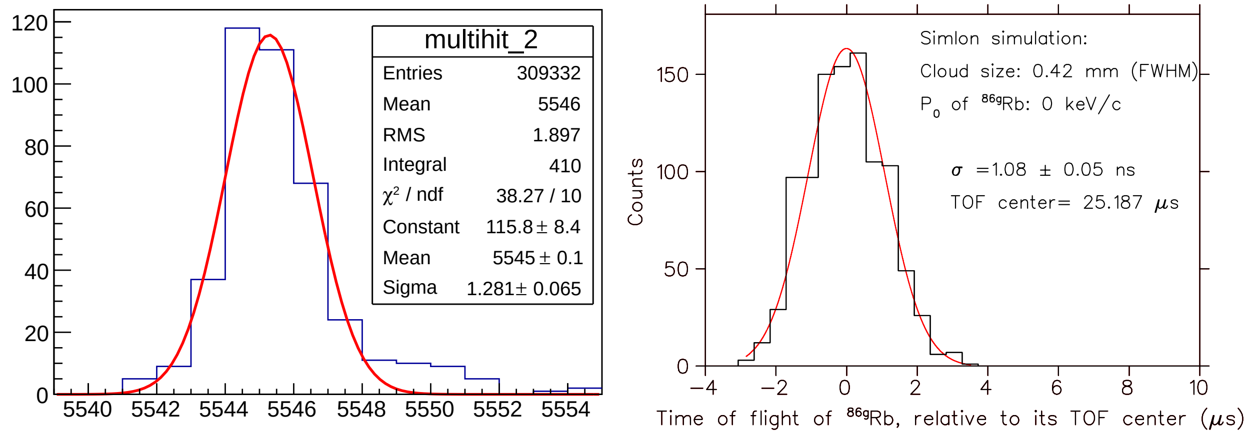

(a) Time resolution achieved in the ^{86}Rb experiment (b) ^{86m}Rb ions with 0 keV/c recoiling momentum.

Figure 4.10: Timing resolution the spectrometer, the x-axis units are ns in both graphs. (a) time resolution achieved in the ^{86}Rb experiment. The ^{86m}Rb atoms were trapped in the MOT for searching the $5S_{1/2}$ to $5D_{5/2}$ two-photon transition resonance. (b) SimIon simulation of ^{86m}Rb ions with 0 keV/c recoiling momentum.

According to the momentum calibrations using Equation 4.8 and 4.9,

$$\begin{aligned} dP_t &= 0.35dt, \\ dP_x &\simeq 12dx + 0.8dy, \\ dP_y &\simeq 12dy + 0.3dx \end{aligned} \tag{4.12}$$

for the +1 ^{86}Rb ions if we ignore the second and the third order terms of the polynomials for calibrating P_x and P_y. Then Equation 4.11 can be rewritten as

$$dP = [P_t \times 0.35dt + P_x(12dx + 0.8dy) + P_y(12dy + 0.3dx)]/P, \tag{4.13}$$

which gives the analytical relation between the momentum resolution dP and the timing resolution dt and the spatial resolution dx and dy.

4.4.1 Timing Resolution

The timing resolution of the experiment is determined by the resolution of the spectrometer's time focusing capability and the TDC's timing resolution(1/4 ns).

According to the discussion in Section 4.1.1, the time focusing resolution gets worse with the increasing longitudinal momentum component when the trap size is fixed. For ^{86}Rb ions with 0 recoiling momentum, the timing resolution can be determined by both the experimental data and SimIon simulations. Figure 4.10 (a) shows the experimental TOF histogram of the 0-speed ^{86m}Rb ions, when the $^{86\mathrm{m}}$Rb atoms were trapped in a MOT for searching the $5\mathrm{S}_{1/2}$ to $5\mathrm{D}_{5/2}$ two-photon transition resonance. The experimental timing resolution is found to be 1.28(7) ns by fitting a Gaussian profile. As a comparison, the simulation result by SimIon is 1.08(5) ns, as shown in Figure 4.10 (b). Although the simulation result is 2σ differed to the experimental value, they will match within 1σ if taking into account the TDC resolution of 1/4 ns.

For ^{86}Rb ions with the same non-0 recoiling momentum, there's no experimental way to testify their timing resolution, since we can't control the directions of the recoiling momentum. However, since the timing resolutions of the 0 momentum ions match in both the experimental data and SimIon simulation, we could use the simulation result of the 556 keV/c recoils as the upper limit of the spectrometer's timing resolution. The result is 1.6(1) ns, as shown in Figure 4.2.

In summary, the timing resolution dt of our spectrometer is 1.3(1) – 1.6(1) ns, depending on the longitudinal momentum components. The TDC resolutionf of 1/4 ns is small enough to be neglected. Since $dP_t \simeq 0.35\ dt$, the momentum resolution in the longitudinal direction is 0.6 keV/c at maximum.

4.4.2 Spatial Resolution

The spatial resolution is determined by several factors, including the resolution of the spectrometer's momentum focusing capability, the trajectory deflections by the quadrupole magnetic field, and the position distortion by the time jittering of the DLD80 signals and the E field nonuniformity between the back MCP and DLD80.

The transverse momentum calibrations by Equation 4.8 includes the momentum focusing resolution and also corrects the B field deflection. The calibration residuals imply a resolution of about 5 keV/c, as shown in Figure 4.6 (d) and 4.7 (d). On the other hand, as discussed in Section 3.4.4, the spatial resolution of our ion detector is about 0.4 mm. This will result in 5 keV/c uncertainties in the transverse momentum reconstructions, since the linear slope of the calibration equations (see Figure 4.6 and Figure 4.7) for the transverse momentum is $\sim$ 12 keV/mm.

In summary, the resolution dP of the recoiling momentum would be around 7 keV/c. This is mostly from the uncertainties in transverse momentum components, including 5 keV/c caused by the detector's spatial resolution and another 5 keV/c caused by momentum calibrations.

Chapter 5

The ^{86}Rb Experiment

In this chapter, I will first show the TOF spectrum and r vs TOF diagram of all charge states. Then I will discuss the internal conversion events, which happened naturally with a 2% branching ratio and have a much better signal to background ratio than the +1 photoions. Based on the analysis of the internal conversion events, we found a 30% inconsistency in the transverse momentum calibration between the experimental data and the simulation. The reason turned out to be the sagging of the 40 mm spectrometer mesh.

Then I will explain the new SimIon simulations with a spherically-sagged spectrometer mesh, including the calibration equations for the +4 internal conversion events and +1 photoions, new simulated 2D MCP distributions and r vs TOF diagrams, and the comparison with the experimental data.

Using the new calibration equations from the simulation, we reconstructed the recoiling momentum for the +4 internal conversion events and the +1 photoions. The achieved resolutions will be discussed and compared with the predicted values. For the +1 photoions, I will also discuss the reason for the nonuniform background, along with the background simulations.

A test for the exotic particle search was also done by scanning across the momentum spectrum of the +1 photoions and fitting Gaussian profiles, and the branching ratio of emitting a potential massive particle will be deduced.

Because of the low photoionziation rate problem, we tested the possibility of increasing the 778 nm light intensity by a power buildup cavity. The design of the cavity will be explained, as well as the results from the optical table test and the chamber test.

At the end of the chapter, I will briefly describe the attempt to search for exotic particles in the decay of trapped ^{81}Rb isomers.

5.1 Run History

Dec 2007

The ion MCP assembly started sparking and did not stop at the beginning of the run. Observation through the vacuum viewports showed glowing of the MCP assembly around several corners. This run was terminated, since the sparking problem could not be solved without breaking the vacuum. The reason for the sparking was found after disassembling the ion MCP: there were some sharp edges left on the MCP electrode ring, which was cut by scissors. After rounding off the sharp edges and adding in Kapton shielding around the MCP, the sparking problem was solved.

Aug 2008

ISAC radiative beam yield was 50x lower than requested, only 4×10^6/s for $^{86\mathrm{m}}$Rb. The count rate of $^{86\mathrm{g}}$Rb photoions was too low to search for the narrow two-photon transition on the Gamma-ray recoils. So we turned to trapping $^{86\mathrm{g}}$Rb instead since it has a 18-day half lifetime and 10x higher yield in the beam. We trapped $\sim 10^4$ of $^{86\mathrm{g}}$Rb and found one two-photon resonance frequency. Then the MBR laser frequency was locked to it and 90 minutes data were taken with the trapped $^{86\mathrm{m}}$Rb. There are about 6 events in the expected 556 keV/c recoil momentum peak. This run was our test run. All equipments worked and were confirmed to be ready for more beam time.

Apr 2009

During the 10 shifts beam time, the yield for $^{86\mathrm{m}}$Rb was 10^9/s, and the trap size was about 10^6. The background event rate on ion MCP was reduced from 700 Hz to 300 Hz, by adding more lead shielding between the detection chamber and the collection chamber.

We measured the Doppler-free two-photon spectra for $^{86\mathrm{m}}$Rb and $^{86\mathrm{g}}$Rb in this run, and tried to increase the photoionization rate for the fast-moving $^{86\mathrm{g}}$Rb, including hyperfine pumping, optimizing photoionization duty cycle. The data that will be analyzed in this chapter were all taken in this run.

Nov 2009

In this run, we switched to ^{81}Rb isomer decay. However, the background event rate was too high due to the electron capture decay of the long-lived $^{81\mathrm{g}}$Rb ($t_{1/2} = 4.6$ hours). Although the original search for exotic particles was not possible with this background, we successfully measured the two-photon transition spectrum in $^{81\mathrm{g}}$Rb.

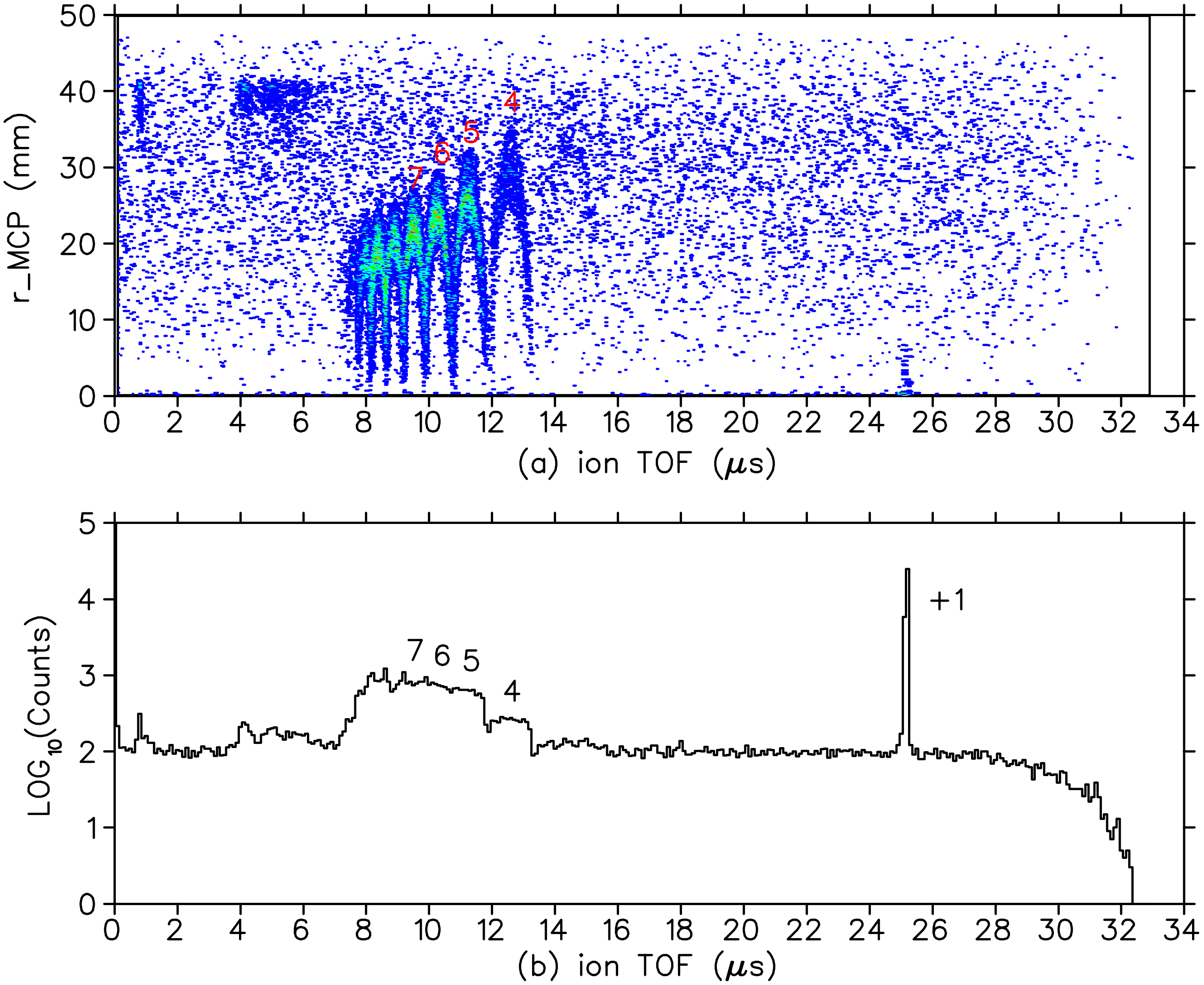

Figure 5.1: (a) The r vs TOF plot with elliptical patterns. The high-density ^{86m}Rb isomer photoions in channel 25.1 μs and 25.2 μs were cut off to make the density plot, otherwise, there will be only one spot shown around (25.1 μs, 0mm). (b) Time-of-Flight spectrum of all charge states, including the +1 photoion events and the internal conversion events. The charge states for +4 – +7 internal conversion events are labeled on the plot.

Apr 2012

The detection chamber was opened and the detectors were disassembled. The 40 mm spectrometer mesh was found to be sagged by 4 mm, which has been confirmed to be the reason for the 30% less transverse displacements of internal conversion events.

5.2 Time-of-Flight Spectrum and "r vs TOF" Diagram

Figure 5.1 shows the TOF spectrum and the corresponding r vs TOF diagram for the events we measured in the ^{86}Rb experiment, the total data-taking time was about 8 hours.

The TOF spectrum covers a timing spread of 0 – 34 μs, which includes both the +1 photoion events created by the MBR laser and the internal conversion events with charge states up to +10. The ions' TOF used in Figure 5.1 is not from the high-resolution TDC. Instead it was recorded by an auxiliary channel, using a timer with 100 ns resolution instead of 1ns. Although the auxiliary channel has low timing resolution, it covers a much wider range than the TDC and recorded all the events including the internal conversion events.

As discussed in Chapter 4, momentum calibrations by SimIon simulations showed that $p_t \propto$ TOF and $p_r \propto r$, where p_t is the longitudinal momentum component, and r is the displacement of the ion on the MCP detector due to the transverse momentum component p_r. If the size of the ion's recoiling momentum is fixed, then there will be a correlation between p_t and p_r,

$$\begin{array}{ccccl} p_t^2 & + & p_r^2 & = & \text{constant, or} \\ r^2/a^2 & + & TOF^2/b^2 & = & \text{constant.} \end{array} \tag{5.1}$$

This correlation will result in elliptical patterns on a r vs TOF plot, as shown in Figure 5.1 and Figure 5.3. Each elliptical pattern has a symmetrical shape. The symmetry center is the TOF center for ions with a given charge state, such as the 12.6 μs is the TOF center for +4 events. The TOF center corresponds to the ions with initial momentum along the transverse direction only, and thus approximately maximum displacements on the MCP detector.

The r vs TOF plot shows clear elliptical patterns for the internal conversion events followed by Auger electron emissions, including charge states +3 – +10. However, there is no clear pattern for the +1 photoion events, which are supposed to be centered at TOF = 25.2 μs with a ± 1.6 μs timing spread. The events in channel 25.1 μs and 25.2 μs are the $^{86\mathrm{m}}$Rb isomer photoions, which were trapped in the MOT and could be easily photoionized by the MBR laser even off-resonance.

The r vs TOF plot of Figure 5.1 also shows a high-density region at 4 – 6 μs and 35 – 40 mm. The far displacements of those events suggest that they did not start from the trap center, but from a position much biased transversely. The very short TOF can only be allowed for high charge state ions created by the Auger effect. A simple explanation is that those events were from highly charged $^{86\mathrm{g}}$Rb ions on the electrode rings. The $^{86\mathrm{m}}$Rb isomers can survive very long in the research chamber, since they have a half-life of 1 minute while the trap half-life is about 15 seconds. Some of the $^{86\mathrm{m}}$Rb atoms stick on the electrode rings and decay into high charge state $^{86\mathrm{g}}$Rb ions by internal conversions and the following Auger processes.

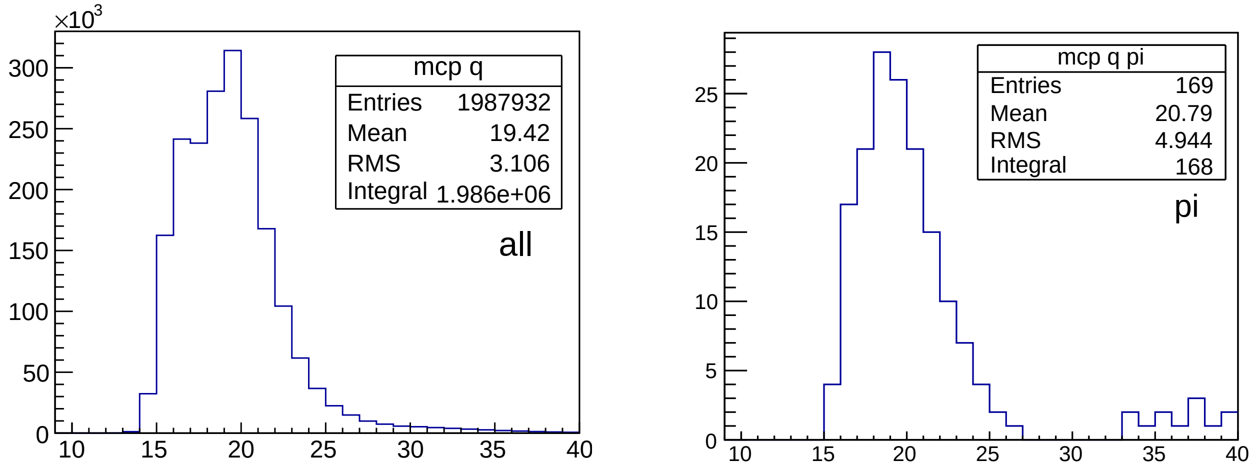

(a) all events

(b) events within $25.1 \pm 1.6\mu s$, the time window for +1 photoions

Figure 5.2: MCP pulse height distribution of run #2512, the x axes are the charge "Q". (a) all events, (b) events within $25.1 \pm 1.6\mu s$ time window.

5.3 Isomer Events and MCP Pulse Height

According to the estimations in Section 3.6.5, the isomer event rate would be 29× the daughter event rate, and the isomer events dominate at the low momentum tail of the recoiling momentum spectrum. However, the isomer events can easily be discriminated in the momentum reconstruction, due to their special features of being trapped in a 1mm cloud and nearly-zero speed. Their displacements on the ion detector are determined by the MOT cloud size, which is about 1mm and the isomer event distribution on the detector is clearly shown in Figure 5.15 (a). On the TOF spectrum, they all arrive the ion detector at about the same time, bin 25.1 μs and 25.2 μs as seen in Figure 5.1 b, which include about 40K isomer events in 8-hours data.

Besides the isomer event cut, we also did a cut on the ion MCP pulse heights. These were recorded by a capacitor and the induced charges on the capacitor are proportional to the pulse heights. The MCP pulse height for gamma accidentals is usually smaller than the Rb ions. The pulse heights for ion signals are from 1 or 2 electrons made at the very beginning of the MCP with full gain, but the gamma accidentals make a secondary electron somewhere deeper in the MCP with less gain. In principle, the signal to noise ratio for the ^{86g}Rb recoils can be improved by cutting off the low charge tail on the pulse height distribution. As an example, the MCP pulse height distribution of run #2512 is shown in Figure 5.2, including the distributions of all events (mostly gamma accidentals), and events within the photoion time window of $25.1 \pm 1.6\mu s$. By cutting off events at $Q \leq 18$, there is a 34% loss for all events but 25% loss for events within the photoion time window. However, the signal to noise ratio is not improved by this cut, since

$$\frac{S}{N} = \frac{S(1-0.25)}{\sqrt{B(1-0.34)}} \simeq 0.9\frac{S}{\sqrt{B}} < \frac{S}{N}. \tag{5.2}$$

So the events within the photoion time window are still mostly gamma accidentals.

5.4 The 30% Spatial Inconsistency

By comparing the elliptical patterns for internal conversion events, we found a 30% inconsistency of the ions' MCP displacements between the experimental data and SimIon simulations, as shown in Figure 5.3 (a) and (c). As an example, the maximum displacement for the +4 events from the experiment is around 29 mm, but the SimIon simulation suggests it should be at 38 mm, which is 30% more than the experimental data. Because of this inconsistency, the momentum reconstructions for the photoions and the internal conversion events result in big offsets from the nominal peak values of 556 keV/c and 919 keV/c, respectively.

Although the ions' MCP 2D distributions did not match with the simulation results, the TOF data agrees very well with the simulation (within 100 ns accuracy out of tens of μs TOF). As we can see in Figure 5.3 (a) and (c), the TOF center for the +4 internal conversion events is $t_4^0 = 12.6(1)\mu s$ in both the experimental data and the simulations. As for the +1 photoions, the TOF center is $t_1^0 = 25.1(1)\mu s$, as shown in the experimental data of Figure 5.1. This also agrees with SimIon simulations within 100 ns.

5.4.1 Preliminary Momentum Reconstruction

The internal conversion events have a much better signal to noise ratio than the +1 photoions, and the MCP images clearly shows their distribution above the background, as shown in Figure 5.4. Although the calibration equations from the simulation in Section 4.3 do not work for the transverse momentum reconstructions, we can optimize the momentum calibrations to give correct transverse momentum reconstruction by finding out the centers and the maximum displacements for the internal conversion events based on their 2D MCP images. Wherever the longitudinal calibration from the SimIon simulation was not affected by the sagging spectrometer mesh, it could still be used in the momentum reconstructions for either the +1 photoions or the internal conversion events.

As an example, the calibration equations of the +4 internal conversion events were determined

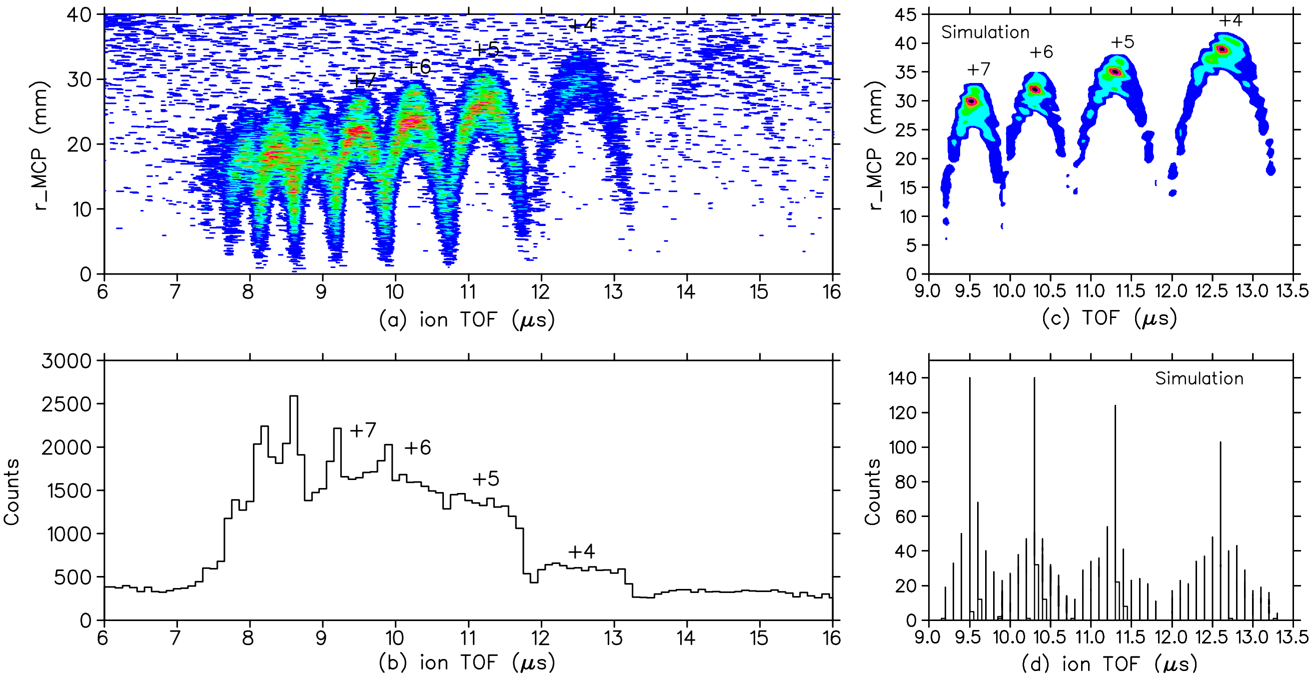

Figure 5.3: The internal conversion events. (a) elliptical diagrams for charge states +3 – +10, (b) TOF spectrum measured by the auxiliary channel with a 100 ns resolution. (c) elliptical diagram for charge states +4 – +7 by SimIon simulations, with a flat 40 mm spectrometer mesh. (d) TOF spectrum in SimIon simulation.

to be

$$\begin{aligned} p_{4r} &= r_4 \times 31.2\ \mathrm{keV/mm}, & (5.3)\\ p_{4t} &= (t_4 - t_4^0) \times 1.4\ \mathrm{keV/ns}. & (5.4) \end{aligned}$$

The transverse calibration coefficient of 31.2 keV/mm comes from the maximum displacement of 29 mm for the 919.3 keV/c recoiling momentum, as shown in Figure 5.13. The reconstructed momentum spectrum for the +4 events is shown in Figure 5.5 (a), which centers around 920 keV/c with an 8% width in σ.

As for the less obvious photoion events, the transverse calibrations cannot be optimized by the elliptical shape, since there's no clear pattern on the 2D MCP image. However, they can be deduced by scaling the transverse calibrations of the internal conversion events. According to Equation 4.1 and 4.2, if the initial longitudinal speed of the ions is $v_0 = 0$, then

$$\begin{aligned} t_{1s} &= \sqrt{2s/a} \propto 1/\sqrt{a}, \\ t_{1d} &= d/\sqrt{2as} \propto 1/\sqrt{a}, \end{aligned} \qquad (5.5)$$

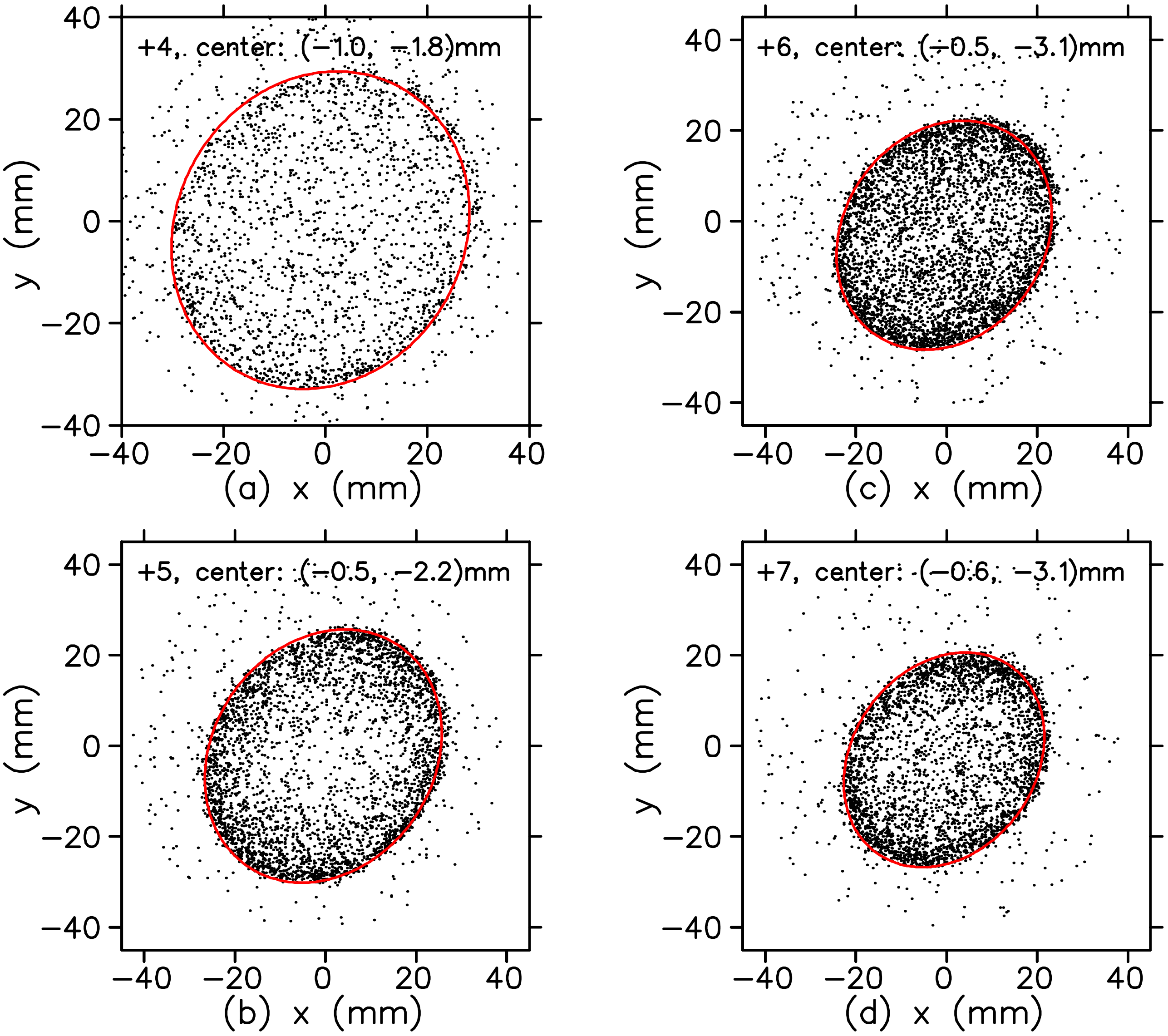

Figure 5.4: 2D MCP image of the internal conversion events with different charge states. (a) +4 , (b) +5, (c) +6, (d) +7.

and the total TOF $t = t_{1s} + t_{1d} \propto 1/\sqrt{q}$ since $a = Eq/m$. For ions with different charge states q_1 and q_2, the ratio between their TOF would be $t_1/t_2 \propto \sqrt{q_2/q_1}$. For one example, the TOF ratio between the +1 events and the +4 photoions should be $\sqrt{4/1} = 2$. This is consistent with the measured TOF centers: 25.1 μs for the +1 photoions and 12.6 μs for the +4 internal conversion events, as shown in the r vs TOF plot of Figure 5.1 (a).

The ions' transverse momentum components are proportional to their displacements on the ion detector, $P_r \propto r$, and $r = v_r\, t$, since there's no transverse acceleration by the electric field. If we define the calibration coefficient as ε, and $\varepsilon = P_r/r$, then for the +1 photoions and the +4 internal

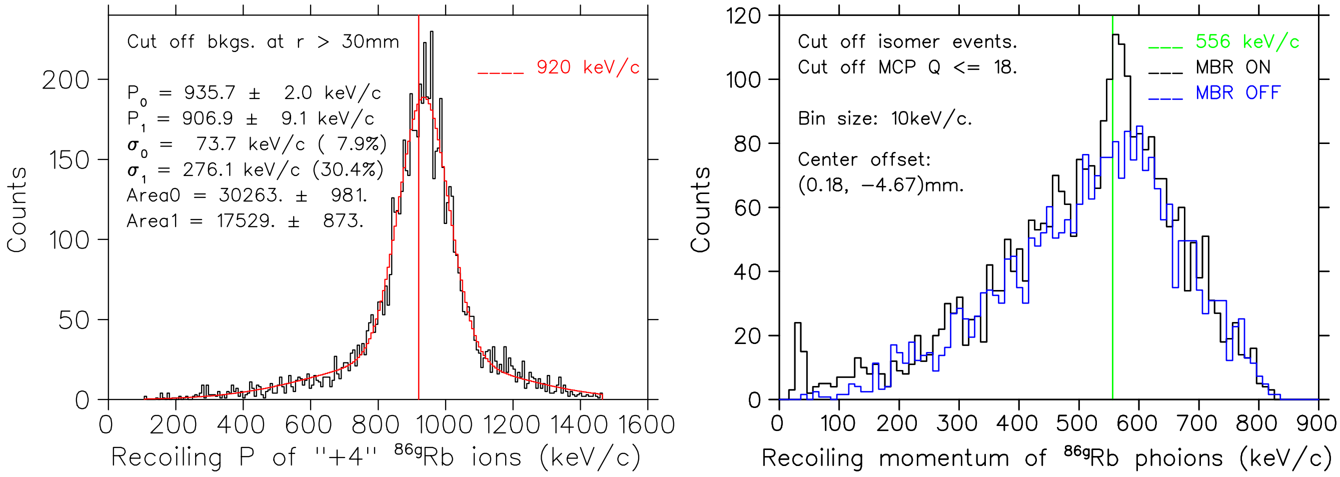

(a) +4 internal conversion events (b) +1 photoions

Figure 5.5: Recoiling momentum spectrum after corrections by the elliptical patterns on 2D MCP images. (a) +4 internal conversion events, fitted by a sum of two Gaussian profiles. (b) +1 photoions, the transverse calibrations are scaled down from the +4 internal conversion events.

conversion events, we have

$$\begin{aligned} \varepsilon_1 &= P_{1r}/r_1 = P_{1r}/(v_{1r}\,t_1) = m_{86}/t_1, \\ \varepsilon_4 &= P_{4r}/r_4 = P_{4r}/(v_{4r}\,t_4) = m_{86}/t_4. \end{aligned} \tag{5.6}$$

So $\varepsilon_1/\varepsilon_4 = t_4/t_1 \propto \sqrt{q_1/q_4} = \sqrt{1/4} = 1/2$, which is the scaling factor of the transverse calibrations between the +1 photoions and the +4 internal conversion events. By scaling down the coefficient in Equation 5.3, the calibration equations for the +1 photoions were found to be

$$\begin{aligned} p_{1r} &= r_1 \times 15.6 \text{ keV/mm}, \\ p_{1t} &= (t_1 - t_1^0) \times 0.35 \text{ keV/ns}, \end{aligned} \tag{5.7}$$

and the resulting momentum spectrum is shown in Figure 5.5 (b).

5.4.2 Inconsistency Discussions

Based on the elliptical pattern on the 2D MCP image, we deduced the transverse calibration coefficient for the +4 internal conversion events and reconstructed their recoiling momentum. The recoiling momentum for the +1 photoions was also reconstructed using calibration equations which were scaled down from the +4 internal conversion events. Both spectra in Figure 5.5 showed correct peak values.

However, the spectrometer seemed to not work as planned in the transverse direction. Small

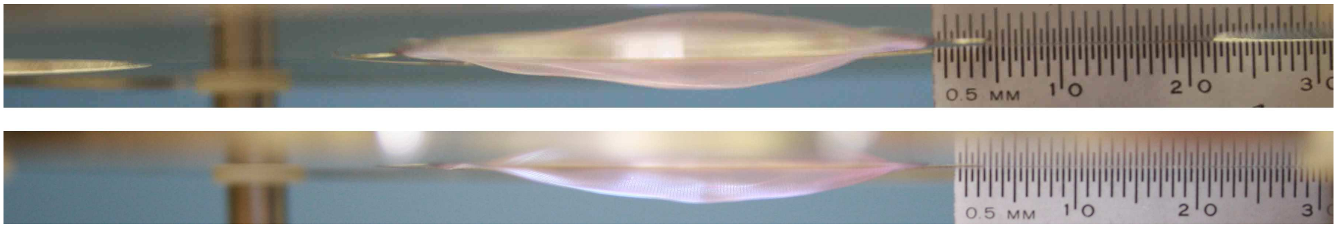

(a) side views

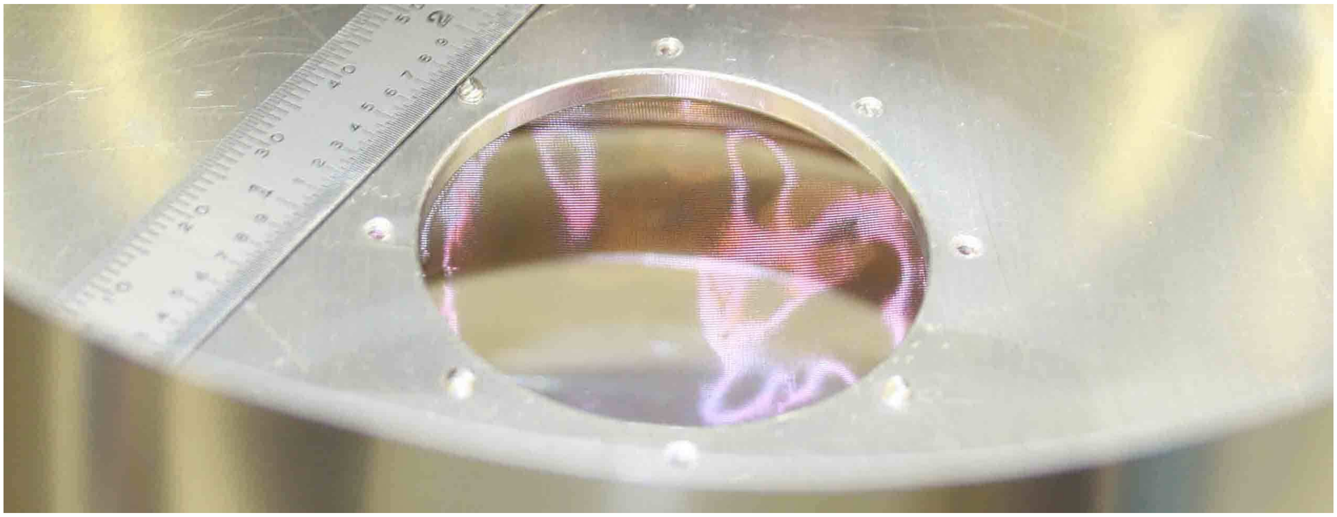

(b) surface distortion

Figure 5.6: Sagging geometries of the 40 mm spectrometer mesh. (a) side views. The spectrometer mesh was sagged by 3 – 4 mm. The upper picture is along the horizontal direction, the lower one is along the vertical direction. (b) surface distortions.

distortions of the aluminum electrodes or the 1 mm fluctuation on the 80 mm ion MCP mesh cannot explain the 30% spatial inconsistence. We also did detailed investigations in SimIon, such as starting the ions from a far-offset location instead of the trap center, and adjusting the geometry of the ion MCP assembly. None of these analysis could explain the 30% spatial inconsistence without affecting the well-consistent TOF.

5.5 The Sagged 40 mm Spectrometer Mesh

5.5.1 Sagging Geometry

When we opened the chamber in April 2012, a close examination on the spectrometer and the detectors showed no distortion on the 40 mm e$^-$ detector mesh (defined in Figure 3.1), and only small fluctuations (less than 1 mm) on the 80 mm ion detector mesh. However, the 40 mm spectrometer mesh was distorted and noticeably sagged.

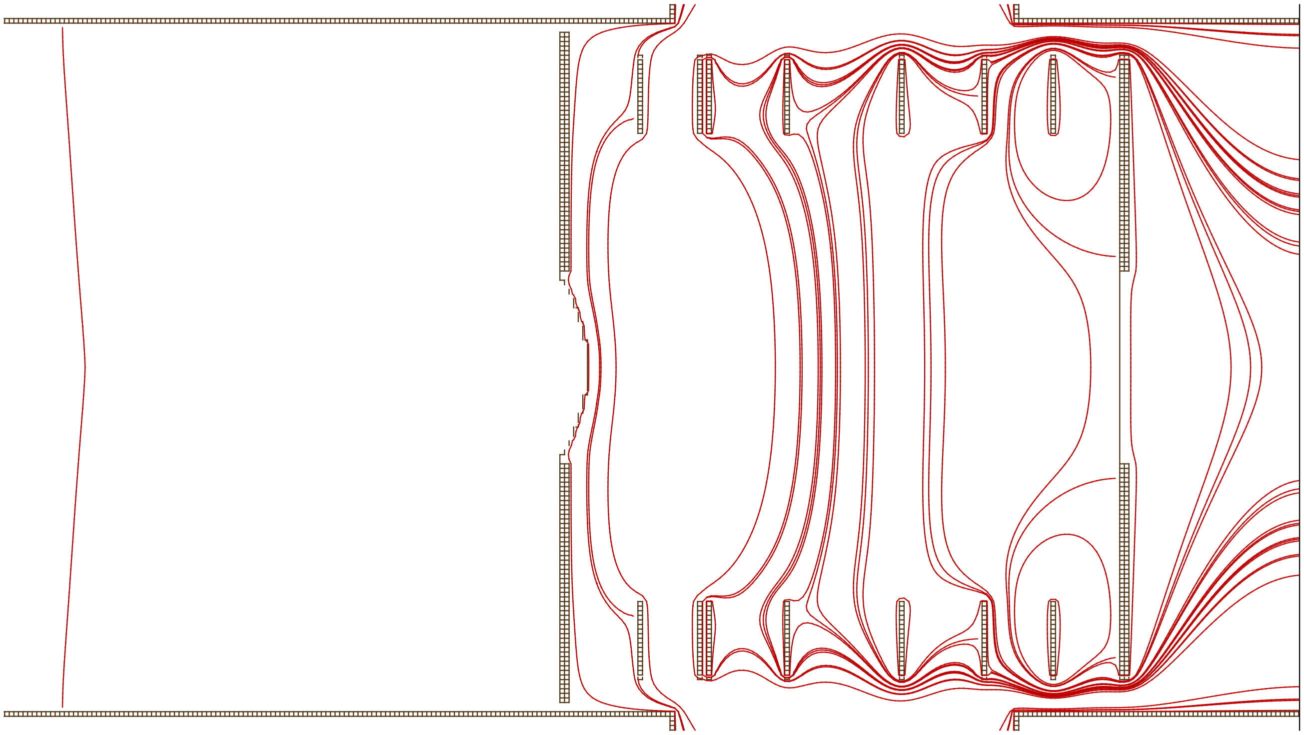

Figure 5.7: The electric field contours generated by the spectrometer, with the 40 mm spectrometer mesh spherically sagged.

Figure 5.6 (a) shows the sagging and side views in both dimensions, and Figure 5.6 (b) shows an image of the surface distortions on the mesh. The geometry of the sagging mesh shows a maximum sagging depth of 3 – 4mm. The shape looks more or less spherical, and symmetrical in the vertical direction but a little bit biased in the horizontal plane. The possible reason for this incidence could be an unnoticed touch on the mesh during assembling, or the unsecured clamping which was designed to use 8 screws but instead only 4 were on it.

5.5.2 Effects on The E-field

After we discovered that the 40 mm spectrometer mesh was distorted and sagged, new SimIon simulation have been done by replacing the flat mesh with a spherically sagged shape, according to the geometries specified in Section 5.5.1.

Figure 5.7 shows the new electric contour lines. The local electric field around the sagged mesh is distorted and acts like an electric lens. Ions' trajectories will be more focused after passing the sagged mesh, and the transverse displacements on the detector will be smaller comparing to the designed version with a flat mesh. As an example, new simulation for the +4 internal conversion events shows much smaller displacements on the ion detector comparing to the old simulation with flat mesh, as shown in Figure 5.13 (a). Most importantly, the new ion-MCP image matches well

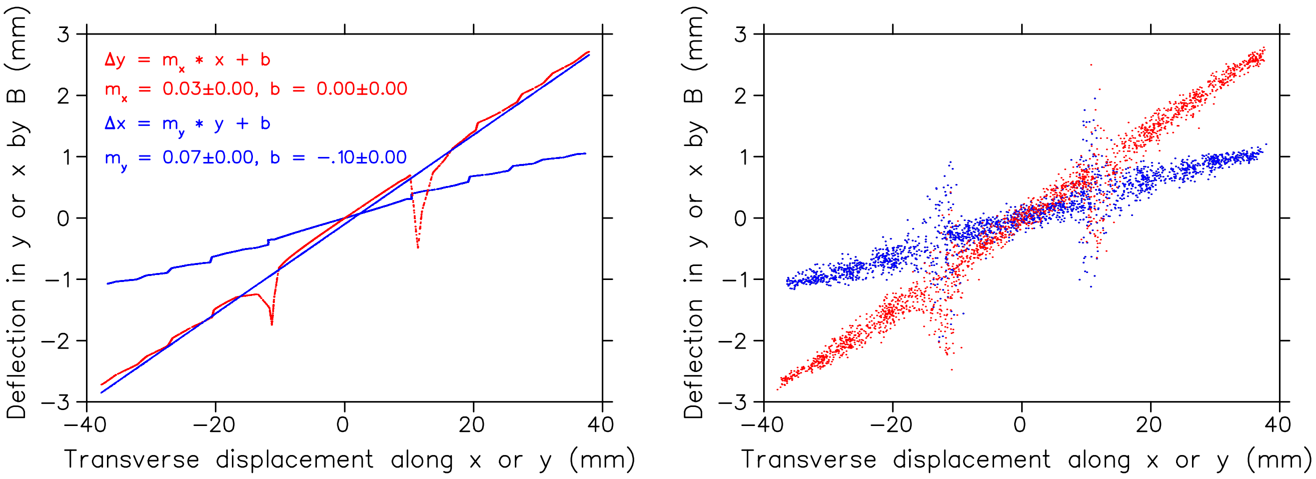

(a) 0 mm trap cloud size

(b) 1 mm FWHM trap cloud size

Figure 5.8: Trajectory deflection for +1 ions by the quadrupole magnetic field, when the spectrometer is sagged by 4 mm. (a) trap cloud size of 0 mm, (b) trap cloud size of 1 mm in FWHM.

with the experimental data after taking account of the center offsets, as shown in Figure 5.13 (b, c, d).

Figure 5.13 shows a clear evidence that the sagged 40 mm spectrometer mesh is responsible for the 30% spatial inconsistence between the design and the experiment. More interestingly, the ions' TOF is not affected by the mesh sagging, due to the time focusing capability of the spectrometer.

5.5.3 Effects on The Trajectory Deflection

To figure out the effects of the 4 mm sagging mesh on ions' trajectory deflections by the quadrupole magnetic field, we repeated the same analysis as Figure 4.5 (b).

The results are shown in Figure 5.8, which includes the deflections of Δx and Δy for 0 mm and 1 mm FWHM trap size. Although the fitting results in Figure 5.8 (a) are about the same as the case with a flat spectrometer mesh, the sagging spectrometer mesh causes heavy non-linearities, especially around the "± 10 mm" transverse displacements. Moreover, the nonlinearities get much worse for the 1 mm FWHM trap size.

If we ignore these nonlinearities and repeat momentum calibrations using Equation 4.8, the magnetic field deflections still can be corrected and the momentum residuals will be minimized to about the same level as B field off, as shown in Figure 5.9. The expected resolution by this calibration is about 10 keV/c, which is twice the resolution shown in Figure 4.6.

However, the 4 mm spherical sagging mesh simulated in SimIon (as shown in Figure 5.7) is just a rough estimation. The real geometry of the sagging in Figure 5.6 is much more complicated and impossible to replicate in SimIon, especially the surface fluctuations. Besides, the 1 mm resolution in SimIon simulation is also not good enough to show all the sagging details (more discussion in Section 5.5.4). We have tested the momentum reconstruction for the +1 photoions, using calibration equations derived from SimIon simulations with the 4 mm spherical sagging mesh (as the example shown in Figure 5.9 (c)), but the 556 keV/c peak is not improved comparing to Figure 5.5 (b).

In summary, the 4 mm spherical sagging estimation for the spectrometer mesh could solve the 30% inconsistency of the transverse displacements, as shown in Figure 5.13. However, correcting the magnetic field deflections with this sagging effect requires much more details of the mesh geometry, and the nonlinearities caused by the sagging mesh are also very difficult to correct. So we decided not to correct the magnetic field deflections in the following momentum reconstructions.

5.5.4 Calibration Equations

In this section, we will show the results of the momentum calibrations with a 4 mm spherical sagging mesh, but ignore the magnetic field deflections. The derived calibration equations will be used for calibrating the +1 photoions and +4 internal conversion events, as shown in Figure 5.17 and 5.14, respectively.

The new calibrations are shown in Figure 5.10, 5.11 and 5.12, which includes the simulation results for the +4 internal conversion events and the +1 photoions, respectively. The simulation for each species is divided into three parts, the longitudinal part, the horizontal part “x” and the vertical part “y”. For every part, we also distinguished the ion’s flying directions, such as towards/opposite to the ion detector, “±x” and “±y” directions. The reason for including all these geometry details is, that the spectrometer is not cylindrically symmetric. There are windows on the electrodes for the trapping lasers in the horizontal direction, and the magnetic field deflection is not the same for “±x” or “±y” either.

Each calibration equation was generated by firstly flying 2000 ions in SimIon along a specific direction which started from the trap center, with a uniform momentum distribution between 0 keV/c and 556 keV/c for +1 photoions (or 920 keV/c for +4 internal conversion events). The TOF simulation thus created a one-to-one relation between the ions’ initial momentum and the TOF or displacements on the ion detector. The relationships were then determined by fitting the data with linear or polynomial equations, depending on the linearity of the data.

As seen from the calibration figures, the calibrations in the longitudinal direction are quite linear, for either the flat spectrometer mesh or the sagged version. The coefficients of the linear relationships in those two versions are very close, only differing by about 0.7%. This means the sagged mesh did not change the ions’ TOF too much due to the time focusing ability of the spectrometer. However, the transverse calibrations look more like polynomial in both versions of

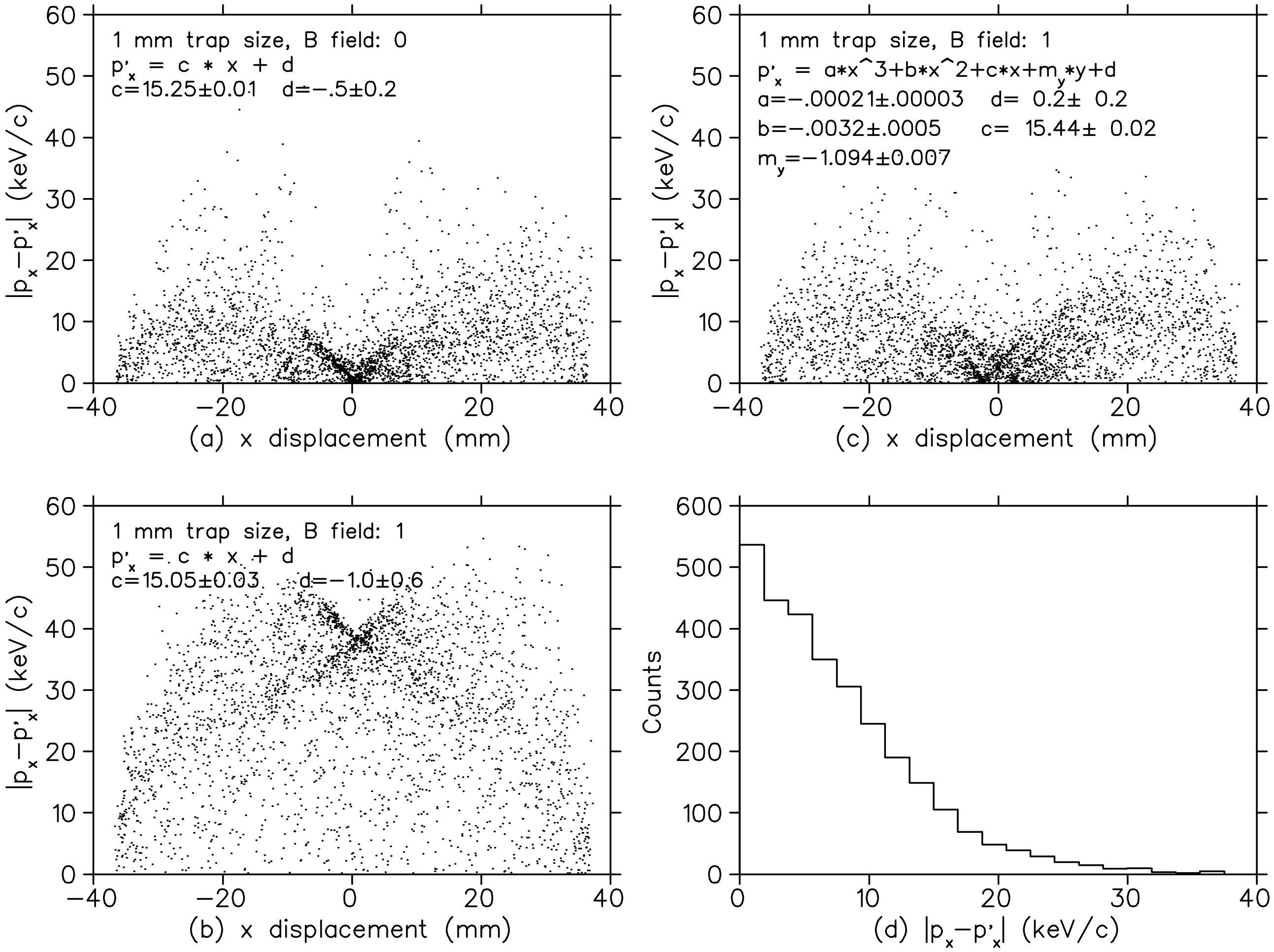

Figure 5.9: Momentum calibrations of the x component for ions with +1 charge and starts in a 1 mm FWHM size trap. P_x is the preset momentum component in the simulation, P_x' is the calibrated value according to different calibration equations. The 40 mm spectrometer mesh is simulated with a 4 mm spherical sagging. (a) linear calibrations when B field is off. (b) linear calibrations when B field is on. (c) calibrations using Equation 4.8 with B field on. (d) histogram of the $|P_x - P_x'|$ residual, after calibrating with Equation 4.8.

the spectrometer mesh.

For the spherically-sagged spectrometer mesh, the transverse calibrations are not smooth, such as Figure 5.11 and 5.12, which include 3 – 4 stepping regions in each figure. The reason for the steps is due to the the relatively low resolution for creating the spherically-sagging mesh in SimIon, which was designed to be 1 mm for the 306 mm x 260 mm x 401 mm overall size. As shown in Figure 5.7, the local E field contours around the spectrometer mesh is not smooth, and there are 4 – 5 steps on the mesh surface. Depending on the maximum displacements on the ion detector, ions with different charge states and different recoiling momentum will see 3 – 4 steps on the mesh and thus result in the same number of steps in the transverse momentum calibrations.

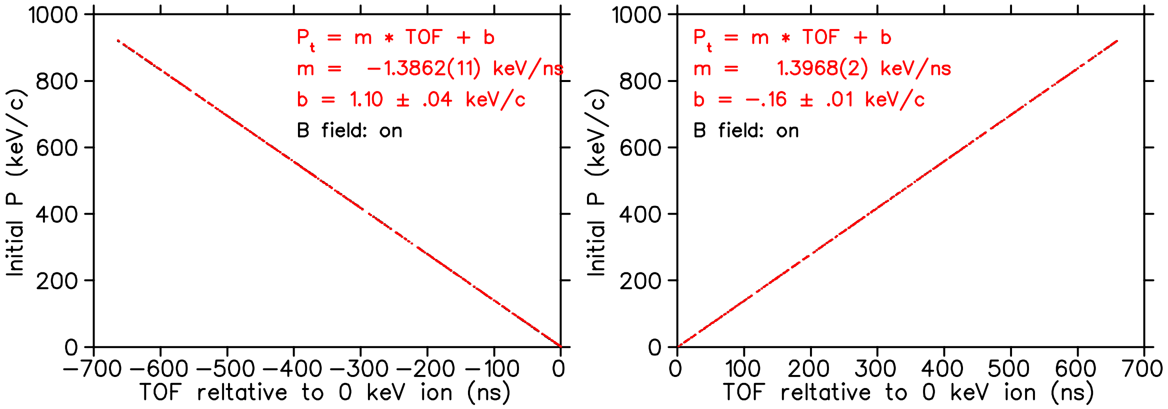

(a) +4 ions with 920 keV/c maximum momentum

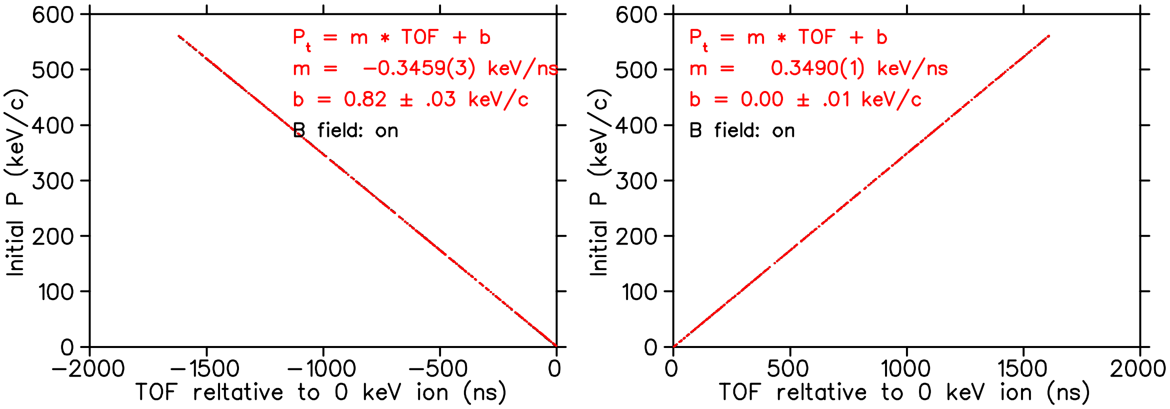

(b) +1 ions with 556 keV/c maximum momentum

Figure 5.10: Calibration equations for ions with recoiling momentum along the longitudinal direction, with a sagged spectrometer mesh. (a) +4 ions, (b) +1 ions.

The size of the steppings in the transverse calibrations can be decreased by increasing the spatial resolution in SimIon simulation. However, increasing the resolution by 2x will result in $2^3 = 8$x memory usage and computing time, which will reach the limitation of a normal desktop pc. Moreover, the spherical sagging is only an estimation of the sagging effect by ignoring the surface distortions, and the real geometry of the sagging mesh is hard to determine with high resolution. Since the current simulation results with the 1 mm resolution and the 4 mm spherical sagging have already matched the experimental data for the +4 internal conversion events (see Figure 5.13), we decided to continue with the 1 mm resolution in the following momentum calibrations.

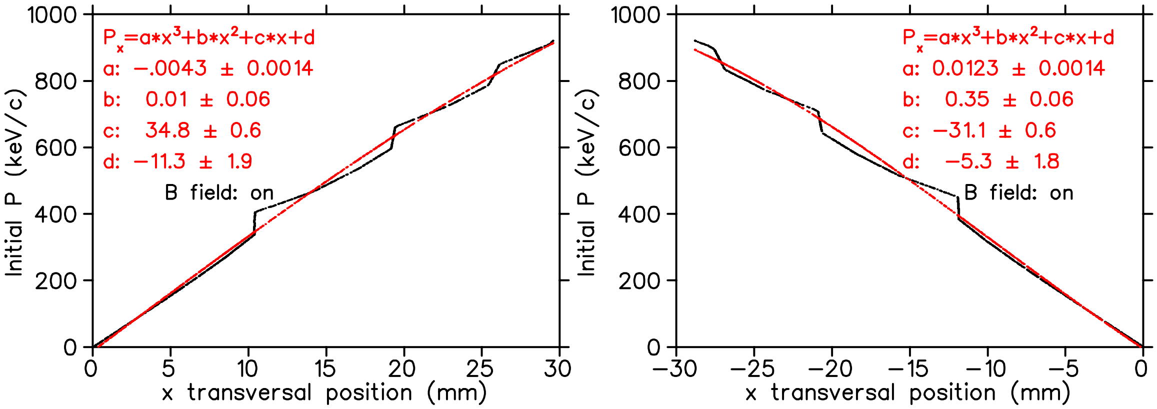

(a) transverse momentum calibration in ±x direction

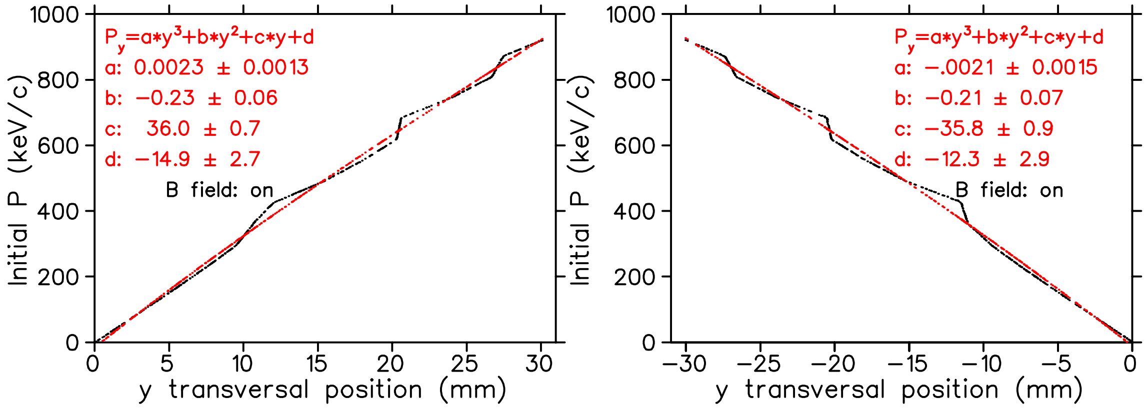

(b) transverse momentum calibration in ±y direction

Figure 5.11: Momentum calibrations for +4 ions in transverse directions, with a spherically-sagged spectrometer mesh. The steps are artificial effect due to the 1 mm resolution in SimIon simulations. (a) x component, (b) y component.

5.6 Internal Conversion Events

5.6.1 MCP 2D Images

Due to the range limitation of the high-resolution TDC, the internal conversion events were recorded by a 100 ns resolution auxiliary channel, as shown in the TOF spectrum and the r vs TOF plot of Figure 5.1 or Figure 5.3, which clearly shows the elliptical patterns for charge state +4 – +10. Even the charge state +3 is also visible.

Figure 5.4 shows the MCP 2D images for charge state +4 to +7. The internal conversion events can be easily distinguished from the backgrounds, and their patterns look more like elliptical than circular due to the trajectory deflections by the magnetic field. The center for each charge state is determined by fitting an ellipse to the data, which can be used for correcting the center offset of the ion detector.

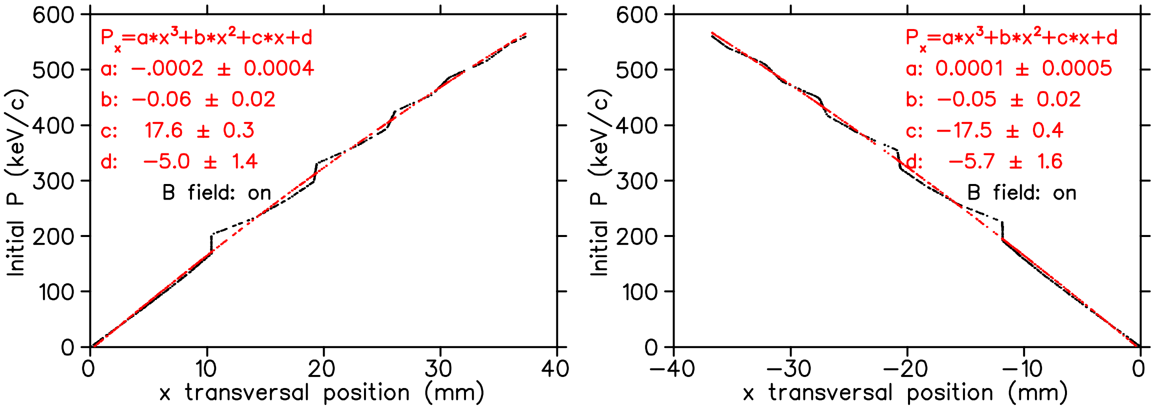

(a) transverse momentum calibration in ±x direction

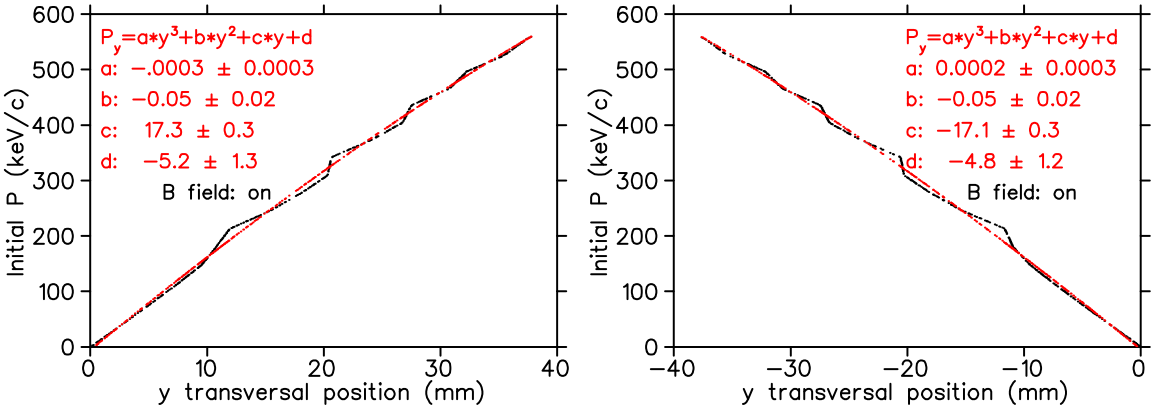

(b) transverse momentum calibration in ±y direction

Figure 5.12: Momentum calibrations for +1 photoions in transverse directions, with a spherically-sagged spectrometer mesh. The steps are artificial effect due to the 1 mm resolution in SimIon simulations. (a) x component, (b) y component.

Figure 5.13 shows the comparison between the experimental data of the +4 internal conversion events and the SimIon simulation results with a spherically-sagged spectrometer mesh. After correcting the center offsets for both data, the experimental data matches very well with the simulation, as shown in the 2D MCP image comparison. Their r vs TOF diagrams and the radial distributions match as well.

The +4 internal conversion events have a longer TOF than the higher charge states, and thus a bigger transverse displacement on the ion detector. This results in a better relative spatial resolution of $\Delta r/r$. We will use the +4 events as an example to analyze the internal conversion events, such as the momentum reconstruction and momentum resolution.

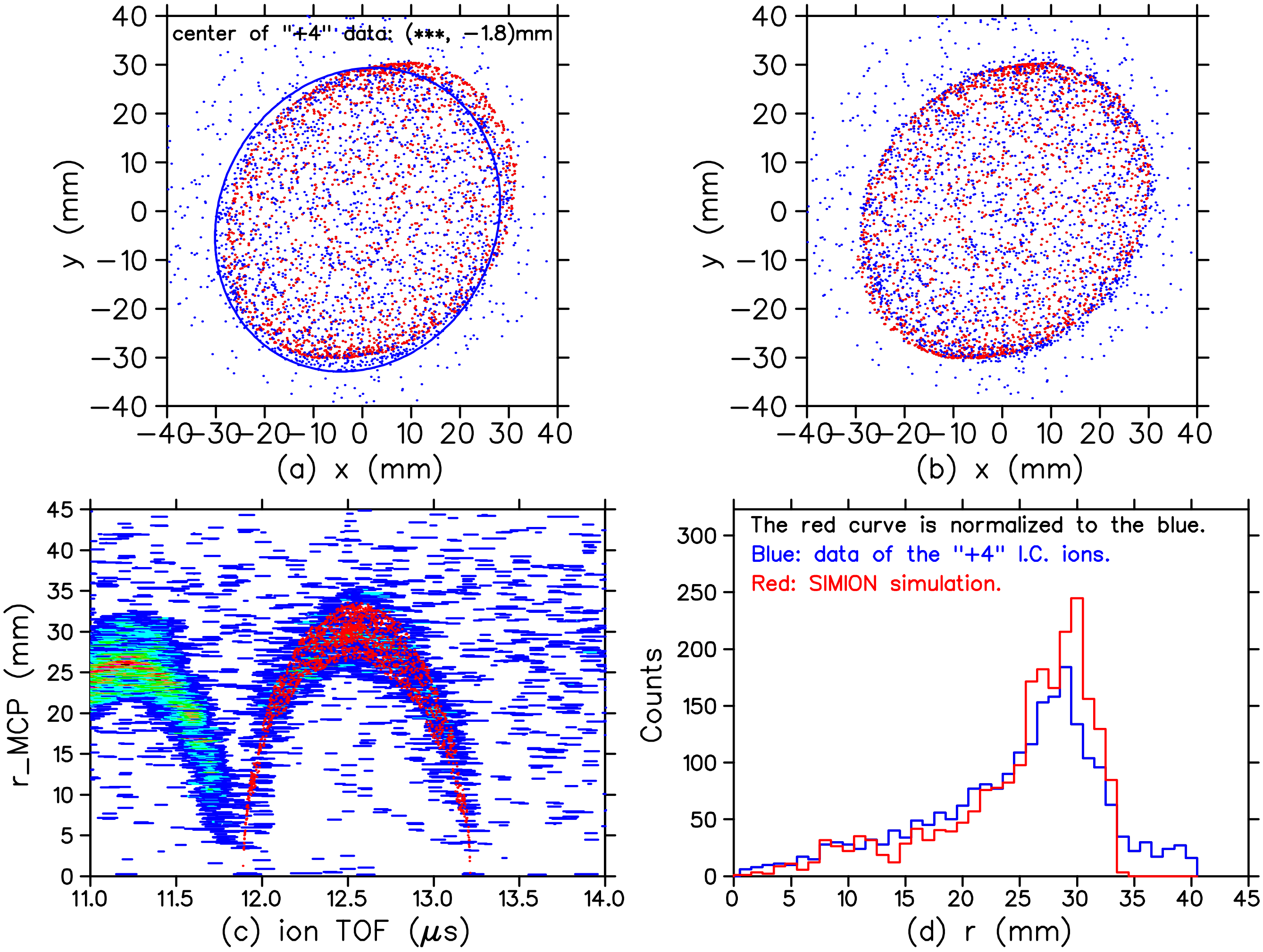

Figure 5.13: Comparison of the experimental data and SimIon simulation for the +4 internal conversion events. (a) 2D MCP images before correcting center offsets. (b) 2D MCP images after correcting center offsets. (c) elliptical pattern comparisons, (d) comparison of the radial distributions on the ion detector.

5.6.2 Momentum Reconstruction

The momentum reconstruction for the +4 internal conversion events was done using the calibration equations shown in Section 5.5.4, which was from the SimIon simulation with a spherically-sagged spectrometer mesh. The resulting momentum spectrum is shown in Figure 5.14, which excluded the background events at $r > 30$mm.

As discussed in Section 1.3.2, the internal conversion process is dominated by the K-shell conversion and L-shell conversion, with the nominal recoiling momentum of $P_K = 919.3$ keV/c and $P_L = 934.3$ keV/c, respectively. The reconstructed momentum spectrum was fitted by the sum of two Gaussian profiles as a test. The peak momenta were found to be 926(3) keV/c with a 68 keV/c width in σ, and 952(13) keV/c with a 193 keV/c width in σ. The peaks are about 2σ

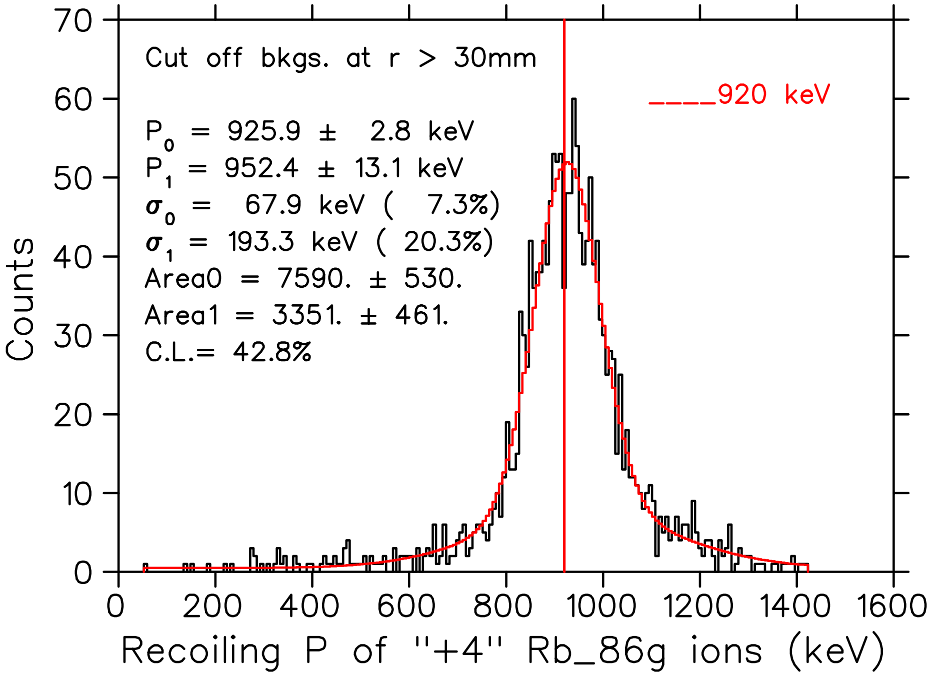

Figure 5.14: Momentum reconstruction for "+4" internal conversion events. The spectrum is fitted by a sum of two Gaussian profiles, the red line marks the nominal position of the 920 keV/c momentum.

away from the nominal values, which is quite good considering the rough estimation on the sagging geometries for the spectrometer mesh. However, the relative height between the 926 keV/c peak and the 952 keV/c peak is just 2.3:1, not consistent with the expected branching ratio of 7:1 [7].

Although the two Gaussian profile model found reasonable peak momentum values, this model is not sufficient for the complicated physical processes involved in the internal conversion decay. Since this experiment was not designed to investigate the physics of the internal conversion process, we will continue with the simple two Gaussian model.

5.6.3 Momentum Resolution

The momentum resolution for the internal conversion events is mainly affected by two factors, the spatial and timing resolution of the hardware, and the broadening effects by Auger electrons and X-ray photons.

The timing resolution for the internal conversion events is 100 ns, out of a total TOF spread of 1300 ns for +4 charge state. This results in 7.7% uncertainty for longitudinal momentum component. The maximum displacement for the +4 events on the ion detector is 29 mm, and the 0.4 mm spatial resolution of the detector corresponds to 1.4% uncertainty for the transverse momentum component.

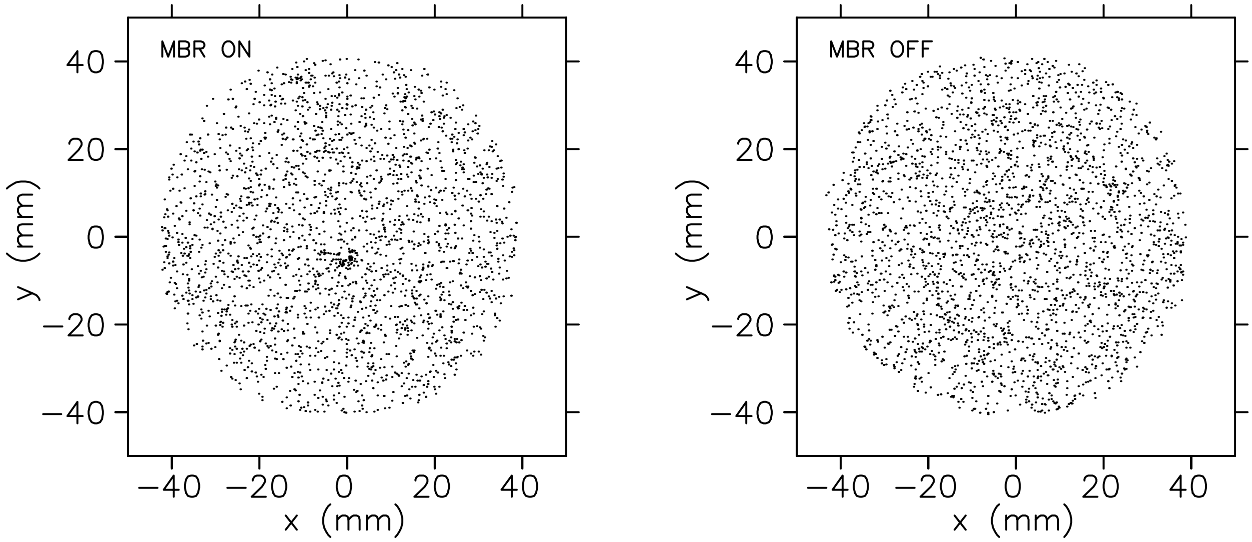

(a) 2D MCP image when MBR laser was on.

(b) 2D MCP image when MBR laser was off.

Figure 5.15: 2D MCP image of the +1 photoions.

As explained in Section 1.3.2, the Auger electrons will broaden P_K by 93 keV/c, and 35 keV/c for P_L. The emitted X-ray photons will also smear the ^{86}Rb recoiling momentum up to 15 keV/c.

5.7 +1 photoions

5.7.1 MCP 2D Image

Figure 5.15 (a) and (b) shows the 2D MCP images for the +1 photoions with the MBR laser on and off, respectively. There are no clear patterns for the fast-moving ^{86g}Rb daughters in the "MBR ON" figure, due to the low photoionization rate. According to SimIon simulations, the pattern should look like the one shown in Figure 5.16. The maximum transverse displacement for +1 photoions is decreased by 20% due to the sagging spectrometer mesh.

The high-density cloud around the MCP center in the "MBR ON" figure are events from the isomers, which were trapped and can be easily photoionized when the MBR light is on. The center of the +1 ^{86g}Rb photoions can be determined based on the isomer event cloud, since the isomer events act like the ^{86g}Rb events with 0 transverse momentum and the hitting position on the ion MCP is close to the ^{86g}Rb cloud center. The isomer event center is determined to be (-0.18,-4.67)mm, according to the isomer cloud on the "MBR ON" 2D image in Figure 5.15 (a). This is also consistent with the isomer event center created by a 355 nm pulse laser, and will be used as the center for the daughter events in the momentum reconstruction.

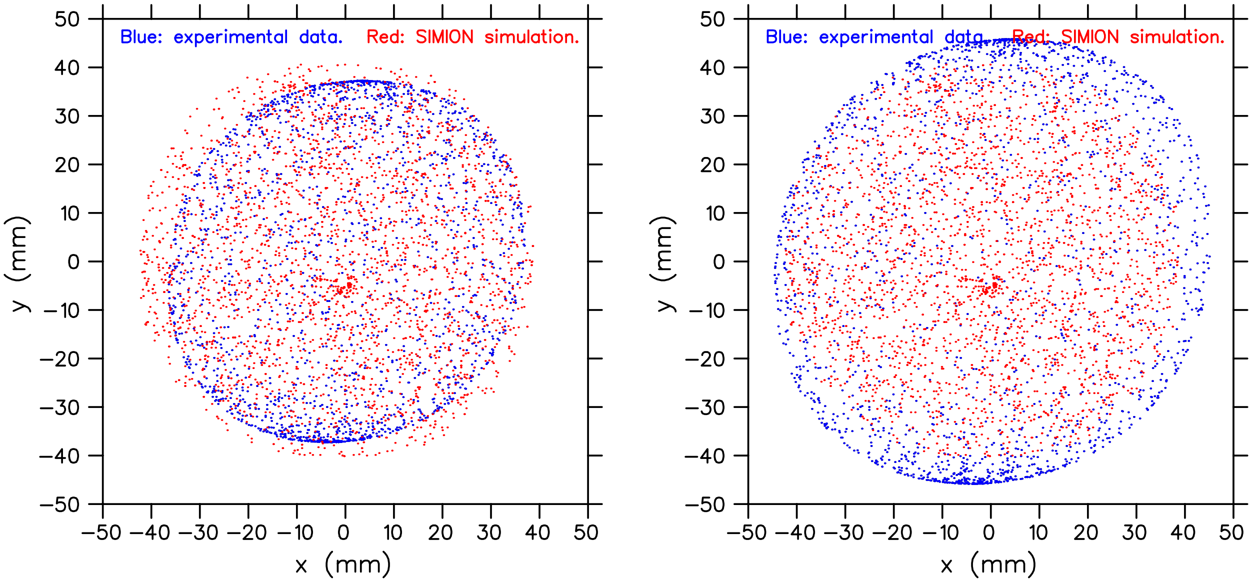

(a) spherically-sagged spectrometer mesh.
(b) flat spectrometer mesh.

Figure 5.16: 2D MCP image comparison of the experimental "MBR ON" data (in blue color) and the SimIon simulation result (in red color) for +1 photoions. The center offset of the simulated data has been corrected. (a) simulation with a spherically-sagged spectrometer mesh, (b) simulation with a flat spectrometer mesh.

5.7.2 Momentum Reconstruction

Using the calibration equations shown in Figure 5.10 and 5.12, we reconstructed the recoiling momentum for the +1 photoions. The results are shown in Figure 5.17, which includes three spectra: signal spectrum when MBR on, background spectrum when MBR off, and the background spectrum by simulations.

The signal spectrum shows the peak of +1 photoions around 556 keV/c, with about 150 counts above the background. The tails on both sides of the 556 keV/c peak match with both the experimental background "MBR OFF" and the simulated background.

There are three cuts in the momentum reconstruction of the +1 photoions: the isomer event cut, the MCP pulse height cut, and the MCP region cut. The isomer events cut was done by removing the central TOF channels of the ^{86}Rb ions and the central region of the ion detector, and the MCP pulse height cut was done by cutting off the photoions with "$Q \leq 18$". After the isomer event cut, there are still some isomer events left in the spectrum, as the peak around 40 keV/c in Figure 5.17, which is due to the tight spatial cut to avoid cutting out too many daughter events.

The MCP region cut was done according to the simulated 2D MCP image for the +1 photoions (as shown in Figure 5.16 a). The region outside the simulated image ($r > 40$ mm) was cut off in all three momentum spectra shown in Figure 5.17. Without this cut, the high-end tail above the

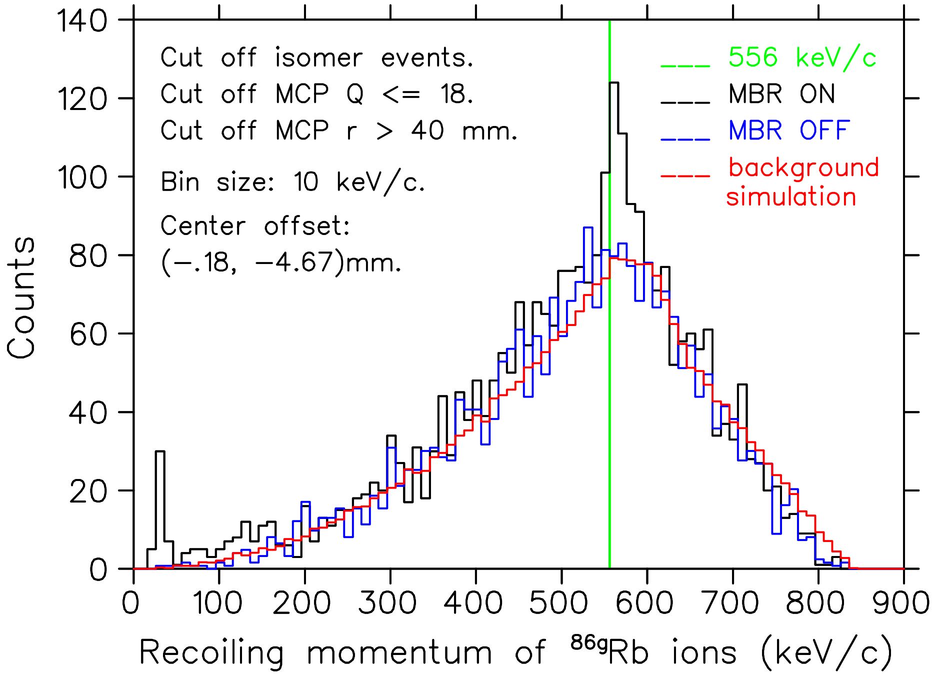

Figure 5.17: Reconstructed momentum spectrum for +1 photoions, including the signal spectrum when MBR laser is on, the experimental background spectrum when MBR laser is off, and the background spectrum by simulation. The green line marks the nominal position for the 556 keV/c momentum, and the signal peak around 556 keV/c shows the collected ^{86g}Rb events.

556 keV/c peak will extend to 1000 keV/c and not be consistent with the momentum spectrum of the simulated background.

5.7.3 Nonuniform Background

The accidental background spectrum is not flat, neither the simulation spectrum nor the "MBR OFF" spectrum. Instead, it increases with the recoiling momentum until a maximum at $\sim$ 556 keV/c, and then decreases. The reason for this special background spectrum is because the differential ring area dA of a circular detector is proportional to the radius,

$$dA = 2\pi\, r\, dr. \tag{5.8}$$

Since the transverse momentum is proportional to r, and the background events are almost uniformly distributed over the detector surface, the momentum reconstruction yields higher count rates for background events with higher transverse displacements. By contrast, the longitudinal momentum is almost uniformly distributed, as shown in the TOF spectrum of Figure 5.3 (b). Therefore, the nonuniformity in the momentum spectrum for background events arises solely from the transverse momentum reconstruction.

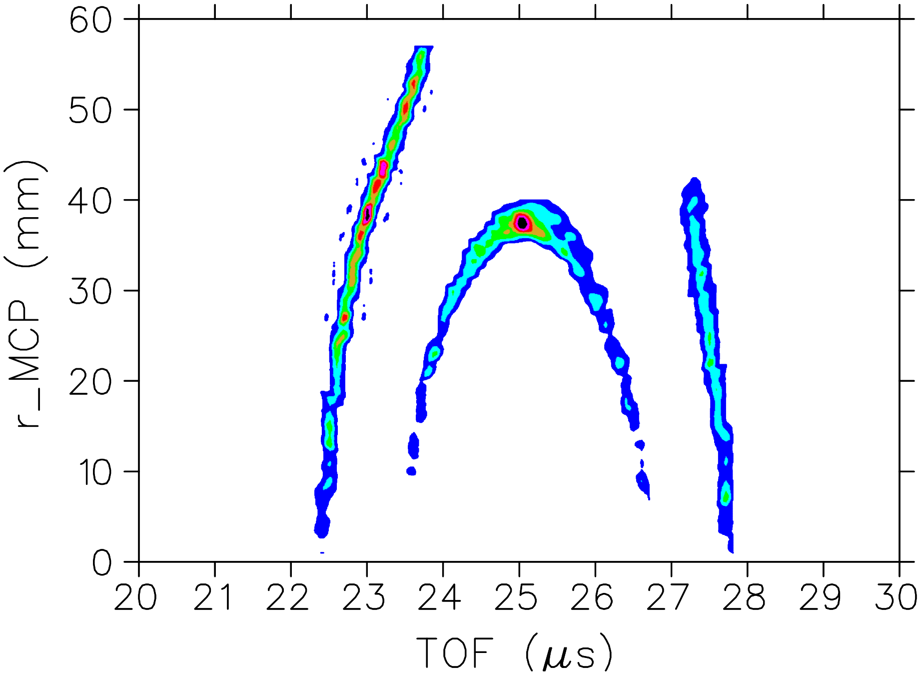

Figure 5.18: Elliptical diagrams of the 556 keV/c and 920 keV/c ions with the same charge state +1 by SimIon simulations, when the spectrometer mesh is spherically-sagged. The inner ellptical pattern is for the 556 keV/c ions. The outer pattern is for the 920 keV/c ions, and the broken shape is due to the ion's large transverse displacements and thus being stopped on the chamber walls before arriving at the ion detector.

The background simulation was done by assuming a uniform timing distribution between -1600 ns – +1600 ns (relative to the TOF center of the +1 photoions), and a uniform solid angle distribution in space. The reason for simulating a uniform solid angle distribution is assuming the backgrounds were mostly gamma rays emitted from the trap center and evenly distributed in all directions.

The internal conversion events do not contribute to backgrounds in the +1 photoions' momentum spectrum. The ions with charge states higher than +1 have much different TOF and are not recorded in the same timing window as the +1 photoions. The probability of emitting +1 internal conversion events is very low due to the quick processes followed. Even if they did pass through the acceleration region before transforming into higher charge states, their displacements on the ion detector will be too big to be detected by the ion MCP. The reason can be explained by Figure 5.18, which shows the simulated r vs TOF diagrams of the 556 keV/c and 920 keV/c photoions with the same charge +1. As we can see, in the timing window of the 556 keV/c ions, the 920 keV/c ions will have a radius bigger than 45 mm, which is outside the 40 mm radius MCP detector already.

To pick a random point on the surface of a unit sphere, the differential element of the solid

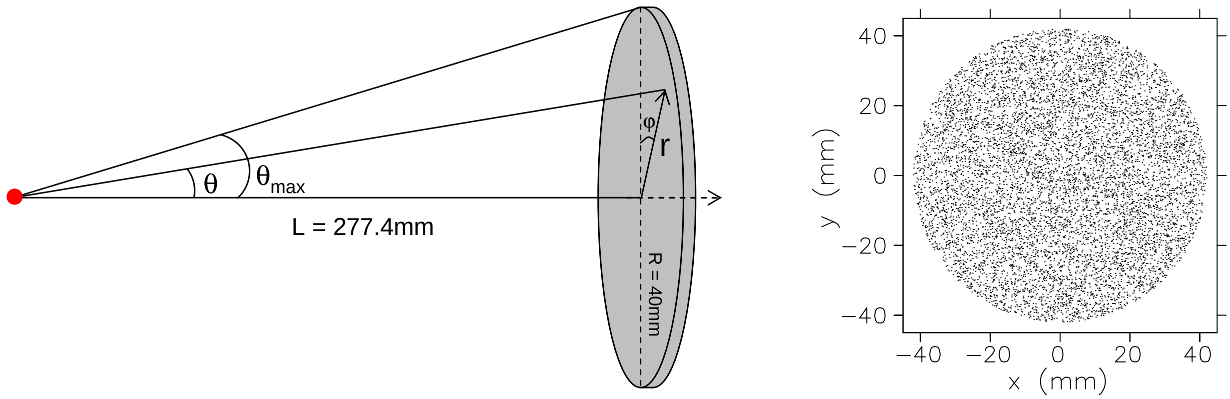

(a) coordinates.

(b) 2D MCP image of the simulated backgrounds.

Figure 5.19: Background simulation with a uniform solid angle distribution. (a) coordinates, (b) distribution of the simulated background events on the ion MCP.

angle $d\Omega$ must be uniformly distributed, instead of just the uniform distributions of $\theta \in [0, 2\pi]$ and $\phi \in [0, 2\pi]$. Since

$$d\Omega = sin\theta \, d\theta \, d\phi = -d(cos\theta) \, d\phi, \tag{5.9}$$

uniform distribution of $d\Omega$ requires $\phi \in [0, 2\pi]$ and $cos\theta \in [-1, 1]$. A common algorithm is to choose two random variables, $U, V \in (0, 1)$, then

$$\begin{aligned} \phi &= 2\pi U, \\ \theta &= cos^{-1}(1 - 2V) \end{aligned} \tag{5.10}$$

will give the spherical coordinates for a set of points which are uniformly distributed over the spherical surface.

In our experimental setup, the ion detector is 277.4 mm away from the trap center, with an effective radius of 40 mm. The maximum elevation angle θ_{max} is about 8.2°, as shown in Figure 5.19 (a). The range of θ can be chosen as

$$\theta = cos^{-1}(1 - (1 - cos\theta_{max})V), \tag{5.11}$$

resulting $cos\theta \in [cos\theta_{max}, 1]$, and the choice of $\phi = 2\pi U$ is good for covering all 2π angles on the MCP. The coordinates on the ion MCP are then determined by

$$\begin{aligned} x &= L \, tan\theta \, cos\phi, \\ y &= L \, tan\theta \, sin\phi. \end{aligned} \tag{5.12}$$

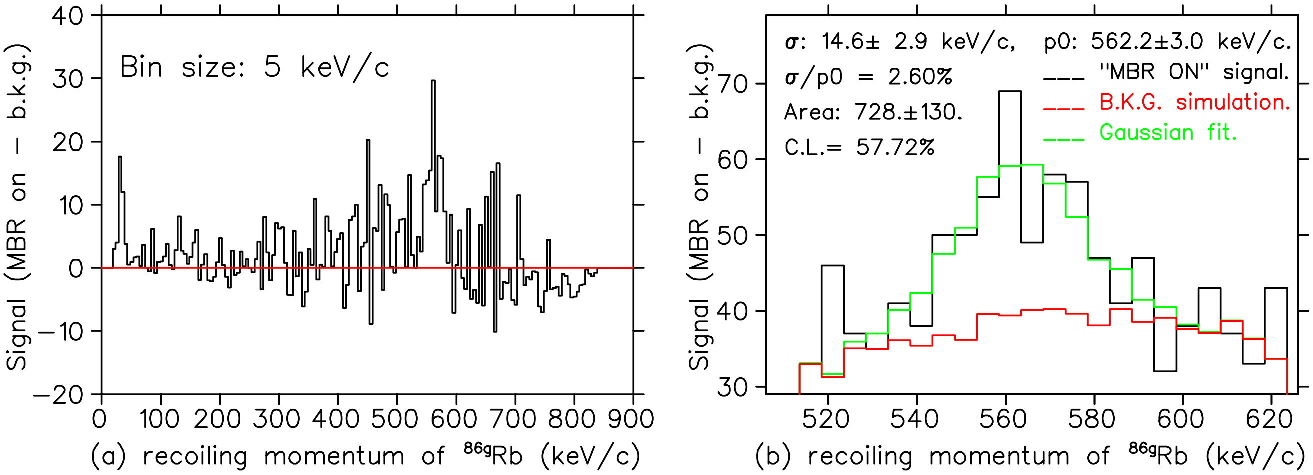

Figure 5.20: Recoiling momentum analysis for the ^{86g}Rb photoions. (a) “MBR ON” signal subtracts the simulated background, (b) Gaussian fit of the 556 keV/c peak.

The spatial distribution of the backgrounds on the ion detector is shown in Figure 5.19 (b), which includes about 9000 counts. The 3 dimensional coordinates (tof,x,y) for each background event are then constructed by combining these 9000 spatial coordinates with each TOF bin, and in total about 10^5 background events were simulated. The recoiling momenta of the simulated backgrounds were reconstructed using the same calibration equations as the experimental data, and the resulting spectrum matches with the “MBR OFF” spectrum very well, despite the statistical fluctuations.

5.7.4 Momentum Resolution

Figure 5.20 shows the analysis of the 556 keV/c peak, by fitting a Gaussian profile on top of the simulated background instead of the experimental background. The simulated background matches well with the experimental background but its statistical fluctuation is much smaller.

Based on the covered area under the peak, we could deduce the number of the 556 keV/c events, 728(130)/5 = 145(26). The fitting result also shows that the peak centroid is $p_0 = 562(3)$ keV/c, which is within 2σ of the 556 keV/c nominal value. The Gaussian width of $\sigma_{556keV} = 15(3)$ keV/c is equivalent to a relative momentum resolution of $\sigma/p_0 = 2.6\%$.

The achieved momentum resolution is twice the expected resolution of 7 keV/c (as discussed in Section 4.4). This is mostly from the uncertainties in transverse momentum components, including the 0.4 mm spatial resolution and the transverse momentum calibrations. The 0.4 mm spatial resolution corresponds to 6 keV/c momentum uncertainty instead of 5 keV/c, since the transverse displacement of the +1 photoions is decreased by 20% due to the sagging spectrometer mesh. Then the momentum uncertainty from the transverse momentum calibration is

$$\sqrt{\sigma_{556keV}^2 - 6^2} = 14(3)\ \text{keV/c}, \tag{5.13}$$

which is bigger than the 10 keV/c estimation in Section 5.5.3, since the magnetic field deflection was not corrected for in this momentum calibration.

In addition to the $E4$ transition by emitting a 556 keV photon, the $^{86\mathrm{m}}$Rb nucleus also has a probability to emit two photons [49]. This will make a recoil with a very broad momentum spectrum. However, this is very hard to distinguish from our smooth background.

5.8 Massive Particle Searches

Based on the momentum spectrum of Figure 5.17, we did a massive particle search by scanning over the recoiling momentum and fitting Gaussian profiles for potential peaks. Each Gaussian fit was done by floating the simulated background spectrum and fixing the Gaussian widths at the same as σ_{556keV}. The fixed centroids were scanned at a 5 keV/c step between 60 and 700 keV/c. The fitting range covered at each step is ± 100 keV/c. The data with momentum less than 60 keV/c was ignored, since it is dominated by the isomer events.

The reason for fixing the Gaussian width at σ_{556keV} is due to the fact that the momentum resolution is mostly from the spatial resolution of the ion detector, which is uniform across the plate and thus uniform for ions with any recoiling momentum. We also checked the momentum resolution for +1 ions with different recoiling momentum by SimIon simulations, which qualitatively showed that the momentum resolution is constant and not depending on the recoiling momentum for the +1 photoions.

5.8.1 Branching Ratios

After the scanning, the branching ratio for emitting a potential massive particle at each step was calculated by taking the ratio between A_{ith} (counts under the scanned peaks) and A_{556} (counts under the 556 keV/c peak). The results are shown in Figure 5.21 (a), which is a plot of the deduced branching ratio versus the $^{86\mathrm{g}}$Rb recoiling momentum p.

The physically allowed branching ratio is in the range of [0,1]. However, there are multiple points with negative branching ratios, as shown in Figure 5.21 (a). The reason for these physically unallowed branching ratios is the floating background during the Gaussian fit. To find physically meaningful upper limits for those points, a method using the Bayes's theorem of inverse probability [50] was applied. The main idea of this method is to assume a normal distribution centered at the negative branching ratio "-a" with a width of σ. Then the tail area above the 0 branching ratio will be normalized to unity. The new most probable value for the branching ratio is set at 0, and the new upper limit will be at the location "+b" where 68% area is covered between 0 and +b. The corrected branching ratios are shown as red color in the plot.

According to the momentum spectrum, our sensitivity to exotic particles is about 10%, which is not enough for detecting the exotic particles proposed in Chapter 1. The relatively high branching ratio at $p < 140$ keV/c comes from the tail of the isomer event peak, which is not totally eliminated by the isomer event cut. The peak at 556 keV/c with more than 2σ significance is from the known gamma-ray emissions.

Since the transition energy in the ^{86m}Rb isomeric transition is a constant of 556 keV, the recoiling momentum of ^{86g}Rb can be converted into the mass for potential exotic particles by $E = \sqrt{m^2c^4 + p^2c^2} = 556$ keV/c. The result is shown in Figure 5.21 (b), which is a plot of the branching ratio versus the mass of potential exotic particles. The events with $p > 556$ keV/c are excluded in the mass spectrum, since they correspond to negative masses by the conversion. Due to the 15 keV/c momentum resolution, our sensitivity gets worse for particles with masses less than 150 keV/c^2, since they can not be resolved from the gamma-ray peak. For m > 540 keV/c^2, the massive particles can not be resolved from the isomer photoions either.

5.8.2 Phase Space Probability

To search for a massive particle with mass m_0, the phase space density $p^2dp = pEdE/c^2$, since

$$\begin{aligned} E^2 &= m_0^2c^4 + p^2c^2, \\ E\,dE &= p\,c^2\,dp. \end{aligned} \tag{5.14}$$

When the transition energy is fixed as in our case, the probability of emitting a massive particle in phase space has to be integrated over E with a delta function $\delta(E - E_0)$,

$$\int pEdE/c^2 \times \delta(E - E_0) = pE_0/c^2, \tag{5.15}$$

which is linearly proportional to the recoiling momentum p.

As we discussed in Section 3.6.4, the photoionization probability R_g for the ^{86g}Rb recoils is proportional to their transit time τ_t in the 778 nm laser beam, which is inversely proportional to the recoiling momentum ($\tau_t \propto 1/p$). So $R_g \propto 1/p$, leaving no dependence on p for the sensitivity. However, the transit-time braodening produces a p dependence for the sensitivity since the two-photon transition rate is inverse proportional to the transition linewidth (see Equation 2.8), which is a convolution of the 5D$_{5/2}$ state natural linewidth and other broadening effects including the transit-time broadening. The transit-time dependence of the two-photon transition rate has been

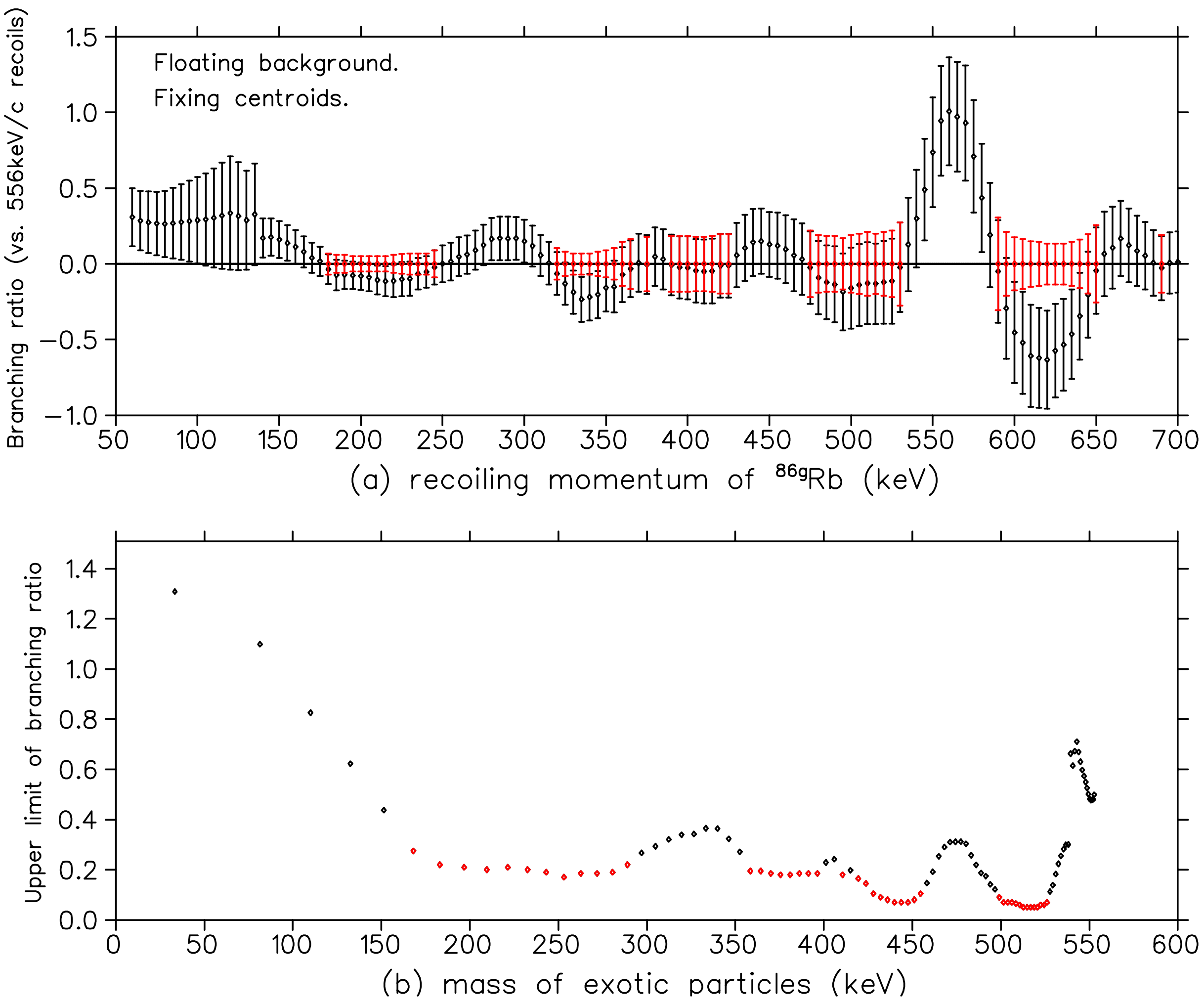

Figure 5.21: Branching ratios for emitting massive particle candidates, by calculating A_{ith}/A_{556}. The red points are the results of correcting the negative branching ratios using the Bayes's theorem of inverse probability [50]. The peak at 556 keV/c is from the known gamma-ray emissions. (a) branching ratios versus recoiling momentum of potential massive particles. The error bars are calculated using 1σ errors from the Gaussian fittings. (b) upper limit of the branching ratio versus masses of potential massive particles. Recoiling momentum p is converted to mass by $\sqrt{m^2c^4 + p^2c^2}$ = 556 keV.

taken into account during the branching ratio calculation, by normalizing the two-photon transition rate for Rb recoils at the lower recoiling momentum to the case at the 556 keV/c. As a result, the sensitivity at the lowermost momentum is improved by 30%.

5.9 Summary of The ^{86}Rb Experiment

To reconstruct the recoiling momentum of the decay daughter ^{86g}Rb, and thus search for exotic particle emissions in ^{86}Rb isomeric transitions, we measured the ion's TOF and hit positions on the MCP. The events we measured include photoions with charge state +1, and internal conversion events with high charge states (+3 to +10).

The maximum transverse displacement for the internal conversion events is 30% smaller than expected. The reason was found to be the sagging of the 40 mm spectrometer mesh. After adding a 4 mm spherical sagging of the spectrometer mesh, the inconsistency in transverse displacements was solved. However, the attempt to correct the magnetic field deflections with this sagging mesh failed, due to the dependance of the deflections on the details of the sagging geometry.

The momentum reconstructions were conducted for +1 photoions and +4 internal conversion events, by assuming a polynomial relationship between the ions' TOF/displacements and their longitudinal/transverse momenta. The momentum spectrum for the +1 photoions shows a peak around 562(3) keV/c, within 2σ of the nominal value of 556 keV/c. Since we ignored the trajectory deflections by the quadrupole magnetic field, the achieved momentum resolution is 15(3) keV/c, which is twice the estimation of 7 keV/c.

Although the number of collected photoion events is much lower than expected (explanation in Section 5.9.2), we still did the search for massive particles as a test. The resulting branching ratios are determined to be 10%, which is not sensitive enough for detecting the proposed exotic particles.

5.9.1 Atomic State of ^{86}Rb After The Isomer Decay

To figure out the atom's electronic states after gamma decay, we adopted a sudden approximation model that was applied to shakeoff electrons from beta decay [51].

The probability of finding an electron (originally in orbital ψ_i of a nucleus of charge Z) in orbital ψ_f of charge $Z + \Delta Z$ is

$$P_{if}(\vec{k}_r) = | < \psi_i | e^{-i\vec{k}_r \cdot \vec{x}} | \psi_f > |^2, \tag{5.16}$$

the transition matrix element involves a plane wave for the electron (in the rest frame of the atom), treated as an operator between the initial and final state wavefunctions. Expanding $P_{if}(\vec{k}_r)$ to first order in $\vec{k}_r \cdot \vec{x}$ gives

$$P_{if}(\vec{k}_r) \simeq | < \psi_i | \psi_f > |^2 + |\vec{k}_r|^2 | < \psi_i | \hat{k}_r \cdot \vec{x} | \psi_f > |^2, \tag{5.17}$$

where $\hat{k} = \vec{k}/|k|$. The first term in the expansion of the plane wave is just an overlap between the initial and final atomic states. This term is nonzero in beta decay because the nuclear charge has changed and different atoms are involved, but in internal conversions the initial and final states are both in the same Rb atom and they are orthogonal to each other, so this term vanishes.

The next term can be related to the dipole strength function, and simply using the dipole sum rule shows that it is about 10^{-5} in probability. Almost all of this goes to the first excited p state of the alkali atom [52], which immediately decays to the ground state again in tens of nanoseconds.

So, after gamma decay, most ^{86}Rb atoms are still in the atomic ground state, instead of the metastable excited states which could make them blind to the 778 nm light. We also note that even if the atoms were in the metastable states, most such states would still be ionized by the 1064 nm laser, which was on all the time in the experiment.

5.9.2 Low Event Rate

Both the absolute photoionization event rate and the event ratio between the isomers and the daughters are inconsistent with our estimation.

In the ^{86}Rb experiment, the total data-taking time for searching for exotic particles was about 8 hours, and we collected about 5.3×10^4 isomer events (before the ion MCP pulse height cut). However, the expected isomer events is 2.8×10^7 for $R_{86m} = 1$ kHz, which is 500x more than the collected events. We also tested the ^{85}Rb photoionization rate offline, and the rate is 50x lower than expected. There are a lot of factors that could affect the absolute isomer event rate, such as the alignment and stability of the 778 nm and 1064 nm light, the overlap between the photoionization laser beams and the trap cloud.

As estimated in Section 3.6.5, the photoionization rate of the isomers should be 40x the fast-moving decay daughters, even when the 778 nm two-photon transition light is 1645 MHz off resonance. Since we collected about 40,000 isomer events (after the MCP pulse height cut), the number of the daughter events should be around 1000. However, the 556 keV/c peak shown in Figure 5.17 only includes 150 daughter events, which is 6x less than expected. There are two main factors affecting the daughter event rate. First, the 778 nm light was not always on resonance for the decay daughters, since we scanned the 778 nm light in the MHz range to search for better daughter signals in some runs. Secondly, the sagging effect on the spectrometer mesh decreases the momentum resolution by a factor of 2, which smeared the 556 keV/c peak and decreased the number of daughter events. Moreover, the hyperfine structures of the transition matrix element was ignored in the two-photon transition rate estimation, which could also affect the event ratio by a small factor.

In summary, the absolute event rate is much lower than expected, due to the imperfect experimental setup for two-photon transitions. However, the event ratio between the isomers and the decay daughters would be consistent if the spectrometer mesh was not sagged and the 778 nm light was locked to the two-photon resonance frequency all the time.

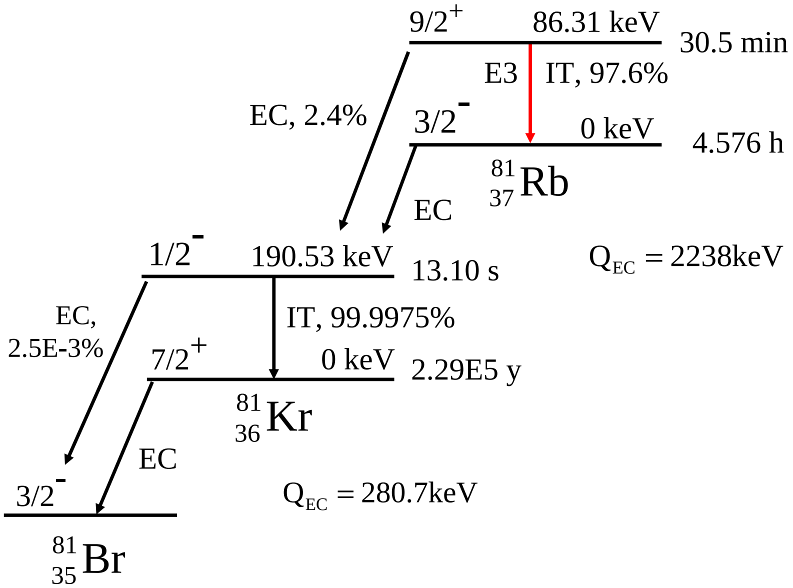

Figure 5.22: ^{81}Rb isomeric transitions.

5.10 The ^{81}Rb Test

5.10.1 Motivations

Because of the difficulties in photoionizing ^{86g}Rb, we switched to ^{81m}Rb isomer decay, which has a 86.3 keV transition energy and is sensitive to 40 – 80 keV/c^2 masses, as shown in Figure 5.22.

The recoiling momentum of ^{81g}Rb is 6.4x smaller than ^{86g}Rb, resulting in a 6.4x longer transit time crossing the laser beam. Based on the discussions shown in section 3.6.4, the two-photon transition efficiency is about quadratically proportional to the transit time, so the photoionization rate for ^{81g}Rb could be increased by 41x.

With the demonstrated TRINAT count rates for ^{86m}Rb, and taking into consideration of the decay lifetime difference and one order of magnitude higher production rate for ^{81m}Rb, we expected to collect 2×10^5 ^{81g}Rb events in 4 shifts beam time. Even assuming no further signal/noise improvements and no power buildup cavity for the 778 nm light, this could have allowed sensitivity to 2.5×10^{-4} branch at 90% confidence, to search for 0^+ particles within the 40 – 80 keV/c^2 mass range.

5.10.2 Radioactive Background

The test for exotic particle searches in ^{81m}Rb isomer decay failed, due to the unforeseen high background rate. The background rate was many kHz in both microchannel plates after a number of hours of accumulation of the ground state ^{81}Rb background. (The two-photon spectroscopy of

Chapter 6 was then done very quickly after letting the background decay for many hours.) Some small progress was made with shielding external to the chamber, but about 2 kHz turned out to be true coincidences between the ion and electron MCP's, not accidental coincidences. These nuclei undergo electron capture decay with a 4.6-hours half lifetime. This makes many energetic Auger electrons and X-rays, most of which are barely perturbed by the modest electric fields of the spectrometer. So the background must have come from ^{81g}Rb atoms sticking to the walls of the second chamber or the electrodes, with ions triggering the ion MCP in coincidence with other radiation triggering the electron MCP. The TOF spectra with trap off had complex structures that were roughly consistent with such a background.

It became clear that this spectrometer design would not work on an isotope whose ground state has a long-lived electron capture decay. TRINAT spectrometers for beta decay in the past have been designed to completely exclude backgrounds from the walls, but this is relatively straighforward for low-multiplicity decays with low-energy ion recoils. This exclusivity was compromised in the present geometry in favor of momentum resolution.

Any future experiments would involve power buildup cavities for ^{86m}Rb decay, where the ground state is a β^- decay with much smaller backgrounds. Electron capture of the 1% EC branch was cleanly identified in the past in ^{80}Rb decay by TOF cuts [53] and production of high charge states. Electron capture decay makes 2-body final states from monoenergetic neutrinos, which by similar kinematics to the exotic massive particles would allow a search for weakly coupled neutrinos with masses of 100 keV/c^2. However, given the long lifetimes of isotopes with large EC branches, it is clear that a completely different spectrometer design would be needed to exclude such backgrounds.

5.11 Power Buildup Cavity Test

5.11.1 Motivations

As discussed in Section 5.9.2, the exotic particle search experiment is limited by the photoionization rate. To achieve the proposed sensitivity in a limited beamtime, more power for the 778 nm light is necessary. A power buildup cavity is the best choice for this purpose without upgrading the laser itself. The MBR laser output has a very good linear polarization and a narrow linewidth of about 300 kHz, which are critical for coupling laser power into the cavity.

A power buildup cavity naturally guarantees a perfect alignment for the 778 nm light when the cavity is locked, and could increase the 778 nm light intensity in a standing wave by orders of magnitude if the cavity is properly designed. Moreover, the 778 nm light itself also ionizes atoms from the 5D$_{5/2}$ state, so the 1064 nm light was removed to simplify the optical setups.

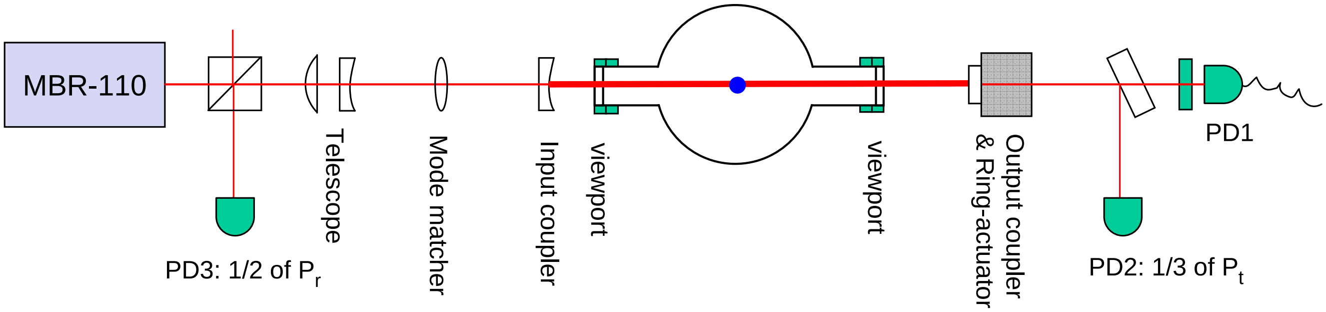

Figure 5.23: Experimental setup of the power buildup cavity.

5.11.2 Experimental Setup

The experimental setup for testing the power buildup cavity is shown in Figure 5.23, and the information of the parts used is summarized in Table 5.1.

The cavity is a plano-concave resonator, which is built outside the collection chamber with two vacuum viewports sandwiched between the input and output couplers. The reason for not building the cavity inside the vacuum is that, the original optical setup (as shown in Figure 3.4) for the exotic particle search experiment did not include a design of the power buildup cavity. In addition, the collection chamber coexisted with the TRINAT $\beta-\nu$ correlation experiment, which was not designed for holding a cavity inside the vacuum.

The input coupler is a $1/2''$ plano-concave mirror with "-2 m" radius of curvature and 98(1)% power reflectivity (R_1), which was mounted on a two-dimensional translation stage. The output coupler is a $1/2''$ plano mirror with 99.5% power reflectivity (R_2), mounted on a ring actuator. The ring actuator modulates the cavity length and also allows the transmitted power to pass through it. Both assemblies of the input and output couplers are mounted on a $1.5''$ diameter damping post to constrain the cavity length and reduce fluctuations. The $1.5''$ damping post is parallel to the 778 nm light crossing the detection chamber and also at 30° angle relative to the horizontal plane.

Three photodiodes were used in the setup, PD1, PD2 and PD3. The photodiode PD3 monitors half of the reflected power from the input coupler, $P_3 = P_r/2$. It can be used to deduce the power coupled into the cavity, $P_{coupled} = P_0/2 - 2P_3$, where $P_0 = 0.58$ Watts is the total power output of the MBR laser. The transmitted power P_t through the output coupler is split into two branches. One branch is sent to the photodiode PD2, which measures 1/3 of the transmitted power, $P_2 = 1/3P_t$. The other branch is sent to the photodiode PD1 and then amplified for locking the cavity length to be on resonance with the 778 nm light. Since the power transmission rate of

Name	Company	Part No.	Specifications
Input coupler	CVI	PR1-780-98-0537	plano-concave, $R_1 = 98(1)\%$, f = -1 m, ø = 1/2″, 3/8″ thick
Output coupler	CVI	TLM1-750-0-0512	flat, $R_2 = 99.5\%$, ø = 1/2″
Viewport		VPZ38BBAR	$T_3 = 99.8\%$
Telescope lens	NEWPORT	KPC040AR.16	lens with f = -50 mm, ø = 1″
Telescope lens	NEWPORT	KPX100AR.16	lens with f = 150 mm, ø = 1″
Mode matcher	NEWPORT	KPX100AR.16	lens with f = 150 mm, ø = 1″
Ring actuator	Piezomechanik	150/14-10/12 VS 22	$12\mu m/150V$ stroke, $f_0 = 20$ kHz, 300N/μm stiffness

Table 5.1: Components used for building the power buildup cavity of the 778 nm light. R_1 and R_2 are the power reflectivity for the input and output couplers, respectively. T_3 is the power transmission rate for the vacuum viewport.

the output coupler is 0.5%, the circulating power inside the cavity is

$$P_{circ} = \frac{3P_2}{0.5\%} = 600P_2, \tag{5.18}$$

and the power buildup ratio is

$$B = \frac{P_{circ}}{P_0/2} = \frac{1200P_2}{P_0}, \text{ or } B = \frac{400P_r}{P_0}. \tag{5.19}$$

5.11.3 Mode Matching

The 778 nm light from the MBR-110 laser is a Gaussian beam in a TEM00 mode, and the quality of the Gaussian fit is 93% at the beam waist [54]. The Gaussian beam diverges during traveling. To match the wavefront of the 778 nm light with the cavity's spatial mode, a telescope and a weak focusing lens are used in front of the input coupler, as shown in Figure 5.23.

The spatial mode [37] of the plano-concave resonator requires that the Gaussian beam waist should be located at the flat output coupler. The wavefront curvature $R(L)$ of the Gaussian beam after traveling one cavity length $L = 0.55$ m, $R(L) = L + z_0^2/L$, must match with the curvature of the input coupler. For the 778 nm light with 0.5 mm beam waist radius, the Rayleigh range $z_0 = \pi w_0^2/\lambda \simeq 1$ m. So the curvature of the input coupler is determined as $R_1 \simeq -2.5$ m. A detailed Gaussian beam simulation using the ABCD law [37] suggested a more appropriate value of $R_1 = -2$ m, and the resulting beam size simulation in the cavity is shown in Figure 5.24, which

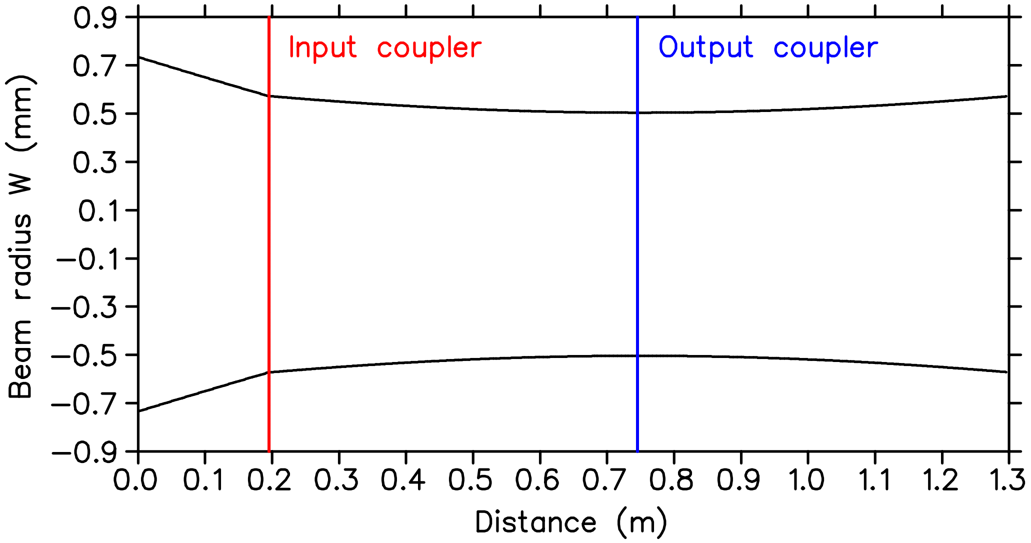

Figure 5.24: Beam size simulation by WinLASE 2.1. The red and blue marks are the positions for the input coupler and the output coupler, respectively. The output coupler is located at the beam waist, and the curvature of the input coupler matches with the spatial mode of the plano-concave resonator.

clearly shows that the 778 nm beam matches with the spatial mode of the plano-concave resonator.

The plano-concave resonator also satisfies the stability condition for ray confinement [37], $0 \leq g_1 g_2 \leq 1$, where $g_i = 1 + d/R_i$. Since $d \simeq 0.55$ m, and the radius of curvature for the mirrors is $R_1 = -2$ m and $R_2 = \infty$, then

$$\begin{aligned} g_1 &= 1 + d/R_1 = 0.73, \\ g_2 &= 1 + d/R_2 = 1, \text{and} \\ g_1 g_2 &= 0.73 \ \leq 1. \end{aligned}$$

5.11.4 Expected Power Buildup Ratio

Based on the mode matching requirements, we determined the curvature of the input coupler, but not the reflectivity. To figure out the optimal value for the input coupler reflectivity and estimate the power buildup ratio of the plano-concave resonator, we made a plot to examine the dependence of the power buildup ratio and finesse on the input coupler reflectivity R_1, according to Equation 2.14 and 2.17.

The plot is shown in Figure 5.25, in which the power reflectivity of the output coupler R_2 is set at 99.5% and the power loss R_3 on the vacuum viewports is combined with R_2 by $R_2' = R_2(1 - R_3)^4 = R_2 T_3^4 \simeq 98.7\%$, since the 778 nm light passes through the viewport surface 4 times

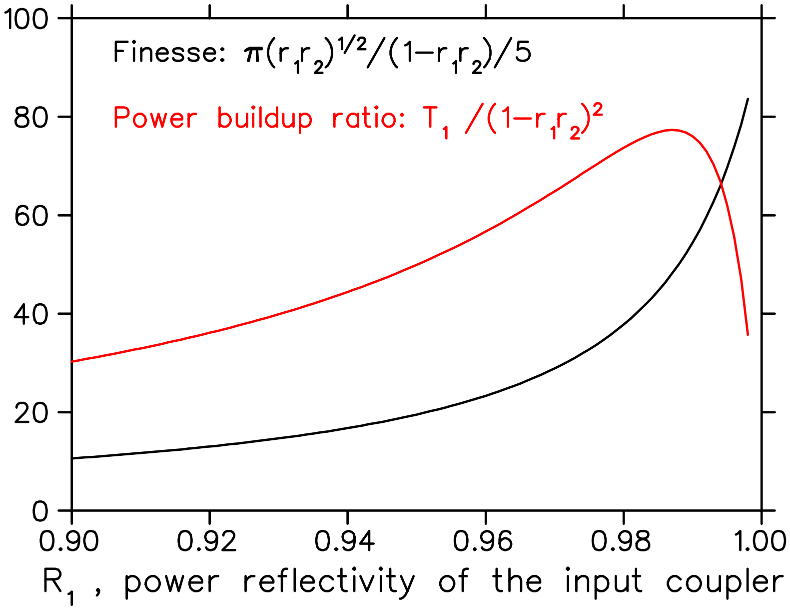

Figure 5.25: Dependence of power buildup ratio and finesse on R_1. The power loss on the vacuum viewport is considered by combining the power reflectivity of the output coupler with the power transmission of the vacuum viewport, $R_2' = R_2 T_3^4 \simeq 98.7\%$.

per path.

The maximum buildup ratio is around $R_1 = 98.5\%$, which matches with the 98(1)% power reflectivity of the chosen input coupler. So the expected power buildup ratio and finesse are $B = 71(6)$ and $F = 210(64)$, respectively.

5.11.5 Table Test

Before assembling the power buildup cavity on the experimental chamber, we did a test on an optical table. The experimental setup for the table test is almost the same as the chamber test, except that the $\o = 1.5''$ post is mounted horizontally above the optical table without the 30° tilting angle.

The measured transmission spectrum is shown in Figure 5.26, as well as the sweeping voltage on the ring actuator. The main mode is shown around $\Delta L = 0.1\ \mu m$, which was fitted by a sum of two Lorenztian profiles. Based on the linewidth of the main mode, $\Gamma = 0.0053\ \mu m$, the cavity finesse is estimated to be $F = \lambda/(2\Gamma) \simeq 74$, which is about 2σ away from the expected value of 210(64).

We did not measure transmission power and reflection power for the cavity in the table test, thus no direct way to determine the power buildup ratio here. An estimation can be made to be $B = 40$, based on the measured finesse and the theoretical curves in Figure 5.25.

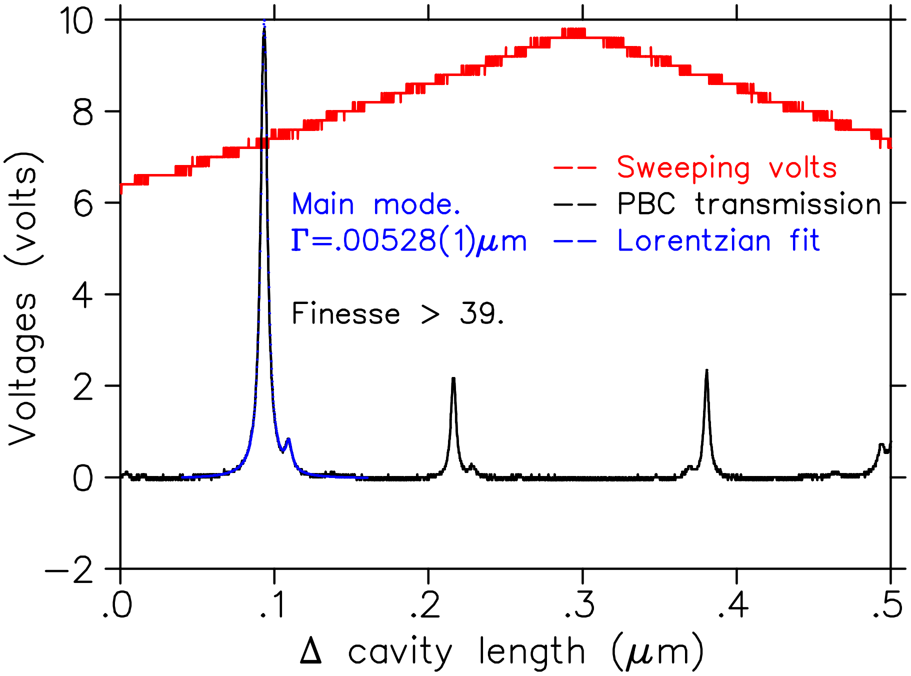

Figure 5.26: Transmission spectrum of the power buildup cavity for the table test. The transmitted power (with arbitrary units) is scaled up by a factor of 12 so that it is at the same scale as the sweeping voltage. The main mode was fitted by a sum of two Lorentzian profiles, and the cavity finesse is estimated to be ∼ 74.

5.11.6 Chamber Test

The chamber test was done using the experimental setup shown in Figure 5.23, with the cavity mirrors mounted on a 30° tilted damping post. The transmission spectrum is shown in Figure 5.27, which includes one full free-spectrum range, and the finesse is determined as 36(10).

Based on the measured finesse and the theoretical curves in Figure 5.25, the power buildup ratio would be estimated to be 21(5). However, the real power buildup ratio is much less. The measured transmission power through the output coupler is $P_t \simeq 1.2$ mW, then the power buildup ratio is $B = 400 \times 1.2/580 \simeq 1$, according to Equation 5.19. The power coupled into the cavity is also deduced by the measuring P_r. The result is 20%, comparing with 70% power coupled during the table test. According to the transition rate estimation in Section 3.6, the 1 fold power buildup for the 0.29 Watts power will not saturate the two-photon transitions for the trapped Rb atoms, and the two-photon saturation intensity would require a power buildup ratio of $B > 3$.

To verify whether the two-photon transitions are saturated or not by the power buildup cavity, we also measured the photoionization rate during the chamber test. This was done by measuring the production rate of Rb photoions, while locking the cavity transmission at different side points of the main mode and thus changing the circulating power inside the cavity. The relationship between the photoionization rate R_{ion} and the circulating poewr P_{circ} is shown in Figure 5.28,

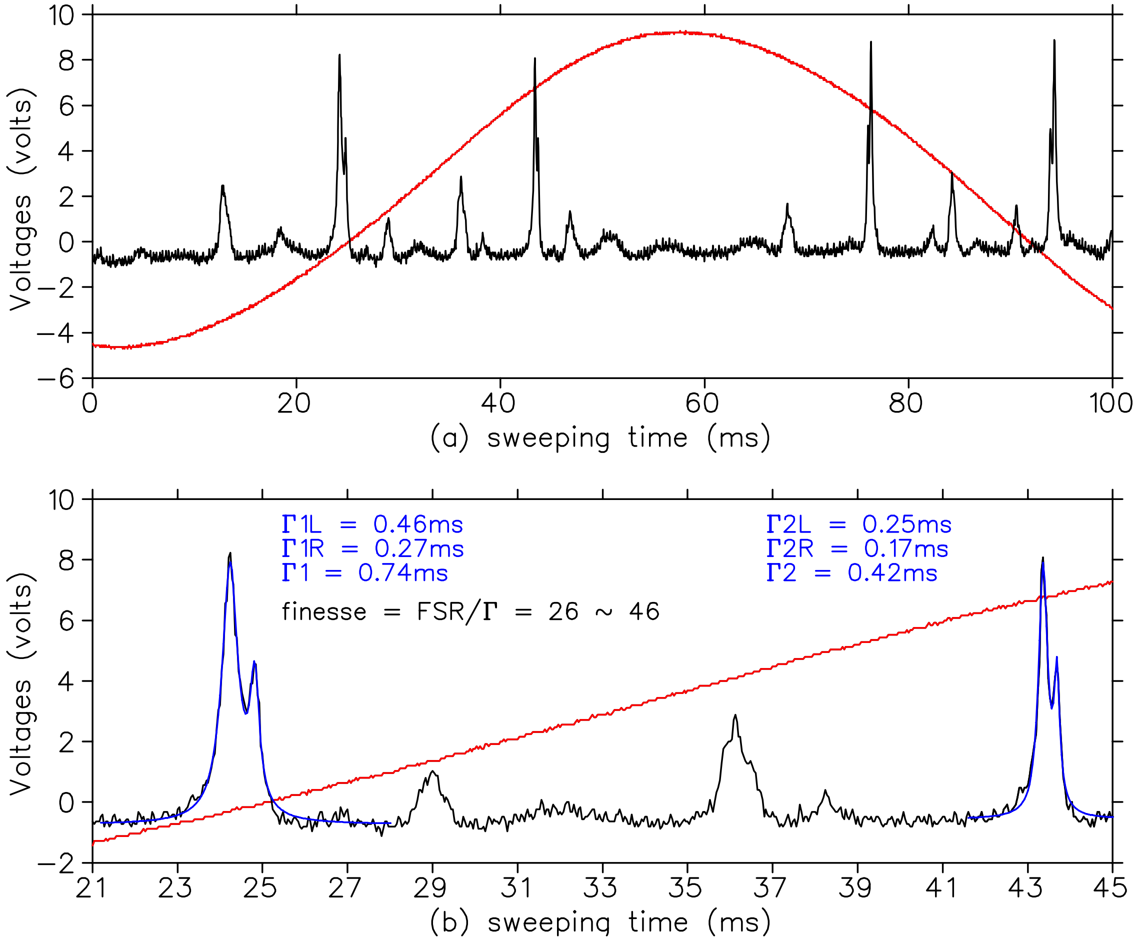

Figure 5.27: Transmission spectrum of the power buildup cavity for the chamber test. The transmitted power was scaled by a factor of 40 to be on the same scale as the sweeping voltage. The main mode was fitted by Lorentian profiles, and the finesse of the cavity was estimated to be 26 – 46.

which was fitted by a power law,

$$R_{ion} = a \times (P_{circ})^i, \tag{5.20}$$

and i was found to be 3.5(2).

According to the two-photon transition theory (see Section 2.2), the two-photon transition rate $R^{(2)}$ is quadratically proportional to the light intensity I when the light polarization is linear and the two-photon transitions are not saturated. The resulting photoionization rate, $R_{ion} = R^{(2)} \times I \propto I^3$. If the two-photon transition rate is saturated, $R_{ion} \propto I$ only. Our measurement of $i = 3.5(2)$ verifies that the circulating power in the cavity did not saturate the two-photon transitions.

The reason for the low power buildup ratio in chamber test is due to several factors, such as the unanticipated loss in the vacuum or on the vacuum windows, the spatial mode distortion by the stress-induced phase shifts from the vacuum viewports, as well as the vibrations and the difficulties

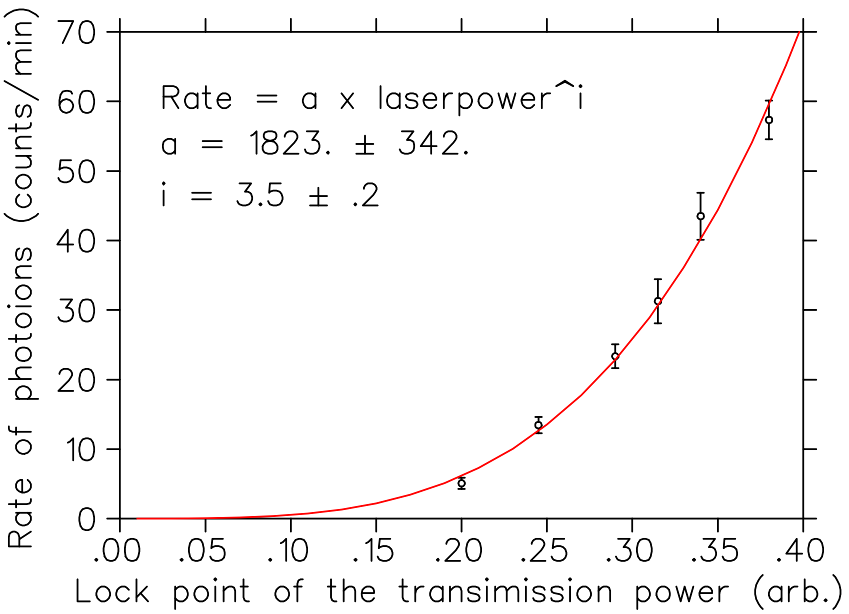

Figure 5.28: Photoion rates versus MBR laser power.

in optics tunings. As shown in the transmission curve, the power coupled into the main mode is only 60% and the high order mode shares more than 40%. In contrast, more than 95% power is coupled into the main mode in the table test, and the high order mode is mostly suppressed.

5.11.7 Summary of The Power Buildup Cavity Test

To solve the low photoionization rate problem in the ^{86}Rb experiment, we tested the power buildup cavity for the 778 nm light. Although the cavity performance was good in the table test, the measured power buildup ratio in the chamber test is only 1x, which suggests that adding a power buildup cavity onto the current experimental setup will not solve the low photoionization rate problem.

Building a new cavity with enough power buildup ratio to saturate the two-photon transitions and make enough photoions for the exotic particle search experiment would require to design a new collection chamber, so that the cavity could be better stabilized.

5.12 Conclusion and Feasibility Discussion of The Exotic Particle Search Experiment

If the new cavity solves the 500x lower isomer event rate problem (see Section 5.9.2), we would expect to collect $150 \times 500 \times (120h/8h) = 1.1 \times 10^6$ $^{86\text{g}}$Rb daughter events in 10 shifts beam time, assuming the same experimental conditions as the run in April 2009.

According to the discussion in Section 5.8.2, our sensitivity to massive particle emissions is independent of the ^{86g}Rb recoiling momentum. Then the sensitivity estimation can be done based on the experimental background around 556 keV/c, which should be about 1000 counts in 10 shifts beam time. The 5σ significance for searching a massive particle signal requires 160 counts above the background. This corresponds to a sensitivity of 1.4×10^{-4}, comparing with the proposed 10^{-6} sensitivity.

The expected sensitivity level can be improved by several factors. The first factor is fixing the sagging spectrometer mesh. This would greatly improve the momentum calibration and reduce the momentum resolution from 15(3) keV/c to the designed 7 keV/c, and the current 6x lower event ratio between the daughter events and the isomer events might be fixed as well. The second factor is lowering the background rate by better-designed Gamma ray shieldings. During the ^{86}Rb experiment, the Gamma background was reduced from 700 Hz to 300 Hz, by adding a piece of half letter-size lead with $1/2''$ thickness between the beamline and the ion detector. This could be further reduced by better-designed shielding using hevimet (high-density Tungsten alloy). The hevimet shielding was implemented in the ^{81}Rb experiment; however, we could not estimate the shielding efficiency since the background rate in the ^{81}Rb experiment was much higher than in the ^{86}Rb experiment.

Accomplishing the above two factors might improve the current sensitivity to the 10^{-5} level, but this is still one order of magnitude higher than the proposed sensitivity of 10^{-6}. The low event rate problem for ^{86g}Rb decay daughters cannot be solved by simply increasing the power of the photoionization lasers, since the isomers will be overkilled by the enhanced laser power and the production rate for the daughters will decrease accordingly. In order to achieve the proposed 10^{-6} sensitivity, a better photoionization scheme must be invented to enhance more on the photoionization rate of the fast-moving daughters but less on the trapped isomers.

Chapter 6

Doppler-free Two-photon Spectroscopy in Rb Isotopes

In this chapter I will summarize the results of the Doppler-free two-photon spectroscopy measurements between the $5S_{1/2}$ and $5D_{5/2}$ states in radioactive Rb isotopes, which has been been published in [55].

First I will explain the slightly different experimental setup comparing with the exotic particle search experiment. Then I will show the Doppler-free two-photon transition spectra for three Rb isotopes, ^{86m}Rb, ^{86g}Rb and ^{81g}Rb. By fitting Voigt profiles to the two-photon spectra, we extracted the related isotope shifts and hyperfine constants of the $5D_{5/2}$ state, and investigated the systematic errors. At the end of this Chapter, I will summarize the specific mass shift analysis for the $5S_{1/2}$ to $5D_{5/2}$ two-photon transition, based on the isotope shift results we measured.

6.1 Experimental Setup

There is little difference between the two-photon spectroscopy experiment and the exotic particle search experiment. In the two-photon spectroscopy measurement, the high power 1064 nm light was removed to avoid photoionizing all the atoms before reaching the two-photon resonances, and the photoionization scheme using the 778 nm light is the same as the one shown in Figure 3.3 (a).

The experimental setups for the $5S_{1/2}$ to $5D_{5/2}$ Doppler-free two-photon spectroscopy are shown in Figure 6.1 and 6.2, which are for the ^{86}Rb and ^{81g}Rb measurements, respectively. Although there are three versions of the setups, they are quite similar and only differed by the AOM schemes. In general, each setup can be separated into two parts: a frequency locking part of the MBR laser and a photo-ionization part of the radioactive isotopes.

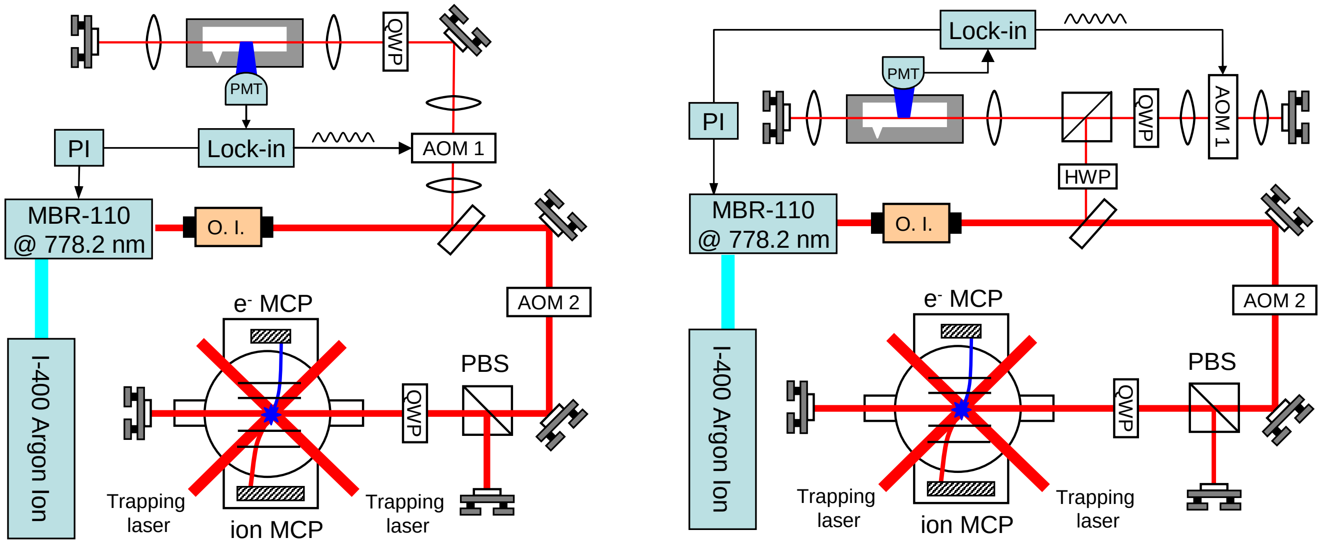

(a) single-pass AOM setup (b) double-pass AOM setup

Figure 6.1: Experimental setup of Doppler-free two-photon photo-ionization of trapped ^{86}Rb atoms. (a) single-pass setup of AOM 1, (b) double-pass setup of AOM 1. AOM 2 was fixed at +80 MHz, and the 1st-order diffracted beam was sent to the experimental chamber. The optical isolator (O.I.) was needed to protect the MBR-110 laser from optical feedback. QWP and HWP are quarter waveplate and half waveplate, respectively.

6.1.1 Vapor Cell Reference

The frequency locking part is done by locking the MBR laser frequency to the two-photon transitions of stable Rb isotopes in a vapor cell. The 778 nm light from the MBR laser is linearly polarized at the laser output. A quarter wave plate is placed in front of the vapor cell to convert the light to circular polarization (σ^+ for both directions). The use of $\sigma^+\sigma^+$ light makes the phototube signal larger [46] and allows us to lock to weaker transitions that are closer to the radioactive Rb isotopes. Both this and the high-intensity focused beam are not ideal for frequency references, so we carefully tested possible offsets and discussed them in Section 6.3.2.

In this experiment, three Rb isotopes were investigated using Doppler-free two-photon spectroscopy, ^{86g}Rb (nuclear spin I = 2), ^{86m}Rb (I = 6) and ^{81g}Rb (I = 3/2). The two-photon transition frequency offsets between these radioactive Rb isotopes and the stable Rb references are dominated by the hyperfine splittings of the $5S_{1/2}$ state, plus the isotope shift and hyperfine splittings of the $5D_{5/2}$ state. Figure 3.3 (b) shows the $5S_{1/2}$ state hyperfine structures for the involved Rb isotopes, which helps determine convenient reference transitions for locking the two-photon transition laser frequency:

^{87}Rb $5S_{1/2}$ F = 2 to $5D_{5/2}$ F = 4 as the reference for ^{81g}Rb F = 2 to $5D_{5/2}$ transitions;

^{85}Rb $5S_{1/2}$ F = 2 to $5D_{5/2}$ F = 4 as the reference for ^{86g}Rb F = 5/2 to $5D_{5/2}$ transitions;

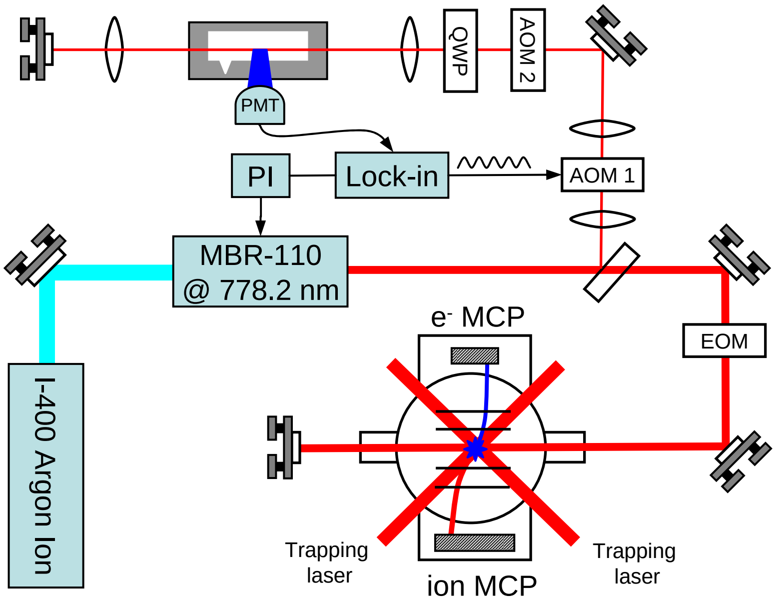

Figure 6.2: Experimental setup of Doppler-free two-photon photo-ionization for trapped ^{81g}Rb atoms. The modulation frequency of AOM 2 was fixed at +60/+70 MHz, and AOM 1 was scanned at 100 – 130 MHz.

^{85}Rb 5S$_{1/2}$ F = 2 to 5D$_{5/2}$ F = 4 as the reference for ^{86m}Rb F = 11/2 to 5D$_{5/2}$ transitions;
^{85}Rb 5S$_{1/2}$ F = 3 to 5D$_{5/2}$ F = 5 as the reference for ^{86m}Rb F = 13/2 to 5D$_{5/2}$ transitions.

6.1.2 AOM Schemes

According to the isotope shift estimations using the experimental values of the Rb D2 transition [30], the two-photon transition frequency offsets between the stable Rb reference and the radioactive Rb isotopes under investigation could be up to hundreds of MHz. This has to be compensated since the linewidth of the 5S$_{1/2}$ to 5D$_{5/2}$ transition is only about 1 MHz.

AOMs (acousto-optic modulators) are good candidates for this purpose, because they are fast (μs switching speed) and accurate enough (kHz resolution) for the precision involved in the two-photon spectroscopy measurement. In addition, the power damage threshold of AOMs is much higher than the MBR laser intensity. The only limitation is the maximum modulation frequency which ranges from tens to hundreds of MHz, so different AOM schemes have to be used depending on the frequency offsets. Details of the AOM schemes for all three measurements are explained in Section 6.2.2 – 6.2.4 and summarized in Table 6.1.

For the convenience of description, we define the MBR laser frequency in the vapor cell as f_{cell}, and in the trap as f_{trap}. The two-photon resonance frequency in the trap can be found by scanning f_{AOM1}, while keeping f_{cell} locked to the resonance frequency of the stable Rb species in the vapor cell. Scanning f_{AOM1} does change the alignment in the vapor cell and decrease the phototube

	^{86g}Rb	^{86m}Rb	^{86m}Rb	^{81g}Rb
Spectrum	F = 5/2 to $5D_{5/2}$	F = 11/2 to $5D_{5/2}$	F = 13/2 to $5D_{5/2}$	F = 2 to $5D_{5/2}$
f_{trap} (in MHz)	735 – 760	945 – 965	-890 – -870	-1250 – -1220
AOM 1 setup	double pass	single pass	double pass	single pass
f_{AOM1} (in MHz)	62 – 74	60 – 84	114 – 127	-105 – -135
f_{AOM2} (in MHz)	+80	+80	+80	+60/+70
Ref. isotope	^{85}Rb	^{85}Rb	^{85}Rb	^{87}Rb
Ref. transition	F = 2 to 4	F = 2 to 4	F = 3 to 5	F = 2 to 4
f_{cell} (in MHz)	803.258	803.258	-719.333	-1295.333

Table 6.1: Summary of the AOM schemes in the Doppler-free two-photon spectroscopy experiments, all frequencies are in MHz. The spectrum is referred to the transitions between a hyperfine level of the $5S_{1/2}$ state to all allowed hyperfine levels in the $5D_{5/2}$ state, and f_{trap} is the corresponding transition frequency ranges relative to the ^{87}Rb COG. f_{cell} is the MBR laser frequency in the vapor cell, which was locked to the reference two-photon transitions ($5S_{1/2}$ state to $5D_{5/2}$ state) of stable Rb species.

signal, even after the deflection minimization by sandwiching AOM 1 with focusing lenses and positioning AOM 1 at the focal point; however, we only need to scan f_{AOM1} over a small range (10 – 30 MHz) to go through most of the $5D_{5/2}$ hyperfine sublevels in all three Rb isotopes. In this case, the phototube signal remains strong enough for locking purposes during the f_{AOM1} scan.

In the ^{86}Rb experiments, AOM 2 was placed between the beamsampler and the trap. This arrangement allowed us to quickly turn on/off the MBR laser beam in the trap. The modulation frequency of AOM 2 was fixed at +80 MHz to avoid misalignment between the MBR laser beam and the trap cloud.

6.2 Doppler-free Two-photon Transition Spectra

We measured the $5S_{1/2}$ to $5D_{5/2}$ two-photon transition spectra for three Rb isotopes, ^{86g}Rb, ^{86m}Rb and ^{81g}Rb, by monitoring the number of photoelectrons. The spectra are shown in Figure 6.3 - 6.6 respectively, where the x axes are f_{trap}, the frequency offsets of the measured transitions relative to the ^{87}Rb $5S_{1/2}$ to $5D_{5/2}$ two-photon transition COG (center of gravity).

6.2.1 Voigt Profile

Although the atoms are cold and the Doppler-broadened background is minimized in our spectra, there are other effects that broaden the line, such as the MOT magnetic quadrupole field which was not turned off in the experiment (discussed in Section 6.3.3). So we used Voigt functions, a convolution of Lorentzian and Gaussian profiles, to fit the spectra.

	D_2 (MHz)	D_5 (MHz)
$\delta\nu^{86m,87}$	-32.1(2.3) [30]	-69.62(4)(19)
$\delta\nu^{86g,87}$	-45.8(2.0) [30]	-83.64(3)(21)
$\delta\nu^{85,87}$	-78.095(12) [56]	-160.627(6) [57]
$\delta\nu^{81g,87}$	-289.9(1.4) [30]	-552.40(28)(29)

Table 6.2: Isotope shifts between Rb isotopes and ^{87}Rb. The D_2 transition is from state $5S_{1/2}$ to $5P_{3/2}$; the D_5 transition is defined as the $5S_{1/2}$ to $5D_{5/2}$ transition. We measured $\delta\nu^{86m,87}$, $\delta\nu^{86g,87}$ and $\delta\nu^{81g,87}$ for the D_5 transition, and the errors are shown as (statistics)(systematics) and are summed quadratically for making the King plot.

	$A(5D_{5/2})$	$B(5D_{5/2})$
$^{86\mathrm{m}}$Rb	-1.2456(35)(115)	4.80(13)(9)
$^{86\mathrm{g}}$Rb	3.4320(67)(163)	1.76(8)(13)
$^{81\mathrm{g}}$Rb	-5.71(12)(4)	4.13(1.65)(31)

Table 6.3: Hyperfine constants (in MHz) of the $5D_{5/2}$ state for three Rb isotopes, $^{86\mathrm{m}}$Rb, $^{86\mathrm{g}}$Rb and $^{81\mathrm{g}}$Rb, as measured by the Doppler-free two-photon transition between the $5S_{1/2}$ and $5D_{5/2}$ states.

$$V(x;\sigma,\gamma) = \int_{-\infty}^{\infty} G(x';\sigma)L(x-x';\gamma)dx', \tag{6.1}$$

where x is the frequency from line center, $G(x;s)$ is the centered Gaussian profile:

$$G(x;\sigma) = \frac{e^{-x^2/(2\sigma^2)}}{\sigma\sqrt{2\pi}}, \tag{6.2}$$

and $L(x;\gamma)$ is the centered Lorentzian profile:

$$L(x;\gamma) = \frac{\gamma}{\pi(x^2+\gamma^2)} \tag{6.3}$$

We extracted isotope shifts for the $5S_{1/2}$ to $5D_{5/2}$ transitions and the hyperfine constants for the $5D_{5/2}$ states. The results are shown in Table 6.2 and Table 6.3, respectively.

6.2.2 $^{86\mathrm{g}}$Rb Measurement

The experimental setup for the $^{86\mathrm{g}}$Rb measurement is shown in Figure 6.1 (b), which includes a double-pass setup for AOM 1, and the relationship between f_{trap} and f_{cell} is

$$f_{trap} = f_{cell} + f_{AOM2} - 2 \times f_{AOM1}. \tag{6.4}$$

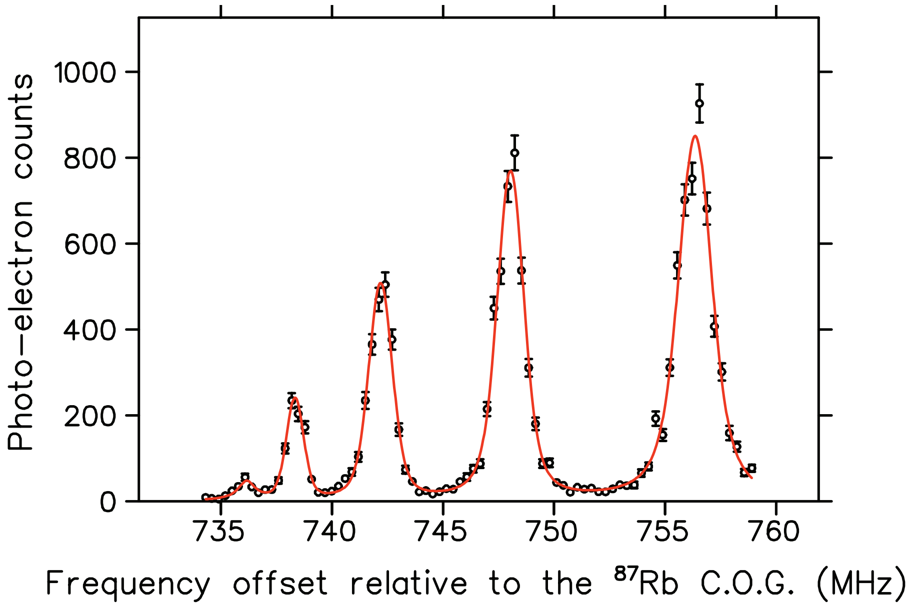

Figure 6.3: Hyperfine spectrum of the ^{86g}Rb 5D$_{5/2}$ state, measured by Doppler-free two-photon transitions between the 5S$_{1/2}$ F = 5/2 state and the 5D$_{5/2}$ F = 1/2 ... 9/2 states (lower ν to higher ν).

f_{cell} was locked to the ^{85}Rb F = 2 to 4 (5S$_{1/2}$ state to 5D$_{5/2}$ state) transition, which has a frequency offset of 803.258 MHz [57] relative to the ^{87}Rb 5S$_{1/2}$ to 5D$_{5/2}$ transition COG. f_{AOM2} was fixed at +80 MHz, and f_{AOM1} was scanned between 62 MHz and 75 MHz to search for the Doppler-free two-photon transition resonances in the trap.

All five transitions from the ^{86g}Rb 5S$_{1/2}$ F = 5/2 state to the 5D$_{5/2}$ states were found by monitoring the number of photoelectrons, and the spectrum is shown in Figure 6.3. The values on the x axis are f_{trap}, the MBR laser frequency in the trap. Besides Equation 6.4, f_{trap} also equals $(I.S. + H.F. - A_{5S})/2$, where A_{5S} = -1578.753(1) MHz [30], the magnetic dipole constant of the 5S$_{1/2}$ state in ^{86g}Rb, $I.S.$ is the isotope shift between ^{86g}Rb and ^{87}Rb for the 5S$_{1/2}$ to 5D$_{5/2}$ transition, and $H.F.$ is the hyperfine structure of the 5D$_{5/2}$ state which includes the magnetic dipole constant and the electric quadrupole constant of the 5D$_{5/2}$ state, A(5D$_{5/2}$) and B(5D$_{5/2}$). The values of $I.S.$ and A(5D$_{5/2}$) and B(5D$_{5/2}$) were extracted by fitting the ^{86g}Rb spectrum with five Voigt functions, and the results are shown in Table 6.3.

6.2.3 ^{86m}Rb Measurement

For the ^{86m}Rb experiment, we measured the 5S$_{1/2}$ to 5D$_{5/2}$ two-photon transition spectra from both 5S$_{1/2}$ state hyperfine sublevels, F = 11/2 and 13/2, as shown in Figure 6.4.

For the F = 11/2 to 5D$_{5/2}$ transition, AOM 1 was in a single-pass setup (Figure 6.1 a), $f_{trap} = f_{cell} + f_{AOM2} - f_{AOM1}$. The reference is the ^{85}Rb F = 2 to 4 (5S$_{1/2}$ state to 5D$_{5/2}$ state) transition,

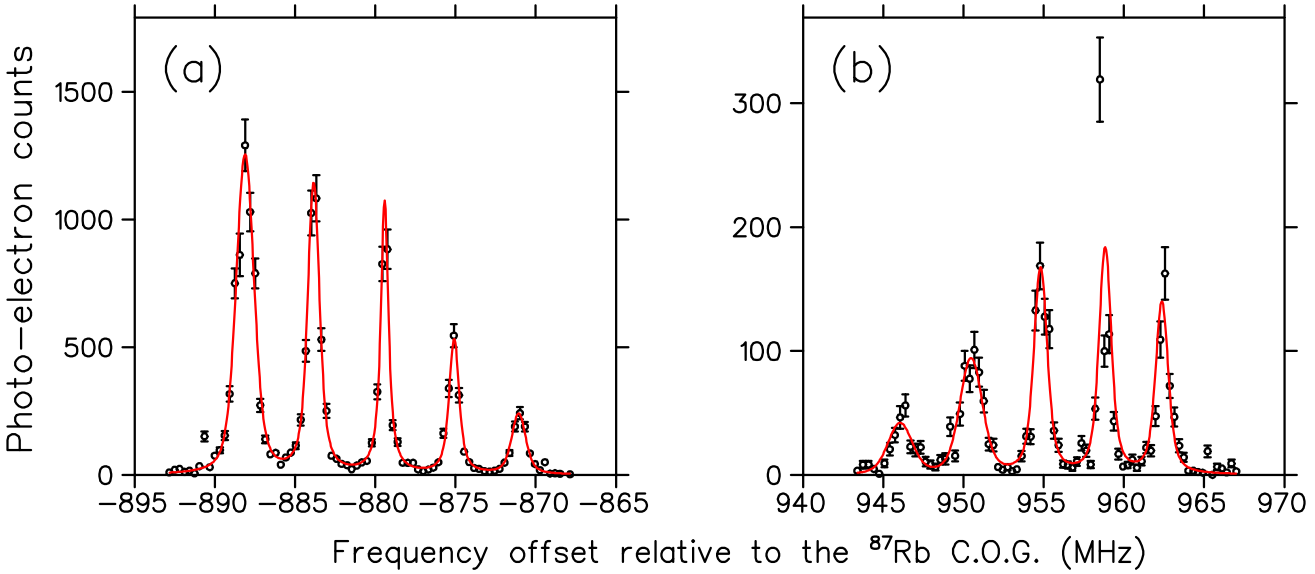

Figure 6.4: Hyperfine spectra of the $^{86\mathrm{m}}$Rb $5\mathrm{D}_{5/2}$ state, measured by Doppler-free two-photon transitions between the $5\mathrm{S}_{1/2}$ and $5\mathrm{D}_{5/2}$ states. (a) between $5\mathrm{S}_{1/2}$ F = 13/2 and $5\mathrm{D}_{5/2}$ F = 17/2 ... 9/2, (b) between $5\mathrm{S}_{1/2}$ F = 11/2 and $5\mathrm{D}_{5/2}$ F = 15/2 ... 7/2.

and $f_{cell} = 803.258$ MHz. f_{AOM2} was fixed at +80 MHz, and f_{AOM1} was scanned between 60 MHz and 84 MHz. The anomalously high count at ~ 958 MHz in Figure 6.4 (b) was caused by .. scalar counter in the second scan. Removing this data point didn't change the fitting results for the hyperfine constants and the slight change in the isotope shift was still within 1σ of the original result, so we decided to not make any modification on the counts.

For the F = 13/2 to $5\mathrm{D}_{5/2}$ transition, AOM 1 was in a double-pass setup (Figure 6.1 b), $f_{trap} = f_{cell} + f_{AOM2} - 2 \times f_{AOM1}$. The reference is the ^{85}Rb F = 3 to 5 ($5\mathrm{S}_{1/2}$ state to $5\mathrm{D}_{5/2}$ state) transition, and f_{cell} = -719.333 MHz. f_{AOM2} was fixed at +80 MHz, and f_{AOM1} was scanned between 114 MHz and 127 MHz.

By the same method described in Section 6.2.2, the values of $I.S.$ and $A(5\mathrm{D}_{5/2})$ and $B(5\mathrm{D}_{5/2})$ for $^{86\mathrm{m}}$Rb were also extracted (results in Table 6.3). Moreover, since we have the two-photon transition spectrum from both ground-state hyperfine sublevels, the $5\mathrm{S}_{1/2}$ state magnetic dipole constant for $^{86\mathrm{m}}$Rb was also determined by fitting the spectra of Figure 6.4 a and b together, $A(5\mathrm{S}_{1/2}) = 563.04(2)(5)$ MHz, compared to 563.5(3) MHz in Thibault [30].

6.2.4 $^{81\mathrm{g}}$Rb Measurement

Both the $^{86\mathrm{g}}$Rb and $^{86\mathrm{m}}$Rb measurements were done with a four-pass setup for the 778 nm light in the trap position, as shown in Figure 6.1 (a) and (b). This four-pass setup was designed for exotic particle search experiments in ^{86}Rb, where a high transition rate is required but the MBR laser

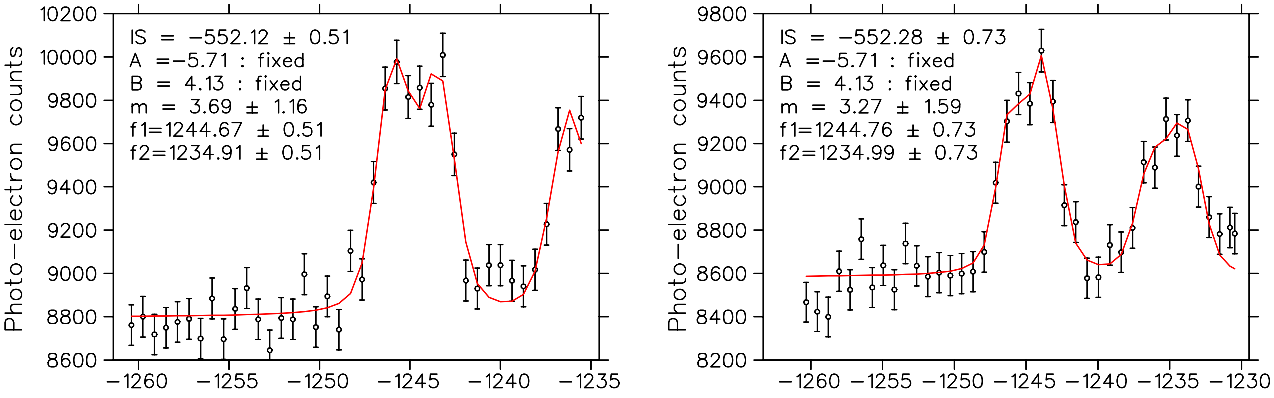

(a) frequency offset relative to the ^{87}Rb COG (MHz) (b) frequency offset relative to the ^{87}Rb COG (MHz)

Figure 6.5: $^{81\text{g}}$Rb measurements. (a) one-peak scan, (b) two-peak scan. IS is the isotope shift between $^{81\text{g}}$Rb and ^{87}Rb for the 5S$_{1/2}$ to 5D$_{5/2}$ transition, A and B are the hyperfine constants of the 5D$_{5/2}$ state, m is the magnetic field crossing the trap cloud. f_1 and f_2 are the positions for the resonance peaks. All of these parameters are extracted from curve fittings using the Voigt profiles, including transitions between Zeeman sublevels.

power is not enough for saturating the two-photon transitions.

In the $^{81\text{g}}$Rb measurement, the four-pass setup was removed and AOM 2 was replaced by an EOM switch (as shown in Figure 6.2). The reason for these modifications is that we were considering a power buildup cavity of the 778 nm light for the $^{81\text{g}}$Rb exotic particle search experiment. This requires linear polarization light, so the PBS (polarized beamsplitter) has to be removed. The details for the power buildup cavity can be found in Section 5.11.

We made three different kinds of scans in the $^{81\text{g}}$Rb measurement, including a 1-peak scan shown in Figure 6.5 (a), a 2-peak scan shown in Figure 6.5 (b) and a 3-peak scan shown in Figure 6.6 (a). The AOM schemes in all three scans can be described by

$$f_{trap} = f_{cell} - f_{AOM1} - f_{AOM2}, \tag{6.5}$$

where f_{cell} = -1295.333 MHz, locked to the ^{87}Rb F = 2 to 4 (5S$_{1/2}$ state to 5D$_{5/2}$ state) transition. f_{AOM1} was scanned at -105 – -135 MHz range in the 2-peak scan and the 3-peak scan, and at -105 – -130 MHz range in the 1-peak scan. f_{AOM2} was fixed at +70 MHz for the 1-peak scan and the 2-peak scan, and +60 MHz for the 3-peak scan.

Table 6.4 summaries the fitting results of these three scans, including the isotope shift, hyperfine constants A and B, the magnetic field and the derived resonance frequencies for the transition peaks. A comparison of these parameters shows a consistency within 1σ in all three scans. During the curve ftting of the 1-peak scan and 2-peak scan, the 5D$_{5/2}$ A and B constants were fixed at the same values as the results from the 3-peak scan. The reason is that the resonance peaks are

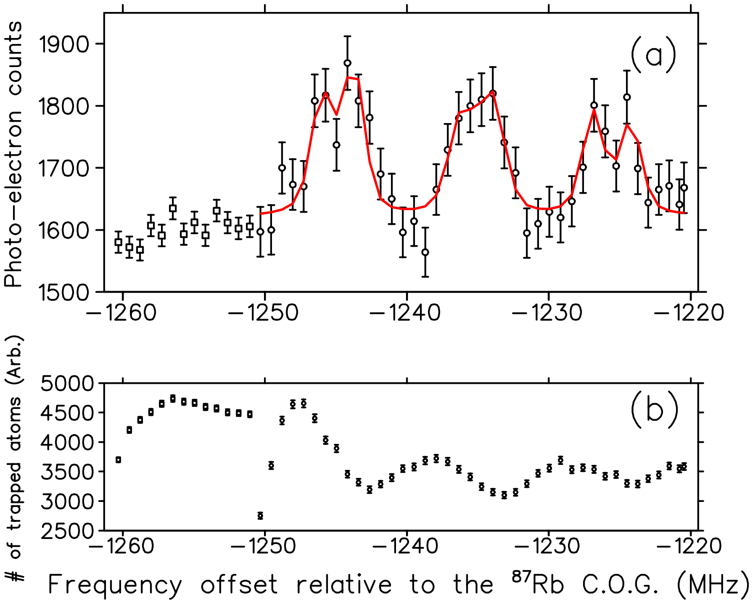

Figure 6.6: ^{81g}Rb measurements. (a) two-photon transition spectrum for the 5S$_{1/2}$ F= 2 to 5D$_{5/2}$ F = 4, 3 and 2 transitions (lower ν to higher ν), the curve between -1250 MHz and -1219 MHz was fitted by the Voigt profiles of multiple Zeeman transitions. The part between -1261 MHz and -1250 MHz is from another scan which shows no peak at less than -1250 MHz, and the peak at x = -1245 MHz is the F = 2 to F = 4 transition. (b) number of trapped atoms, as determined by CCD camera image of the trap D$_2$ transition fluorescence. We choose to suppress the zero of the y-axis so the errors can be seen.

	Figure 6.5 (a)	Figure 6.5 (b)	Figure 6.6
# of peaks	1	2	3
Isotope shift	-552.12(51)	-552.28(73)	-552.40(28)
5D$_{5/2}$ A	-5.71	-5.71	-5.71(12)
5D$_{5/2}$ B	4.13	4.13	4.13(1.65)
B field	3.7(1.2)	3.3(1.6)	3.1(2)
f$_1$	-1244.67(51)	-1244.76(73)	-1244.82(45)
f$_2$	-1234.91(51)	-1234.99(73)	-1235.05(63)
f$_3$	N. A.	N. A.	-1225.55(31)

Table 6.4: Summary of the fitting results in the ^{81g}Rb measurements. All frequencies are in MHz. The magnetic field is in Gauss.

determined by both the isotope shift and the hyperfine A and B constants of the 5D$_{5/2}$ state, and only one (or two) resonance peaks are not enough to determine all three parameters.

The background counts in the ^{81g}Rb spectra are very high, due to the 4.6-hour half-life of the ^{81g}Rb electron capture decay (details in Section 5.10.2). We have to turn off the upstream radioactive beam for hours to let the backgrounds become low enough to see the photo-electron

	$^{86\text{m}}$Rb	$^{86\text{m}}$Rb	$^{86\text{g}}$Rb	$^{81\text{g}}$Rb	^{87}Rb
$5S_{1/2}$ F level	13/2	11/2	5/2	2	2
FWHM (MHz)	1.3(3)	1.6(4)	1.7(5)	3.0(6)	3.2(2)

Table 6.5: FWHM of the $5S_{1/2}$ to $5D_{5/2}$ Doppler-free two-photon transition spectra in Rb isotopes.

signals. In contrast, there is no electron capture decay involved in the ^{86}Rb measurements, and the background counts in the ^{86}Rb spectra are negligible.

Another difference between the $^{81\text{g}}$Rb and the ^{86}Rb spectra is the linewidth. The FWHM of the $^{81\text{g}}$Rb spectra is 2 – 3 times that of the ^{86}Rb spectra, as shown in Table 6.5. Moreover, the transitions between the Zeeman sublevels are very obvious in the $^{81\text{g}}$Rb spectra, due to the 3-Gauss magnetic field crossing the $^{81\text{g}}$Rb trap cloud. So the curve fittings of the $^{81\text{g}}$Rb spectra were done including Zeeman sub-transitions, and the details can be found in Section 6.3.3 where the systematic errors are discussed.

6.2.5 Trap Fluorescence Correction

The number of trapped atoms was not constant in the scan, as shown in Figure 6.6 (b). To take this effect into account, we scaled the photoelectron counts by the number of trapped atoms in the ^{86}Rb spectra, and this correction improved the relative hyperfine line intensities.

In the $^{81\text{g}}$Rb measurement, the radioactive background was very high (see Section 6.3.3). So scaling the number of photoelectrons requires removing the background counts, which is hard to determine and affects fitting results. Instead, we scaled the fitting functions with the number of trapped atoms, and the spectrum fitting was improved without modifying the photo-electron counts, as shown in Figure 6.6 (a).

6.2.6 Relative Intensity

For two-photon transitions between a $S_{1/2}$ and a D_J state, the rank for the two-photon operator is $k = 2$. The relative hyperfine line intensities can be calculated using Equation 2.12, and the results are summarized in Table 6.6.

The relative hyperfine line intensities in ^{86}Rb spectra agree qualitatively with the theoretical values listed in Table 6.6. Possible reasons for the deviation in some of the spectrum lines include the Zeeman broadening which is not constant in all the transitions, and the optical pumping and hyperfine pumping effects for the cold atoms.

In the $^{81\text{g}}$Rb spectra, the relative intensities are almost constant for all peaks. The reasons include high radioactive background, small signal to noise ratio, and the lack of time to optimize

$^{86\text{g}}$Rb			$^{86\text{m}}$Rb			$^{86\text{m}}$Rb			$^{81\text{g}}$Rb		
F_g	F_e	Relative	F_g	F_e	Relative	F_g	F_e	Relative	F_g	F_e	Relative
5/2	9/2	33.3%	13/2	17/2	23.1%	11/2	15/2	5.4%	2	4	37.5%
5/2	7/2	17.1%	13/2	15/2	15.1%	11/2	13/2	8.8%	2	3	17.5%
5/2	5/2	7.2%	13/2	13/2	9.1%	11/2	11/2	10.7%	2	2	6.3%
5/2	3/2	2.1%	13/2	11/2	4.7%	11/2	9/2	11.0%	2	1	1.3%
5/2	1/2	0.3%	13/2	9/2	1.8%	11/2	7/2	10.3%			

Table 6.6: Theoretical values of relative hyperfine line intensities for the $5S_{1/2}$ to $5D_{5/2}$ two-photon transitions in $^{86\text{m}}$Rb, $^{86\text{g}}$Rb and $^{81\text{g}}$Rb. F_g and F_e are the F numbers of the $5S_{1/2}$ and $5D_{5/2}$ states, respectively.

laser intensity to ionize fewer atoms.

6.3 Systematic Errors

The dominant effects that contribute to the systematic errors of this experiment include the AC Stark shift, the reference cell offset and the Zeeman shift. We investigated these systematic effect in the offline traps and the vapor cell using stable Rb isotopes. The deduced results were also compared to Nez's experiment [57], which measured the same $5S_{1/2}$ to $5D_{5/2}$ two-photon transitions in stable Rb isotopes but using low intensity laser light and in zero B field environment. The kHz-level precision of Nez's measurements provided great references to investigate the 10^1 – 10^2 kHz systematic errors in our measurements.

6.3.1 AC Stark Shift

The interaction between an atom and the oscillating electric field of the laser light induces shifts on the atomic energy levels. For linearly polarized light, the shift of energy level $|n\rangle$ can be deduced by second order perturbation theory [58]:

$$\Delta E_n^{(2)} = \frac{(eE_z)^2}{4}\left[\sum_{E_m+\hbar\omega\neq E_n}\frac{|\langle\psi_n\,|z|\,\psi_m\rangle|^2}{E_n-E_m-\hbar\omega}+\sum_{E_m-\hbar\omega\neq E_n}\frac{|\langle\psi_n\,|z|\,\psi_m\rangle|^2}{E_n-E_m+\hbar\omega}\right], \tag{6.6}$$

where E_z and ω are the amplitude and frequency of the laser electric field , respectively. $\langle\psi_n\,|z|\,\psi_m\rangle$ is the transition matrix element between atomic states $|n\rangle$ and $|m\rangle$. The summation is over all possible atomic states $|m\rangle$ which have allowed E1 transition with the $|n\rangle$ state.

In the $5S_{1/2}$ to $5D_{5/2}$ two-photon spectroscopy measurements, both the trapping laser and repumping laser were chopped off. Only the 778 nm light from the MBR laser was on during the photoionization (as shown in the duty cycle of Figure 3.6). The linearly-polarized MBR laser (∼

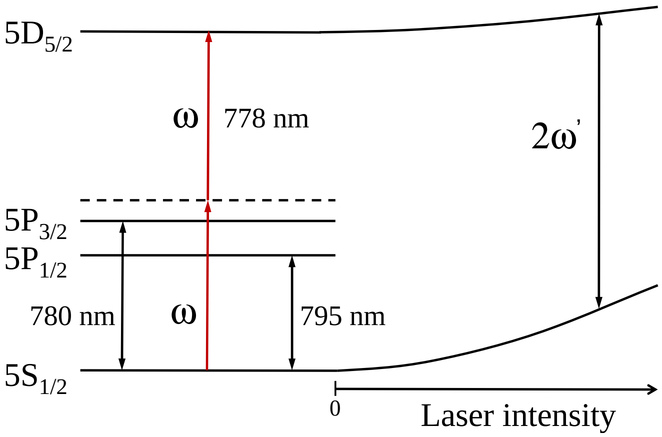

Figure 6.7: AC Stark shift for the $5S_{1/2}$ and $5D_{5/2}$ two-photon transitions, which is induced by the 778 nm light.

0.4 Watts) was focused into a 1.2 mm diameter beam to overlap with the trap cloud in a two-pass setup, resulting in a 70 Watts/cm^2 light intensity at the trap position in the ^{81g}Rb measurements.

The 778 nm light induces shifts for the $5S_{1/2}$ and $5D_{5/2}$ states by coupling these two states to the $5P_{1/2}$ or $5P_{3/2}$ states. The other possible states are not considered since they are far off resonance with the 778 nm light.

$$\Delta E^{(2)}_{5S_{1/2}} = \frac{(eE_z)^2}{4}\left[\frac{\left|\left\langle \psi_{5S_{1/2}}\left|z\right|\psi_{5P_{1/2}}\right\rangle\right|^2}{E_{5S_{1/2}} - E_{5P_{1/2}} + \hbar\omega} + \frac{\left|\left\langle \psi_{5S_{1/2}}\left|z\right|\psi_{5P_{3/2}}\right\rangle\right|^2}{E_{5S_{1/2}} - E_{5P_{3/2}} + \hbar\omega}\right], \tag{6.7}$$

$$\Delta E^{(2)}_{5D_{5/2}} = \frac{(eE_z)^2}{4}\left[\frac{\left|\left\langle \psi_{5D_{5/2}}\left|z\right|\psi_{5P_{3/2}}\right\rangle\right|^2}{E_{5D_{5/2}} - E_{5P_{3/2}} - \hbar\omega}\right]. \tag{6.8}$$

The $5P_{1/2}$ to $5D_{5/2}$ transition is forbidden by E1 transition, so the $5S_{1/2}$ state will be shifted more than the $5D_{5/2}$ state, as shown in Figure 6.7. Then the light shift for the $5S_{1/2}$ to $5D_{5/2}$ two-photon transition frequency is

$$\begin{aligned} h\,\Delta f &= \left(\Delta E^{(2)}_{5D_{5/2}} - \Delta E^{(2)}_{5S_{1/2}}\right)/2 \\ &= \frac{(eE_z)^2}{8}\left[\frac{\left|\left\langle \psi_{5D_{5/2}}\left|z\right|\psi_{5P_{3/2}}\right\rangle\right|^2}{E_{5D_{5/2}} - E_{5P_{3/2}} - \hbar\omega} - \frac{\left|\left\langle \psi_{5S_{1/2}}\left|z\right|\psi_{5P_{1/2}}\right\rangle\right|^2}{E_{5S_{1/2}} - E_{5P_{1/2}} + \hbar\omega} - \frac{\left|\left\langle \psi_{5S_{1/2}}\left|z\right|\psi_{5P_{3/2}}\right\rangle\right|^2}{E_{5S_{1/2}} - E_{5P_{3/2}} + \hbar\omega}\right] \end{aligned} \tag{6.9}$$

Equation 6.9 implies a theoretical value of -70 kHz for the light shifts of the $5S_{1/2}$ to $5D_{5/2}$ transition, which agrees with our measurement in a ^{85}Rb trap, as well as the measurement by Nez [57]. By checking the resonance frequency shifts between the 778 nm laser at full power and at half power, a 70(70) kHz shift is deduced from the ^{85}Rb measurement. We chose to treat this as an uncertainty instead of making a correction, since the exact laser intensity for photoionizing a trapped atom is not constant.

In the ^{86}Rb experiments, the 778 nm laser was in a four-pass setup. The light intensity in the vacuum chamber was 1.6x bigger than for ^{81g}Rb (since AOM 2 cut off 20% power), so the AC Stark shift in this case is estimated to be $\sim$ 110 kHz.

6.3.2 Reference Cell Offset

The light polarization in the Rb vapor cell was set as circular while searching for the two-photon resonance frequencies of the trapped radioactive Rb isotopes, to enhance the 420 nm fluorescence signal and maintain a stable locking for the MBR laser during the AOM frequency scans. However, the reference point in the vapor cell will be shifted by the Zeeman effect due to the circular polarization configuration. This induces a systematic error for the resonance frequency search in the MOT.

The mu-metal shielding around the Rb vapor cell reduces the Earth's magnetic field by a factor of 5, leaving about 0.1 Gauss residual magnetic field in the vapor cell center. To investigate the systematic offset of the reference point caused by this residual B field, we did an analysis in an offline ^{85}Rb MOT. The analysis was done by measuring the difference of the ^{85}Rb two-photon resonance frequencies in the trap, when the light polarizations in the vapor cell are in opposite circular handedness. The results are shown in Table 6.7, which imply an average of 70(65) kHz offset in the reference point. However, since the uncertainty for this offset is about 100%, we treat it as a 70 kHz systematic uncertainty for the isotope shift measurement.

Besides the systematic offset of the reference point, we also compared the measured 5D$_{5/2}$ state hyperfine structure with the precise measurement of Nez et al. [57].

By fitting the centroids listed in Table 6.7 to the 5D$_{5/2}$ state hyperfine structure measured by Nez [57] (fix the 5D$_{5/2}$ state hyperfine constants as the values reported by Nez), we deduced an offset of -70(49) kHz between our measurement and Nez's. This is consistent with the 70 kHz uncertainties on the reference point, so it doesn't contribute any additional systematic error to the isotope shift measurements.

6.3.3 Zeeman Shift

The Zeeman shift is caused by a nonzero magnetic field across the trap cloud, which induces Zeeman splittings in the two-photon transition resonances and also shifts the resonance centers. In our online experiment, the magnetic quadrupole trapping field was not turned off. Although the Earth's magnetic field was mostly canceled by 3 Helmholtz coils, there was 0.5 – 1 Gauss field

Polarization Angle		Centre Frequency [MHz]		
MOT	Cell	F = 3 to 3	F = 3 to 4	F = 3 to 5
100°	54°	83.70(2)	88.29(3)	92.97(3)
100°	322°	83.73(2)	88.20(3)	92.94(2)
210°	322°	83.77(4)	88.23(3)	92.85(2)
210°	54°	83.75(3)	88.31(3)	93.03(2)

Table 6.7: Vapor cell reference offset test using an offline ^{85}Rb MOT. Each angle of the polarizer corresponds to a σ^+ or σ^- circular polarization. Different configurations of circular light polarizations were tested in both the MOT and the Rb vapor cell.

difference across the 1 mm wide trap cloud.

In the ^{86g}Rb and ^{86m}Rb measurements, the 778 nm laser was passed through the trap cloud four times using a quarter wave plate, a polarizing beamsplitter (PBS), and a retro-reflecting mirror, as shown in Figure 6.1 and 6.2. The resulting polarizations for the 778 nm laser were $\sigma^+\sigma^+$ for the first pass, and $\sigma^-\sigma^-$ for the second. The reason for the four-pass design for the 778 nm laser was that this system was designed for efficient photo-ionization to search for massive particles in isomer decay [27]. In this system, the strongest two-photon transition signals come from absorbing two photons from opposite directions with either $\sigma^+\sigma^+$ or $\sigma^-\sigma^-$ polarizations [46], which drives Zeeman transitions with ΔM = +2 or ΔM = -2, respectively. The resulting resonance profile is broadened; however, the centroid is not shifted very much as ΔM = ±2 transitions are symmetrically displaced. The transition induced by $\sigma^+\sigma^-$ photons is much weaker than the other two configurations and the selection rule for this case is ΔM = 0, so the centroid is not shifted much either.

As shown in Figure 6.2, the four-pass setup was removed during the ^{81g}Rb measurement by taking out the quarter waveplate and the polarizing beamsplitter in front of the vacuum chamber. Then there is only one 778 nm laser beam in each direction and the light polarizations are linear, which drives ΔM = 0 transitions and minimizes the resonance centroid shifts.

The Zeeman frequency shift was largest in the ^{81g}Rb measurements. Due to the high radioactive background from the electron capture decay (as discussed in Section 5.10.2), the data-taking time was limited and the ^{81g}Rb trap cloud size was not minimized. The achieved trap size in the ^{81g}Rb measurements was six times bigger than in the case of ^{86}Rb. The magnetic field difference across the trap cloud was about 3 Gauss, and Zeeman splittings are easily visible in the spectrum of Figure 6.6. In contrast, the radioactive background in the ^{86}Rb experiments was much lower, and the cloud size was minimized to 0.5 mm diameter.

The systematic error caused by the Zeeman effect was analyzed using an off-line ^{87}Rb MOT under the same experimental conditions as the ^{81g}Rb measurements. ^{87}Rb has the same nuclear

Run	Corrections	Offset	A($5D_{5/2}$)	ΔA($5D_{5/2}$)	B($5D_{5/2}$)	ΔB($5D_{5/2}$)
2910	counts	-0.41	-7.43(2)	0.03	0.8(1)	0.5
2910	fitfunc	-0.31	-7.43(2)	0.03	1.0(1)	0.3
2918	counts	-0.19	-7.41(1)	0.05	1.5(1)	0.3
2918	fitfunc	-0.19	-7.41(1)	0.05	1.5(1)	0.3
2919	counts	-0.25	-7.42(2)	0.04	1.0(1)	0.3
2919	fitfunc	-0.24	-7.42(2)	0.04	1.0(1)	0.3
Average		-0.27	-7.42(2)	0.04	1.1(1)	0.3
Nez's results [57]			-7.4605(3)		1.2713(20)	

Table 6.8: Systematic error analysis on Zeeman effect using an offline ^{87}Rb MOT. All units are in MHz. Results from three runs are listed and averaged to deduce the systematic errors for the $\delta\nu^{81g,87}$ isotope shift (the Offset column) and the $5D_{5/2}$ state hyperfine constants (the ΔA($5D_{5/2}$) and ΔB($5D_{5/2}$) columns). For each run, the fluctuation of the number of the trapped atoms were taken into account in two ways (details in Section 6.2.5), by scaling the photoelectron counts or by scaling the fitting function. The deduced $5D_{5/2}$ state hyperfine constants are in 2σ agreement with Nez's measurement [57].

spin as ^{81g}Rb, so the Zeeman shifts are the same in both cases with the same magnetic field (the terms proportional to the nuclear g-factor are negligible). Each two-photon resonance is split into five sub-peaks which represent Zeeman transitions with $\Delta M = 0$ and $m'_F = m_F = 0$, ±1 and ±2, and the hyperfine constants A and B for the $5D_{5/2}$ state are floated in the fitting function. The centroids of the resonance peaks are determined by the hyperfine constants A and B, and an offset. Since the 778 nm laser was also locked to the ^{87}Rb transitions in the vapor cell, there is no isotope shift between the vapor cell reference and the ^{87}Rb resonances in the MOT, so the centroid offset is considered to be a systematic error for the ^{81g}Rb isotope shift. The systematic errors for the A and B constants are determined by the difference between our measurement and the low-intensity zero-field measurement of Nez et al. [57]. As shown in Table 6.8, the ^{87}Rb analysis showed systematic errors of 0.27 MHz for the $\delta\nu^{81g,87}$ isotope shift, 0.04 MHz for the $A(5D_{5/2})$ constant and 0.31 MHz for the $B(5D_{5/2})$ constant in ^{81g}Rb. In addition, the $5D_{5/2}$ state hyperfine constants we deduced for ^{87}Rb are in 2σ agreement with Nez's measurement [57].

In the ^{87}Rb analysis, we attributed the centroid offsets to a Zeeman shift, and attributed the linewidth to Zeeman broadening, i.e., the average Zeeman splittings. To estimate the systematic Zeeman shifts in ^{86}Rb, we make the conservative assumption that the linewidth is also entirely due to Zeeman broadening, and then we scale the Zeeman shift with the linewidth. As shown in Table 6.5, the average FWHM linewidth is 1.7 MHz in ^{86g}Rb and 1.5 MHz in ^{86m}Rb, compared to

3.0 MHz in ^{87}Rb. So the scaling factor is 0.6 for $^{86\mathrm{g}}$Rb and 0.5 for $^{86\mathrm{m}}$Rb.

	$^{86\mathrm{m}}$Rb	$^{86\mathrm{g}}$Rb	$^{81\mathrm{g}}$Rb
Zeeman shift	0.14	0.16	0.27
AC Stark shift	0.11	0.11	0.07
Reference cell offset	0.07	0.07	0.07
Total error	0.19	0.21	0.29

Table 6.9: Summary of systematic errors for isotope shifts (in MHz). All three components are summed quadratically.

6.3.4 Summary of Systematic Errors

The systematic errors for the isotope shifts are summarized in Table 6.9. Due to accuracy limitations and the complexity of the error sources, we are unable to correct these systematic errors but consider them as uncertainties, which we add quadratically.

The systematic error for A(5S$_{1/2}$) of $^{86\mathrm{m}}$Rb is determined to be 0.05 MHz, which is 1/3 of the systematic error for the $^{86\mathrm{m}}$Rb isotope shift. The reason for this is that the frequency offset of the $^{86\mathrm{m}}$Rb two-photon transition spectrum in Figure 6.4 includes both $\delta\nu^{86m,87}$ and $A(5\mathrm{S}_{1/2})$, and the ratio between them is 1:3 and 1:3.5 for transitions from the 5S$_{1/2}$ (F = 13/2 and 11/2) to 5D$_{5/2}$ states.

The systematic errors for the 5D$_{5/2}$ state hyperfine constants are summarized in Table 6.3, which come from the Zeeman shift analysis in Section 6.3.3. Reference cell offsets do not affect the measurement of the hyperfine structure, and the Zeeman shift analysis already includes the possible AC Stark effect on the hyperfine constants. The hyperfine constants we measured for the 5D$_{5/2}$ state in these three Rb isotopes are consistent within 2σ with the prediction using Thibault's [30] values for $A(5\mathrm{S}_{1/2})$ and $B(5\mathrm{P}_{3/2})$, assuming no hyperfine anomaly.

6.4 Hyperfine Anomaly

We note that detailed hyperfine anomaly measurements were done in 5S and 6S states by Ref. [59]. However, our measurements are not accurate enough to reveal a hyperfine anomaly. A test by analyzing the ratio of $A(5\mathrm{D}_{5/2})/A(5\mathrm{S}_{1/2})$ shows no evidence for a hyperfine anomaly with 1% sensitivity for those three radioactive Rb isotopes with respect to ^{87}Rb. We have summarized the situation in Figure 6.8, in which all three $A(5\mathrm{D}_{5/2})$ constants for radioactive Rb isotopes are from our measurement, plus the $A(5\mathrm{S}_{1/2})$ constant for $^{86\mathrm{m}}$Rb. The other $A(5\mathrm{S}_{1/2})$ constants for radioactive Rb isotopes come from Thibault's measurements [30], and all the hyperfine constants

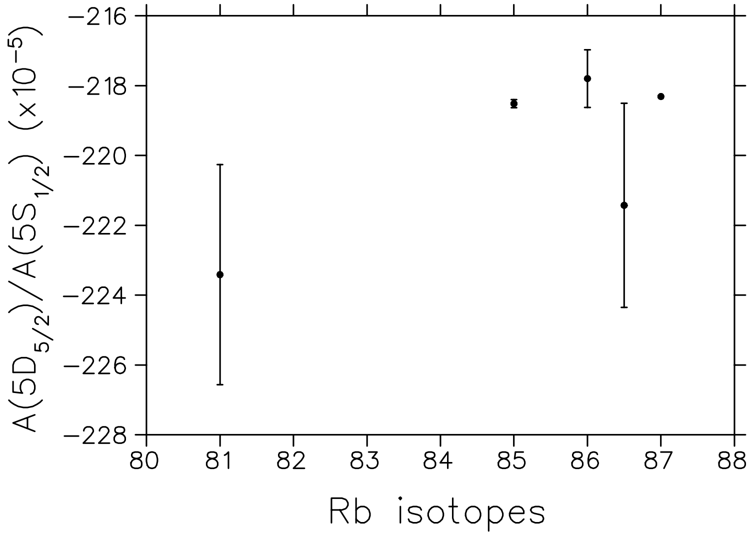

Figure 6.8: Ratio of hyperfine A constants between $5D_{5/2}$ and $5S_{1/2}$ states in Rb isotopes, the mass number of 86.5 is referred as ^{86m}Rb.

for stable Rb isotopes are from Nez's measurements [57].

Similarly, fitting for the magnetic octupole hyperfine contribution does not change the results for the hyperfine A and B constants significantly, nor does it yield a nonzero value for C within errors. Extracting the magnetic octupole moment from a D state transition would require more difficult higher-order calculations than these needed for ^{133}Cs in the $6S_{1/2}$ to $6P_{3/2}$ transition [60].

6.5 Specific Mass Shifts in Rb Isotopes

Based on the measured isotope shifts for the $5S_{1/2}$ to $5D_{5/2}$ transition in ^{86m}Rb and ^{86g}Rb and ^{81g}Rb, we deduced the specific mass shifts between the $5S_{1/2}$ and $5D_{5/2}$ states in Rb isotopes by making a King Plot.

6.5.1 King Plot

A King Plot analysis [23, 61] can be used to separate the mass component and the field component of isotope shifts. It requires isotope shifts for two atomic transitions. The first one we chose is the D_2 transition between the $5S_{1/2}$ and $5P_{3/2}$ states, because excellent survey data from Ref. [30] exist. The second one is between the $5S_{1/2}$ and $5D_{5/2}$ states, the Doppler-free two-photon transition measured in this paper. The isotope shifts for these two transitions can be written as [61]:

$$IS_1^{AA'} = \frac{A-A'}{AA'}(N_1+S_1) + F_1 \cdot \delta\langle r^2\rangle^{AA'}, \tag{6.10}$$

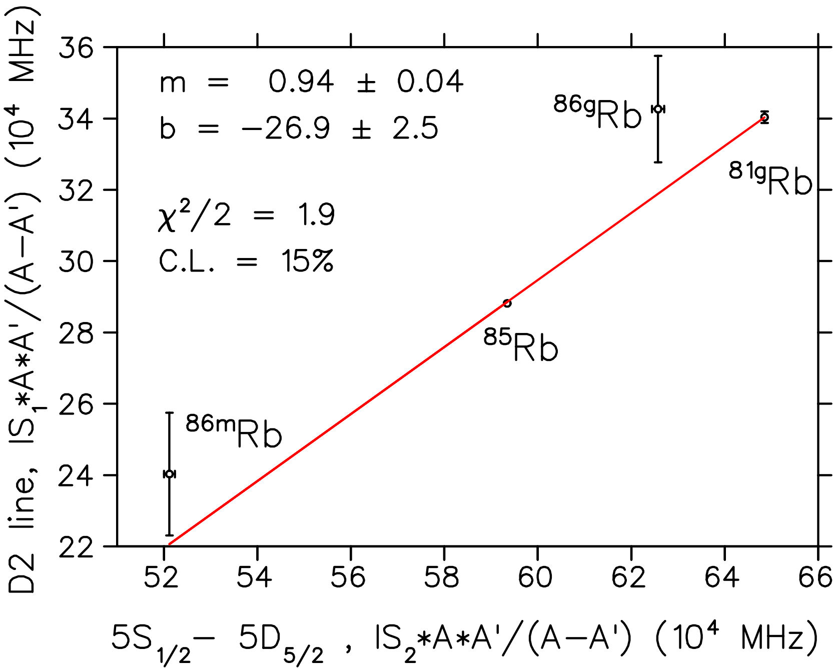

Figure 6.9: King plot of Rb isotope shifts (reference to ^{87}Rb) in two atomic transitions: the 5S$_{1/2}$ to 5D$_{5/2}$ transition from this work, and the 5S$_{1/2}$ to 5P$_{3/2}$ transition [30, 56]. The isotope shift data are from Table 6.2 and are normalized by a mass factor $\frac{AA'}{A-A'}$. m and b are the slope and y-intercept of the straight line fitting, respectively.

$$IS_2^{AA'} = \frac{A-A'}{AA'}(N_2+S_2) + F_2{\cdot}\delta\langle r^2\rangle^{AA'}. \tag{6.11}$$

These two equations can be combined to eliminate the $\delta\langle r^2\rangle^{AA'}$ term, and we obtain

$$\begin{aligned} IS_1^{AA'}{\cdot}\tfrac{AA'}{A-A'} &= (N_1+S_1)-(N_2+S_2)\cdot F_1/F_2 \\ &\quad + F_1/F_2\cdot IS_2^{AA'}\cdot\tfrac{AA'}{A-A'}, \end{aligned} \tag{6.12}$$

Equation 6.12 shows a linear relationship between $IS_1^{AA'}\cdot\frac{AA'}{A-A'}$ and $IS_2^{AA'}\cdot\frac{AA'}{A-A'}$. The slope and intercept are F_1/F_2 and $(N_1+S_1)-(N_2+S_2){\cdot}F_1/F_2$ respectively. Since N_1 and N_2 can be calculated exactly, the intercept can be further simplified to get $S_1 - S_2{\cdot}(F_1/F_2)$.

The plot is shown in Figure 6.9. The isotopes used to make this graph are ^{81g}Rb, ^{86m}Rb, ^{86g}Rb and ^{85}Rb, with ^{87}Rb as the reference isotope. The related isotope shift data are summarized in Table 6.2. The uncertainties in both transitions are used for linear fitting using the Weighted Total Least Squares (WTLS) method [62].

From the King plot, we found

$$\begin{aligned} F_1/F_2 &= 0.94(4), \text{and} && (6.13)\\ (N_1+S_1)-(N_2+S_2)\cdot F_1/F_2 &= -269(25)\ \text{GHz}\cdot\text{amu}. && (6.14)\end{aligned}$$

According to Equation 1.11, N_1 = 210.780 GHz·amu and N_2 = 422.718 GHz·amu, hence the difference betwen the specific mass shift constants of the $5P_{3/2}$ and $5D_{5/2}$ states is

$$S_1 - S_2\cdot(F_1/F_2) = -83(31)\ \text{GHz}\cdot\text{amu}. \tag{6.15}$$

From the King Plot, we deduced F_1/F_2 and $S_1 - S_2\cdot(F_1/F_2)$. To find the specific mass shifts for the $5S_{1/2}$ to $5D_{5/2}$ transition, we need to know S_1, the specific mass shift constant for the D_2 transition.

6.5.2 $\delta\langle r^2\rangle^{85,87}$ and Field Shift

Dzuba *et al* [63] calculated the field shift constants for Rb with 1% precision, $F(5S) = -551.85$ MHz/fm^2 and $F(5P_{3/2}) = 15.60$ MHz/fm^2; hence the field shift constant of the D_2 transition is F_1 = −567.45(1%) MHz/fm^2.

The nuclear charge radius can be deduced from muonic X-ray data. Angeli [64, 65] deduced $\langle r^2\rangle_{85}^{1/2} = 4.2031(18)$ fm for ^{85}Rb and $\langle r^2\rangle_{87}^{1/2} = 4.1981(17)$ fm for ^{87}Rb, with a relative error of

$$\langle r^2\rangle_{85}^{1/2} - \langle r^2\rangle_{87}^{1/2} = 0.0003\ \text{fm}. \tag{6.16}$$

Then the nuclear charge radius difference between ^{85}Rb and ^{87}Rb is

$$\delta\langle r^2\rangle^{85,87} = \left[\langle r^2\rangle_{85}^{1/2} + \langle r^2\rangle_{87}^{1/2}\right] \times \left[\langle r^2\rangle_{85}^{1/2} - \langle r^2\rangle_{87}^{1/2}\right] = 0.0420(25)\ \text{fm}^2. \tag{6.17}$$

Therefore the field shift of the D_2 transition between ^{85}Rb and ^{87}Rb is determined to be

$$F_1\cdot\delta\langle r^2\rangle^{85,87} = -23.8(1.4)\ \text{MHz}. \tag{6.18}$$

6.5.3 Specific Mass Shift

Barwood *et al* [56] measured $\delta\nu_1^{85,87} = -78.095(12)$ MHz; consequently, the specific mass shift value between ^{85}Rb and ^{87}Rb for the D_2 transition can be determined to be $\text{SMS}_1^{85-87} = S_1\frac{A-A'}{AA'} =$ 2.8(1.4) MHz, thus $S_1 = -10.3(5.3)$ GHz·amu. Using this value and the value of $S_1 - S_2\cdot(F_1/F_2)$ from our results, we determined $S_2 = 77(33)$ GHz·amu. From this the specific mass shift difference

	Banerjee [66]		Barwood [56]	
	SMS_1	SMS_2	SMS_1	SMS_2
^{85}Rb	2.9(1.4)	−21(9)	2.8(1.4)	−21(9)
^{86}Rb	1.4(7)	−10(5)	1.4(7)	−10(4)
^{81}Rb	9.1(4.5)	−66(29)	8.8(4.5)	−66(28)

Table 6.10: Specific Mass Shift difference (in MHz). SMS_1 is between the $5\mathrm{S}_{1/2}$ and $5\mathrm{P}_{3/2}$ states; SMS_2 is between the $5\mathrm{S}_{1/2}$ and $5\mathrm{D}_{5/2}$ states.

for each isotope investigated in this paper was also found, as shown in Table 6.10.

Banerjee *et al* [66] also measured $\delta\nu_1^{85,87} = -77.992(20)$ MHz. Repeating the above calculations doesn't change the centroid of the specific mass shifts for the D_5 transition, and the change in the errors is also negligible.

Our results show a small difference between the field shift constants of the D_2 transition and the $5\mathrm{S}_{1/2}$ to $5\mathrm{D}_{5/2}$ transition: $F_1/F_2(\text{experiment}) = 0.94(4)$. A theoretical value can be deduced from Dzuba's [63] calculations if we ignore the field shift for the $5\mathrm{D}_{5/2}$ state, $F_1/F_2(\text{theory}) = 1.03(1)$, which agrees with our value within 2σ. Fixing the slope of the King plot to this theoretical value would reduce the error of SMS_2 to 6% and make $S_2 = 85(5)$ GHz·amu.

6.6 Summary

Using the Doppler-free two-photon transition method, we have measured the $5\mathrm{S}_{1/2}$ to $5\mathrm{D}_{5/2}$ transition spectra in three radioactive Rb isotopes ($^{86\mathrm{g}}$Rb, $^{86\mathrm{m}}$Rb and $^{81\mathrm{g}}$Rb). Details of the measurements were explained in this chapter, including the experimental setups, vapor cell references and AOM schemes. By analyzing the measured spectra, we deduced the hyperfine constants for the $5\mathrm{D}_{5/2}$ state and the isotope shifts for the $5\mathrm{S}_{1/2}$ to $5\mathrm{D}_{5/2}$ transition in these radioactive Rb isotopes.

We also investigated the systematic errors involved in the measurements, including the AC Stark shift, the vapor cell reference and the Zeeman effect. The precision we achieved in the ^{86}Rb measurements is about 0.02 MHz for the $5\mathrm{D}_{5/2}$ state hyperfine A constants, and 0.2 MHz for the isotope shifts and the $5\mathrm{D}_{5/2}$ state hyperfine B constants. In the $^{81\mathrm{g}}$Rb measurements, the precision is 10x worse for the $5\mathrm{D}_{5/2}$ state hyperfine constants and 2x worse for the isotope shits, due to the much bigger Zeeman broadening and shifts (caused by the 6x larger trap cloud size).

By making a King plot to separate the field shifts and the mass shifts, we deduced the specific mass shifts between the $5\mathrm{S}_{1/2}$ and $5\mathrm{D}_{5/2}$ states with 40% precision, and obtained a specific mass shift constant of 77(33) GHz·amu. The absolute precision is in a range of 4 – 28 MHz, which is comparable to calculations and measurements in other alkali or alkali-like species [28]. Our results provide a good benchmark for Rb specific mass shift calculations. We also note that the calculations tested by the recent Sr^+ $5S_{1/2}$ and $4D_{5/2}$ specific mass shift measurement [29] could be done in our case as well.

Bibliography

[1] J. Ullrich, et al., *Recoil-ion and electron momentum spectroscopy: reaction-microscopes*, Rep. Prog. Phys., 66, 1463 (2003).

[2] R. Dörner, et al., *Cold Target Recoil Ion Momentum Spectroscopy: a 'momentum microscope' to view atomic collision dynamics*, Physics Reports, 330 (2000), 95 – 192.

[3] L. Resnick, M. K. Sundaresan, and P. J. S. Watson, *Is there a light scalar Boson?*, Phys. Rev. D, Vol. 8, 172 – 78 (1973).

[4] T. W. Donnelly, et al., *Do axions exist?*, Phys. Rev. D, Vol. 18, No. 5, 1607 (1978).

[5] P. T. Matthews, *The parity of Elementary Particles*, IL NUOVO CIMENTO, Vol. VI, N. 3, 2502 (1957).

[6] E. Browne, R. B. Firestone, Table of Radioactive Isotopes, John Wiley & Sons Inc., 1986.

[7] W. D. Schmidt-Ott, Z. Physik, 219, 70 - 74 (1969).

[8] *Invisible axion search ion* ^{139}*La M1 transition*, M. Minowa, et al., Phys. Rev. Lett., 71, 4120 (1993).

[9] P. Jean, C. Wrinkler, et al., Astronomy & Astrophysics, 407, L55 - L58 (2003).

[10] *An asymmetric distribution of positrons in the Galactic disk revealed by Gamma-rays*, Georg Weidenspointner, Nature, Vol. 451, 159 (2008).

[11] *Stringent constraint on Galactic positron production*, J. F. Beacom and H. Yuksel, Phys. Rev. Lett., 97, 071102 (2006).

[12] Pierre Fayet, Phys. Rev. D, Vol. 74, 054034 (2006).

[13] Roberto D. Peccei, *The strong CP problem and Axions*, Lecture Notes in Physics, Volume 741, 3 – 17 (2008).

[14] R. D. Peccei and H. R. Quinn, Phys. Rev. Lett., 38, 1440 (1977).

[15] R. D. Peccei and H. R. Quinn, Phys. Rev. D, 16, 1791 (1977).

[16] S. Weinberg, Phys. Rev. Lett., 40, 223 (1978).

[17] M. Dine, W. Fischler and M. Srednicki, Phys. Lett. 104B, 199 (1981).

[18] *Origin of the matter-antimatter asymmetry*, Michael Dine and Alexander Kusenko, Rev. Mod. Phys., 76 (2004).

[19] *Low Reheating Temperature and the Visible Sterile Neutrino*, G. Gelmini et al., Phys Rev Lett, **93**, 081302 (2004).

[20] *Axion constraints in nonstandard thermal histories*, Daniel Grin, Tristan L. Smith, and Marc Kamionkowski, Phys. Rev. D, 77, 085020 (2008).

[21] *Scalar dark matter candidates*, C. Boehm, P. Fayet, Nuclear Physics B, 683, 219 – 63 (2004).

[22] *Particle physics from stars*, G. Raffelt, Annual Review of Nuclear and Particle Science, Vol. 49, 163 – 216 (1999).

[23] *Isotope Shifts In Atomic Spectra*, W. H. King, 1984.

[24] J. K. Webb, V. V. Flambaum, C. W. Churchill, M. J. Drinkwater, J. D. Barrow, Phys. Rev. Lett., 82, 884 (1999).

[25] W. Nörtershäuser, R. Sánchez, et al., Phys. Rev. A, 83, 012516 (2011)

[26] R. Sánchez, et al., Phys. Rev. Lett., 96, 033002 (2006).

[27] J. A. Behr and G. Gwinner, J. Phys. G, 36, 033101 (2009).

[28] J. C. Berengut, V. A. Dzuba, and V. V. Flambaum, Phys. Rev. A, 68, 022502 (2003).

[29] W. E. Lybarger Jr., J. C. Berengut, and J. Chiaverini, Phys. Rev. A, 83, 052509 (2011).

[30] C. Thibault, et al., Phys Rev. C, Vol. 23, No. 6, 2720 (1981).

[31] E. Mané, et al., Phys. Rev. Lett., 107, 212502 (2011).

[32] Christopher J. Foot, *Atomic Physics*, OXFORD University Press, 2005.

[33] Robert W. Boyd, *Nonlinear Optics*, 2nd edition, chapter 12, page 528 (2003).

[34] C. J. Bordé, J. L. Hall, C. V. Kunasz, and D. G. Hummer, Phys. Rev. A, Vol. 14, No. 1, 236 (1976).

[35] D. M. Brink and G.R. Satchler, *Angular Momentum*, Oxford (1962).

[36] G. Grynberg and B. Cagnac, Rep. Prog. Phys., **40**, 791-841 (1977).

[37] B. E. A. Saleh, M. C. Teich, *Fundamentals of Photonics*, 1991.

[38] T. Swanson, et al., J. Opt. Soc. Am. B, Vol. 15, No. 11, 2641 (1998).

[39] M. Dombsky, P. Bricault and V. Hanemaayer, Nuclear Physics A, 746 (2004), 32c – 39c.

[40] D. Melconian, M. Trinczek, et al., Nuclear Instruments and Methods in Physics Research A, 538 (2005), 93 – 99.

[41] J. Fung, work report for TRINAT group, 2007.

[42] J. Oberheide, P. wilhelms and M. Zimmer, Meas. Sci. Technol. 8 (1997), 351 – 354.

[43] E. Liénard, et al., Nuclear Instruments & Methods in Phys. Research A, 551, 375 – 386 (2005).

[44] D. Steck, *Rubidium 87 D Line Data.*

[45] M. S. Safronova, Carl J. Williams, and Charles W. Clark, Phys. Rev. A, 69, 022509 (2004).

[46] Abraham J. Olson, Evan J. Carlson,and Shannon K. Mayer, Am. J. Phys., Vol. 74, No. 3, 218 (2006).

[47] B. C. Duncan, V. Sanchez-Villicana, P. L. Gould, Phys. Rev. A, 63, 043411 (2001).

[48] Robert J. Cotter, *Time of Flight Mass Spectroscopy, instrumentation and applications in biological research*, chapter 2 (1997).

[49] A. C. Hayes, J. L. Friar and D. Strottman, Phys. Rev. C, Vol. 41, 1727 (2011).

[50] C. H. johnson, F. Pleasonton, and T. A. Carlson, Phys Review, Vol. 132, No. 3, 1963.

[51] N.D. Scielzo, S.J. Freedman, B.K. Fujikawa and P.A. Vetter, Phys. Rev. A, 68, 022716 (2003).

[52] *Atomic Structure Theory*, Walter Johnson, Springer 2007, 169 – 174.

[53] J.R.A. Pitcairn, et al., Phys. Rev. C, 79, 015501 (2009).

[54] E. Prime, M.Sc. thesis, *Loading of a Far Off resonance Dipole Force Trap For Stable* ^{39}K, 2005.

[55] T. Kong, et al., J. Phys. B: At. Mol. Opt. Phys., 44 (2011) 215004.

[56] G. P. Barwood, P. Gill, and W. R. C. Rowley, Appl. Phys. B, Vol. 53, 142 - 147 (1991).

[57] F. Nez, F. Biraben, R. Felder and Y. Millerioux, Optics Communication, Vol. 102, 432 (1993).

[58] Harald Friedrich, *Theoretical Atomic Physics*, Springer press, chapter 3, page 181, 1990.

[59] A. Pérez Galván, et al., Physics Letters B, 655 (2007), 114 - 118.

[60] Vladislav Gerginov, Andrei Derevianko, and Carol E. Tanner, Phys. Rev. Lett., Vol. 91, No. 7, 072501 (2003).

[61] *Investigation of Short-lived Isotopes By Laser Spectroscopy in Treatise on Heavy-Ion Science*, Vol. 8 ed., D.A. Bromley, Ernst W. Otten, Plenum Press, NY 1989.

[62] M. Krystek, M. Anton, Meas. Sci. Tech., Vol. 18, 3438 - 3442 (2007).

[63] V. A. Dzuba, W. R. Johnson and M. S. Safronova, Phys. Rev. A, 72, 022503 (2005).

[64] G. Fricke, C. Bernhardt, et al., Atomic Data and Nuclear Data Tables, 60, 177 - 285 (1995).

[65] I. Angeli, Atomic Data and Nuclear Data Tables, 87, 185 - 206 (2004).

[66] A. Banerjee, D. Das, and V. Natarajan, Opt. Lett., Vol. 28, No. 17, 1579 (2003).

Appendix A

Spectrometer Drawings

Figure A.1: Photo of the spectrometer

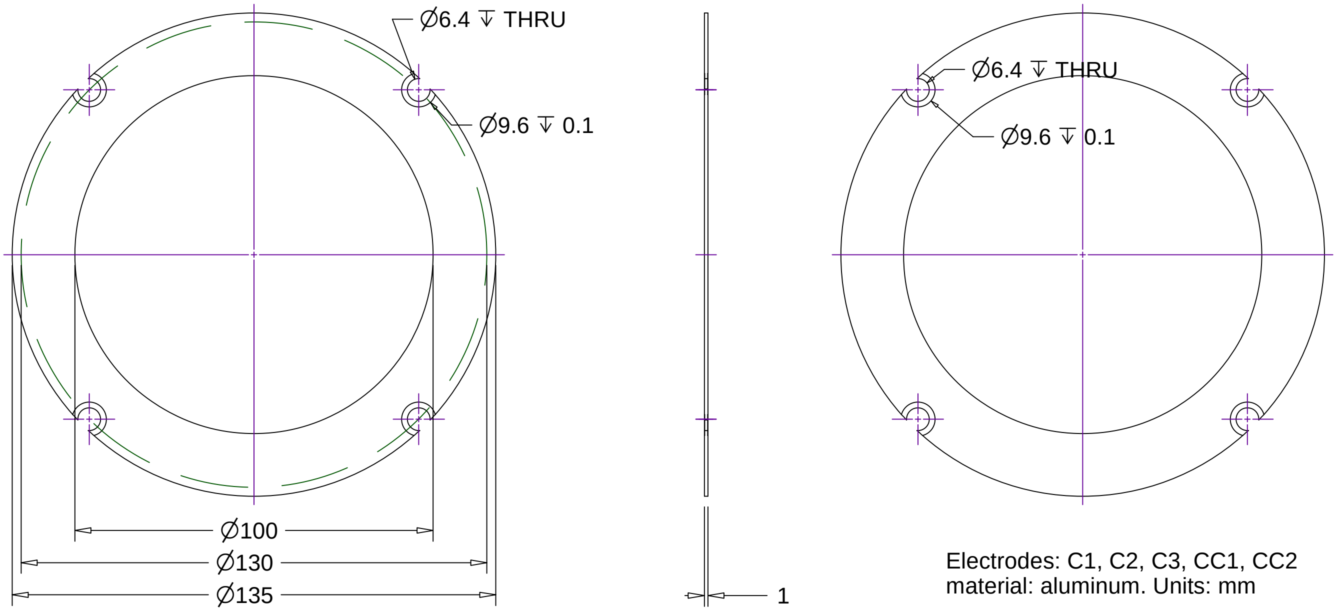

Figure A.2: Drawings of electrode C1, C2, C3, CC1 and CC2.

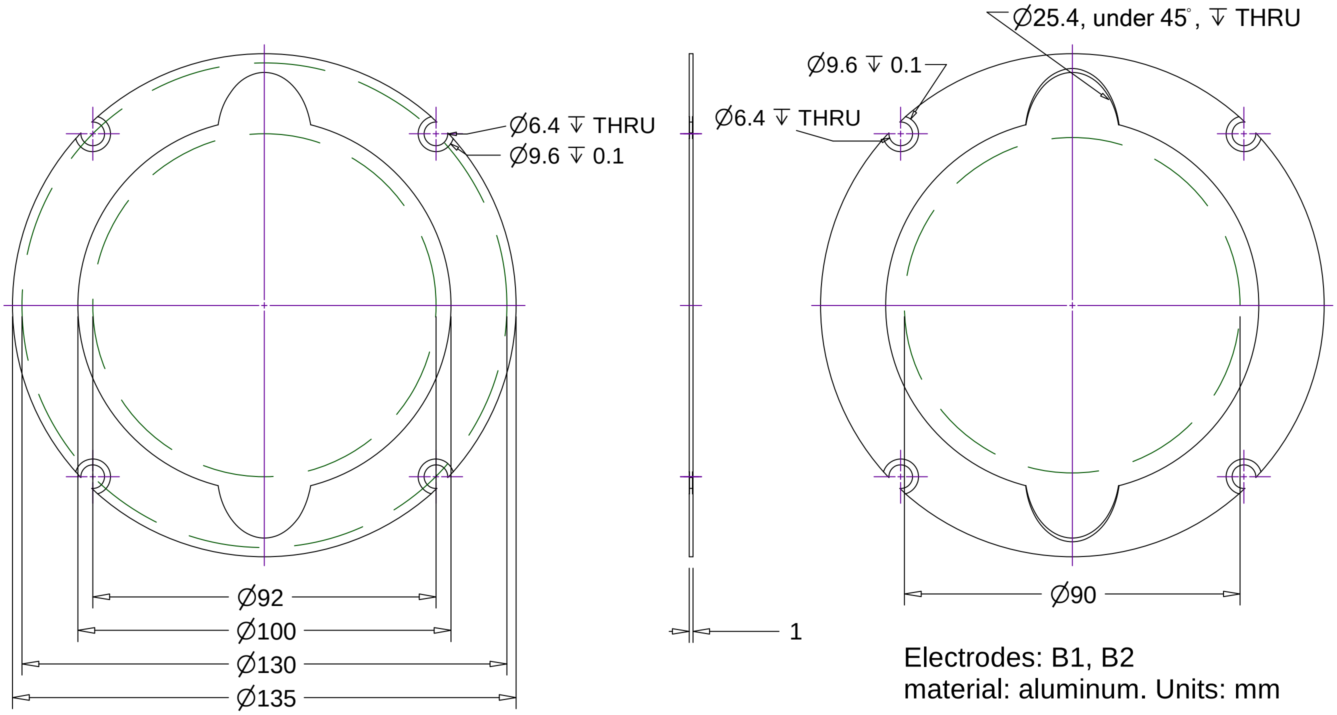

Figure A.3: Drawings of electrode B1 and B2.

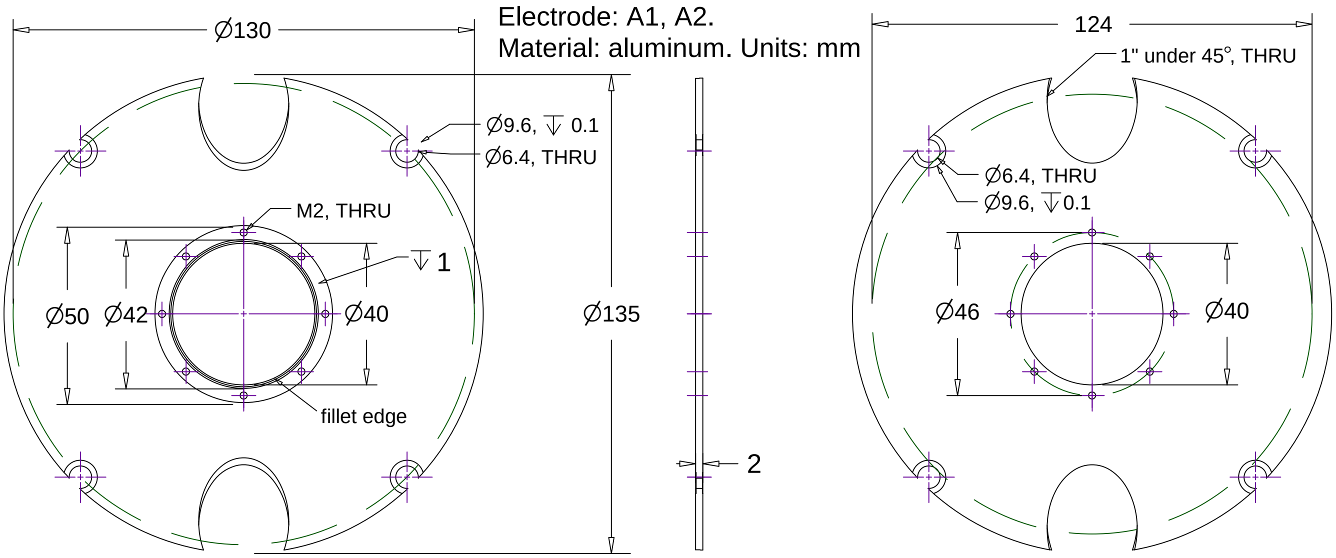

Figure A.4: Drawings for electrode A1 and A2. The electron detector mesh mouting A1 is little different

Appendix B

SimIon Code

B.1 "GEM" Code of The Chamber and Spectrometer

USAGE:

(1) Save the code as "gem" file, and use this geometry file in SimIon to build the vacuum chamber and the spectrometer electrodes. Save the "noname01.pa" file as "filename.pa#", then "refine" the "pa#" file and specify voltage for each electrodes in "fast adjustment".

(2) Two different resolutions could be chosen: 1.0 mm/grid or 0.5 mm/grid.

(3) Use the workbench file "filename.iob" for time-of-flight simulation.

(4) "locate(x,y,z,scale,az,el,rt) {}" defines the new geometry origin (x,y,z) and provides the coordinate transformation by az, el and rt angles. Detailed explanations can be found in the SimIon manual.

(5) "cylinder(xc,yc,zc,rx,ry,length)" defines 3D circular or elliptical cylinder. Parameters define the center at one end, radii, and length. The length always extends in the $-z$ axis direction.

```
;;;The PA# symmetry is planar, y mirror.
;; Resolution of 0.5 mm/grid, scaling factor = 2 and ‘‘x,y,z = 610*260*800 grids’’.
;pa_define(610,260,800,planar,y,E,1)
;locate(360,0,200,2) {

;; Resolution of 1.0 mm/grid: scaling factor = 1 and ‘‘x,y,z = 305x130x400 grids’’.
pa_define(306,130,401,planar,y,E,1)
locate(180,0,100,1) {
;+++++++++++++++++++++++++++++++++++++++++++++++++++++++++++++++++++++++++++++++++
; Firstly build the vacuum chamber, including 6", 4", 3", 3/2", 3/4"
; solid cylinders, the holes will be drilled later. Don’t make the pipes
; one by one, since the crossing region will be overlapped between pipes.
; The holes must be drilled after all solid cylinders are created.
;+++++++++++++++++++++++++++++++++++++++++++++++++++++++++++++++++++++++++++++++++
```

```
; 6" pipe, OD radius = 152.4mm/2 = 76.2mm
e(1) { fill { within { cylinder(0,0,1e6,76.2,, 2e6) } } }
;---------------------------------------------------------------------------------
; 3" pipe, OD radius = 38.1mm
e(1) { fill { within { locate(,,,,,,90) { cylinder(0,0,1e6,38.1,, 2e6) } } } }
;---------------------------------------------------------------------------------
; 4" pipe, OD radius = 50.8mm
e(1) { fill { within { locate(,,,,90,,) {cylinder(0,0,0,50.8,, 2e6)} } } }
;---------------------------------------------------------------------------------
; 3/4" pipe, OD radius = 9.525mm
e(1) { fill { within { locate(,,,,-90,,) {cylinder(0,0,0,9.525,, 2e6)} } } }
;---------------------------------------------------------------------------------
; 30 degree vacuum ports
e(1) { fill { within { locate(,,,,90,,30) { cylinder(0,0,1e6,19.05,, 2e6) } } } }
non_electrode(0){fill{within{locate(,,,,90,,30){cylinder(0,0,1e6, 17.475,,2e6)}}}}
;---------------------------------------------------------------------------------
; 30 degree vacuum ports
e(1) { fill { within { locate(,,,,90,,-30) { cylinder(0,0,1e6,19.05,, 2e6) } } } }
non_electrode(0){fill{within{locate(,,,,90,,-30){cylinder(0,0,1e6, 17.475,,2e6)}}}}
;---------------------------------------------------------------------------------
; 45 degree vacuum ports
e(1) { fill { within { locate(,,,,45,,) { cylinder(0,0,1e6,19.05,, 2e6) } } } }
non_electrode(0){fill{within{locate(,,,,45,,){cylinder(0,0,1e6,17.475,,2e6)}}}}
;---------------------------------------------------------------------------------
; 45 degree vacuum ports
e(1) { fill { within { locate(,,,,-45,,) { cylinder(0,0,1e6,19.05,, 2e6) } } } }
non_electrode(0){fill{within{locate(,,,,-45,,){cylinder(0,0,1e6,17.475,,2e6)}}}}
;---------------------------------------------------------------------------------
; Now drill holes inside the solid cylinders to finish the vacuum pipes.
;---------------------------------------------------------------------------------
; 6" pipe, 0.084"w, ID radius = 74.0664mm
non_electrode(0) { fill {within { cylinder(0,0,1e6,74.0664,, 2e6) } } }
;---------------------------------------------------------------------------------
; 3" pipe, 0.065"w, ID radius = 36.45mm
non_electrode(0){fill{within{locate(,,,,,,90){cylinder(0,0,1e6,36.45,,2e6)}}}}
;---------------------------------------------------------------------------------
; 4" pipe, 0.065"w, ID radius = 49.15mm
non_electrode(0){fill{within{locate(,,,,90,,){cylinder(0,0,0,49.15,,2e6)}}}}
;---------------------------------------------------------------------------------
; 3/4" pipe, 0.062"w, ID radius = 7.95mm
non_electrode(0){fill{within{locate(,,,,-90,,){cylinder(0,0,0,7.95,,2e6)}}}}
;+++++++++++++++++++++++++++++++++++++++++++++++++++++++++++++++++++++++++++++++++
; Now build the spectrometer, which has 9 electrodes in total, plus 4 rods.
; electrodes 2-8 are 135mm OD, 100mm ID, and 1mm thick.
```

```
; electrodes 1 and 9 are 146 mm OD, same ID, and 2mm thick.
;++++++++++++++++++++++++++++++++++++++++++++++++++++++++++++++++++++++++++++++++
e(1) { fill { within {  cylinder(0,0,61.59,73.0,,2) }
              notin  {  cylinder(0,0,61.59,20.0,,2) } } }
;40 mm diameter mesh, 1mm thickness.
e(1) { fill { within {  cylinder(0,0,61.59,20.0,,0) } } }
;--------------------------------------------------------------------------------
e(2) { fill { within {  cylinder(0,0,45.42,67.5,,1) }
              notin  {  cylinder(0,0,45.42,50.0,,1) } } }
;--------------------------------------------------------------------------------
e(3) { fill { within {  cylinder(0,0,32.11,67.5,,1) }
              notin  {  cylinder(0,0,32.11,50.0,,1) } } }
;--------------------------------------------------------------------------------
e(4) { fill { within {  cylinder(0,0,30.11,67.5,,1) }
              notin  {  cylinder(0,0,30.11,50.0,,1) } } }
;--------------------------------------------------------------------------------
e(5) { fill { within {  cylinder(0,0,12.96,67.5,,1) }
              notin  {  cylinder(0,0,12.96,50.0,,1) } } }
;--------------------------------------------------------------------------------
e(6) { fill { within {  cylinder(0,0,-11.96,67.5,,1) }
              notin  {  cylinder(0,0,-11.96,50.0,,1) } } }
;--------------------------------------------------------------------------------
e(7) { fill { within {  cylinder(0,0,-30.12,67.5,,1) }
              notin  {  cylinder(0,0,-30.12,50.0,,1) } } }
;--------------------------------------------------------------------------------
e(8) { fill { within {  cylinder(0,0,-45.29,67.5,,1) }
              notin  {  cylinder(0,0,-45.29,50.0,,1) } } }
;--------------------------------------------------------------------------------
e(9) { fill { within {  cylinder(0,0,-60.46,67.5,,2) }
              notin  {  cylinder(0,0,-60.46,20.0,,2) } } }
;40 mm diameter mesh, 1mm thickness.
e(9) { fill { within {  cylinder(0,0,-60.46,20.0,,0) } } }
;--------------------------------------------------------------------------------
; electrodes with 80 mm ID diameter, OD is the same as the spectrometer end-plate,
; 2mm thickness, V = 0, located in front of the ion MCP,
e(1) { fill { within {  cylinder(0,0,277.42,73.0,,2) }
              notin  {  cylinder(0,0,277.42,40.0,,2) } } }
; 80 mm diameter mesh, 1mm thickness, and V = 0.
e(1) { fill { within {  cylinder(0,0,275.42,40.0,,0) } } }
;++++++++++++++++++++++++++++++++++++++++++++++++++++++++++++++++++++++++++++++++
;1" diameter trapping laser beam, cut off part of the electrodes.
;++++++++++++++++++++++++++++++++++++++++++++++++++++++++++++++++++++++++++++++++
non_electrode(0){fill{within{locate(,,,, 45,,){cylinder(0,0,1e6, 12.7,,2e6)}}}}
non_electrode(0){fill{within{locate(,,,,-45,,){cylinder(0,0,1e6, 12.7,,2e6)}}}}
```

```
;++++++++++++++++++++++++++++++++++++++++++++++++++++++++++++++++++++++++++++++++
; Building 4 rods. Only 2 rods need to be built,
; the other 2 will be created by the planar symmetry of Y axis.
;-------------hole is bigger than the metal rod, be built firstly---------------
non_electrode(0) { fill { within { cylinder( 46,46,63,3.2,,126) } } }
non_electrode(0) { fill { within { cylinder(-46,46,63,3.2,,126) } } }
;-------------central 2mm stainless steel rods---------------------------------
e(1) { fill { within { cylinder( 46,46,63,1,,126) } } }
e(1) { fill { within { cylinder(-46,46,63,1,,126) } } }
;--End beeds, made of stainless steel and separated by ceramic washers----------
e(1) { fill { within { cylinder( 46,46, 73,5.08,,10) } } }
e(1) { fill { within { cylinder(-46,46, 73,5.08,,10) } } }
e(1) { fill { within { cylinder( 46,46,-63,5.08,,10) } } }
e(1) { fill { within { cylinder(-46,46,-63,5.08,,10) } } }
;-------------------------------------------------------------------------------
e(1) { fill { within { cylinder( 46,46,59,5.08,,13) } } }
e(1) { fill { within { cylinder(-46,46,59,5.08,,13) } } }
;-------------------------------------------------------------------------------
e(1) { fill { within { cylinder( 46,46,43,5.08,,10.31) } } }
e(1) { fill { within { cylinder(-46,46,43,5.08,,10.31) } } }
;-------------------------------------------------------------------------------
e(1) { fill { within { cylinder( 46,46,28,5.08,,14) } } }
e(1) { fill { within { cylinder(-46,46,28,5.08,,14) } } }
;-------------------------------------------------------------------------------
e(1) { fill { within { cylinder( 46,46,11,5.08,,22) } } }
e(1) { fill { within { cylinder(-46,46,11,5.08,,22) } } }
;-------------------------------------------------------------------------------
e(1) { fill { within { cylinder( 46,46,-14,5.08,,15) } } }
e(1) { fill { within { cylinder(-46,46,-14,5.08,,15) } } }
;-------------------------------------------------------------------------------
e(1) { fill { within { cylinder( 46,46,-32,5.08,,12) } } }
e(1) { fill { within { cylinder(-46,46,-32,5.08,,12) } } }
;-------------------------------------------------------------------------------
e(1) { fill { within { cylinder( 46,46,-47,5.08,,12) } } }
e(1) { fill { within { cylinder(-46,46,-47,5.08,,12) } } }
;-------------------------------------------------------------------------------
} ;close-bracket for locate()
```

B.2 "LUA" Code of The Quadrupole Magnetic Field

USAGE:

(1) SIMION workbench program that incorporates solenoid magnetic field from Biot-Savart cal-

culation into workbench.
(2) Save the file as “*.lua”, same name as the workbench file.
(3) The workbench must contain an empty magnetic PA (with the same geometry as the electric PA) in which to apply this magnetic field.
(4) This code was written for SimIon 8.04.

```
simion.workbench_program()
; Load Biot-Savart magnetic field calculation support.
local MField = require "simionx.MField"

; Defined quadrupole magnetic field, composed of two solenoids in
; quadrupole configuration, center is at (62.5,0,0)mm.
; coil geometry: OD 191 mm,ID 131 mm, thickness: 33 mm, Gap: 6"(152.4mm)

adjustable ccurrent = 50.5
local ccurrent_last
local field

function segment.mfield_adjust()
  if ccurrent ~= ccurrent_last then
     ccurrent_last = ccurrent

     field = MField.combined_field {
        MField.solenoid_hoops {
            current = -1*ccurrent,
            first   = MField.vector(180,109.2,100),
            last    = MField.vector(180,76.2,100),
            radius  = 80.5,
            nturns  = 32
            },
        MField.solenoid_hoops {
            current = ccurrent,
            first   = MField.vector(180,-109.2,100),
            last    = MField.vector(180,-76.2,100),
            radius  = 80.5,
            nturns  = 32
            }
     }
end

ion_bfieldx_gu, ion_bfieldy_gu, ion_bfieldz_gu =
field(ion_px_mm, ion_py_mm, ion_pz_mm)

end
```